Wrocław University of Technology
Centre of Advanced Materials and Nanotechnology

Materials Science
Poland

Vol.22 • No. 2 • 2004

Oficyna Wydawnicza Politechniki Wrocławskiej

Materials Science is an interdisciplinary journal devoted to experimental and theoretical research into the synthesis, structure, properties and applications of materials.

Among the materials of interest are:

- glasses and ceramics
- sol-gel materials
- photoactive materials (including materials for nonlinear optics)
- laser materials
- photonic crystals
- semiconductor micro- and nanostructures
- piezo-, pyro- and ferroelectric materials
- high-T_c, superconductors
- magnetic materials
- molecular materials (including polymers) for use in electronics and photonics
- novel solid phases
- other novel and unconventional materials

The broad spectrum of the areas of interest reflects the interdisciplinary nature of materials research. Papers covering the modelling of materials, their synthesis and characterisation, physicochemical aspects of their fabrication, properties and applications are welcome. In addition to regular papers, the journal features issues containing conference papers, as well as special issues on key topics in materials science.

Materials Science is published under the auspices of the Centre of Advanced Materials and Nanotechnology of the Wrocław University of Technology, in collaboration with the Institute of Low Temperatures and Structural Research of the Polish Academy of Sciences and the Wroclaw University of Economics.

All accepted papers are placed on the Web page of the journal and are available at the address:
http://MaterialsScience.pwr.wroc.pl

The Journal is supported by the State Committee for Scientific Research

Editorial Office
Karol Langner
Łukasz Maciejewski

Printed in Poland

Drukarnia Oficyny Wydawniczej Politechniki Wrocławskiej
Zam. nr 514/2004.

Contents

Materials Science-Poland, Vol. 22, No. 2, 2004

Chemical durability of β-wollastonite-reinforced glass-ceramics prepared from waste fluorescent glass and calcium carbonate

BYUNG-HOON KIM[1], BO-AN KANG[2], YEON-HUM YUN[2], KYU-SEOG HWANG[2*]

[1]Department of Materials Science and Engineering, Chonnam National University, 300 Yongbong-dong, Buk-gu, Gwangju 500-757, South Korea

[2]Department of Applied Optics and Institute of Photoelectronic Technology, Nambu University, 864-1 Wolgye-dong, Gwangsan-gu, Gwangju 506-824, South Korea

We prepared glass-ceramics reinforced by β-wollastonite using waste fluorescent glass to resolve the environmental problem. Fluorescent glass and calcium carbonate were used as starting materials. The chemical durability of specimens heat-treated at 800 °C, 900 °C, and 1000 °C was analyzed by both measuring weight change and observing surface morphology. Specimen composition was determined with energy dispersive X-ray spectroscopy. As the heat treatment temperature was increased from 800 °C to 1000 °C, the chemical durability decreased, especially in the glass-matrix area. A compressive strength of about 250–350 MPa was sufficiently large for practical use.

Key words: *glass-ceramics; β-wollastonite; fluorescent glass*

1. Introduction

Wollastonite ($CaSiO_3$) is an important substance in the ceramic and cement industries. A host of favourable properties such as low shrinkage, good strength, lack of volatile constituents, body permeability, fluxing characteristics, whiteness and acicular shape renders wollastonite useful in several ceramic and other applications. The growing demand for wollastonite in recent years has been attested by a steady increase in production worldwide [1].

Conversion or inclusion in glass-ceramic systems has been used to extend recycling to several types of by-products, such as fly ash from coal- and oil-fired electric power stations and fly ash from urban solid waste incinerators [2]. Some of these

*Corresponding author, e-mail: khwang@mail.nambu.ac.kr.

glass-ceramic materials have become commercial products [3] or have been developed up to the pre-industrial stage [4]. Their main applications are in the field of abrasion-resistant materials, i.e., industrial floor coverings, wall facings, abrasion-resistant linings, and high-temperature insulators. Moreover, low cost and availability of the raw materials make them very attractive from the economic point of view. However, according to our knowledge no useful and economic method of their preparation has been devised as yet [5].

Recently, we have prepared glass-ceramics from waste fluorescent glass [6]. In this work, we investigate the chemical durability of glass-ceramics reinforced by β-wollastonite. The mechanical strength of these glass-ceramics has been determined.

2. Experimental procedure

Preparation of the specimens used in this study was similar to that described in our previous report [6]. Briefly, fluorescent glass and calcium carbonate ($CaCO_3$, Duksan Co., Ltd., South Korea) were used to prepare β-wollastonite glass-ceramics. Table 1 shows the chemical composition of the fluorescent glass used. Waste fluorescent glass cullet was washed with water to remove attached Hg, and dried at 110 °C for 24 h in air. The compositions of the mother glasses of the glass-ceramics were fixed at glass cullet: $CaCO_3$ = 4:1 in weight ratio. About 30 g of powder mixture was put in an alumina crucible and melted in a box-type SiC electric furnace at 1300 °C for 1 h in air. In order to quench the glass, the melts were rapidly poured into a water bath at room temperature and dried at 110 °C for 24 h in air. The quenched glass was ground in an agate mill and pressed into a disk 0.5 cm thick and 3 cm in diameter. The green disks were heated in a tube-type furnace to 800 °C, 900 °C, and 1000 °C at a rate of 5 °C /min for 1 h, respectively, and then allowed to cool inside the furnace.

Table 1. The chemical composition of the fluorescent glass

Element	Content wt. %
O	29.55
Na	11.01
Mg	1.79
Al	2.02
Si	47.04
K	2.02
Ca	6.57
Total	100.00

To analyze their chemical durability, the specimens were immersed into 20 cm^3 of acidic solution (0.5 M H_2SO_4) at 80 °C for 48 h. After this treatment, the specimens were successively washed with distilled water and dried at 80 °C for 24 h in air. The

chemical durability of the specimens was analyzed by both measuring weight change and observing surface morphology with field emission-scanning electron microscopy (FE-SEM, S-4700, Hitachi Co., Jpn.). Variations in chemical compositions at the surface of the specimens before and after immersing were evaluated by an energy dispersive X-ray spectrometer (EDX) equipped with a Robinson-type backscattered electron detector. Compressive strength was determined using a universal tester with a 0.5 mm/min crosshead speed (Instron 4302, Instron Co., England).

3. Results and discussion

Figure 1 shows the FE-SEM images of fractured cross sections of the sintered samples. Morphological analysis of the specimens at 900 °C and 1000 °C shows a dense structure. However, the structure of the sample sintered at 800 °C was porous with large particles throughout the sample. We assume that porous structure was caused by the vaporization of organics during heat treatment or by insufficient annealing.

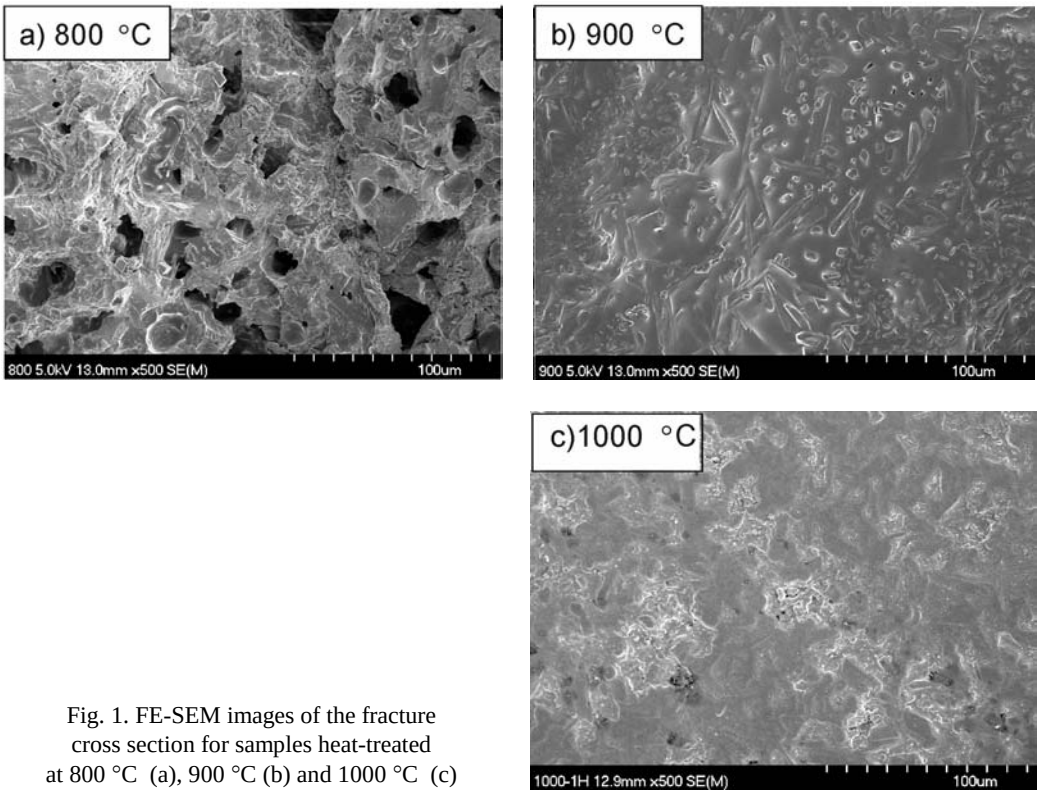

Fig. 1. FE-SEM images of the fracture cross section for samples heat-treated at 800 °C (a), 900 °C (b) and 1000 °C (c)

Table 2 shows the chemical durability of the specimens heat-treated at 800 °C, 900 °C, and 1000 °C . The chemical durability of these samples was not significantly affected by heat-treatment temperatures, although the weight loss of the sample heat-

treated at 1000 °C exhibited a small but significant increase. Since it is difficult to analyze the exact chemical durability of the samples due to their small weight changes before and after immersing, we were not able to explain the variations in the chemical durability by measuring weight gain alone.

Table 2. Weight changes of the glass-ceramics heat-treated at 800 °C (A), 900 °C (B) and 1000 °C (C) between before acid-immersion (BA) and after acid-immersion (AA)

Sample	BA (g)	AA (g)	Weight-loss (%)
A	36.985	36.947	0.1030
B	36.685	36.619	0.1060
C	36.376	36.335	0.1130

In order to obtain more insight into chemical durability, morphology and chemical composition at the surface of the samples were evaluated by FE-SEM and EDX before and after immersing the samples in acidic sol. Figures 2, 4, and 6 show the surface morphologies and chemical compositions of the glass-ceramics heat-treated at 800 °C, 900 °C and 1000 °C before acid-treatment. Si, Ca, Al, and alkali ions such as Na, Mg, and K were detected on the surfaces of all samples before acid-immersion. However, as is clearly seen in Fig. 6c, relatively small and strong peak intensities corresponding to Na and Ca, respectively, were identified on the surface grain for the sample heat-treated at 1000 °C .This is probably due to the formation of highly crystalline β-wollastonite. Simultaneously, as shown in Figs. 2 and 4, for samples heat-treated at 800 °C and 900 °C it is very difficult to detect variations in peak intensities between the glass-matrix (Figs. 2a and 4a) and grain-like area (Figs. 2b and 4b). It is clearly shown in Fig. 6 that as the heat-treatment temperature increased to 1000 °C, the amount of Na in the glass matrix confirmed by EDX was significantly larger than that in the whisker-type grains. Moreover, the calcium content of the glass-matrix at 800 °C and 900 °C significantly decreased with increasing heat treatment temperature. This is additional evidence of the growth of β-wollastonite crystals in the sample heated at 1000 °C, since the formation of β-wollastonite needs more calcium ions.

Figures 3, 5 and 7 show the surface morphologies and chemical compositions of glass-ceramics heat treated at 800 °C, 900 °C, and 1000 °C, respectively, after acid-immersion. Figs. 3 and 5 show that it is very difficult to identify variations in the amount of Na ions in the glass-matrix for samples heat-treated at 800 °C and 900 °C, whereas a significant decrease of Na ion concentration was detected in the grain-like area. On the contrary, at 1000 °C, as shown in Fig. 7, the amount of Na ions in the glass-matrix decreased after acid-immersion (compare Fig. 6b with Fig. 7b).

In order to compare ion contents more clearly, we determined the weight ratio (Na/Si) for different samples, as shown in Fig. 8. For the samples heat-treated at 800 °C and 900 °C, Na ion-diffusion was larger in the grain-like area than in the glass-matrix. The sample heat-treated at 1000 °C gave the opposite result, i.e., the glass-matrix exhibited larger Na-diffusion after acid-immersion.

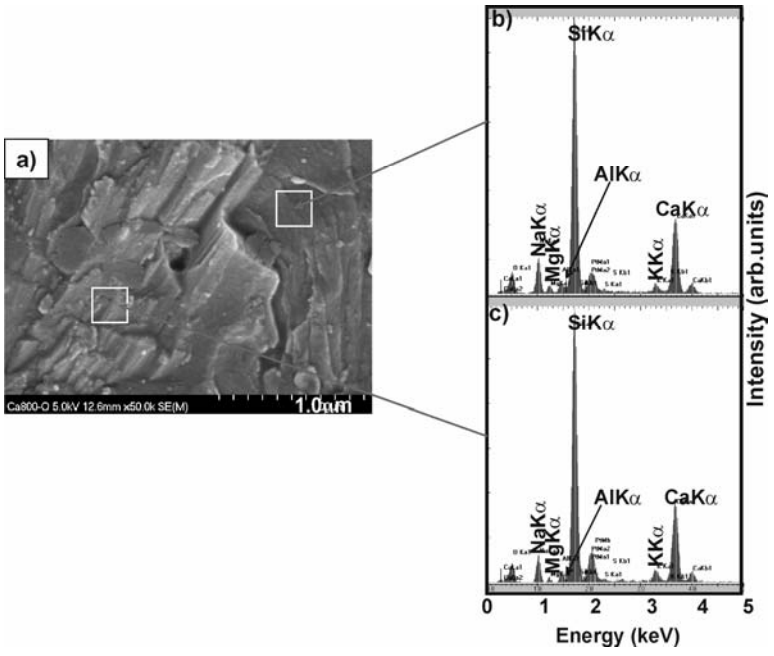

Fig. 2. FE-SEM image (a) and chemical composition of the surface (matrix (b) and grain (c)) of the glass-ceramic heat-treated at 800 °C, before acid-immersion

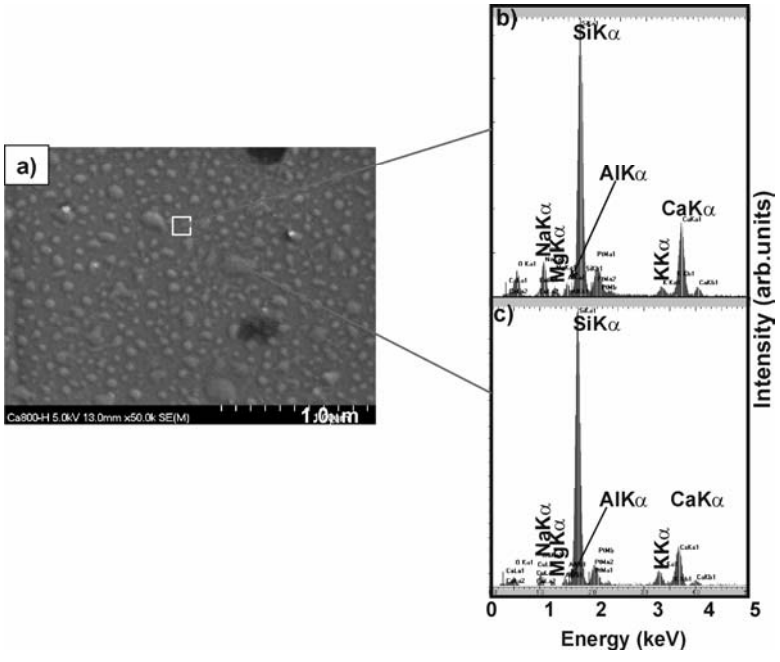

Fig. 3. FE-SEM image (a) and chemical composition of the surface (matrix (b) and grain (c)) of the glass-ceramic heat-treated at 800 °C, after acid-immersion

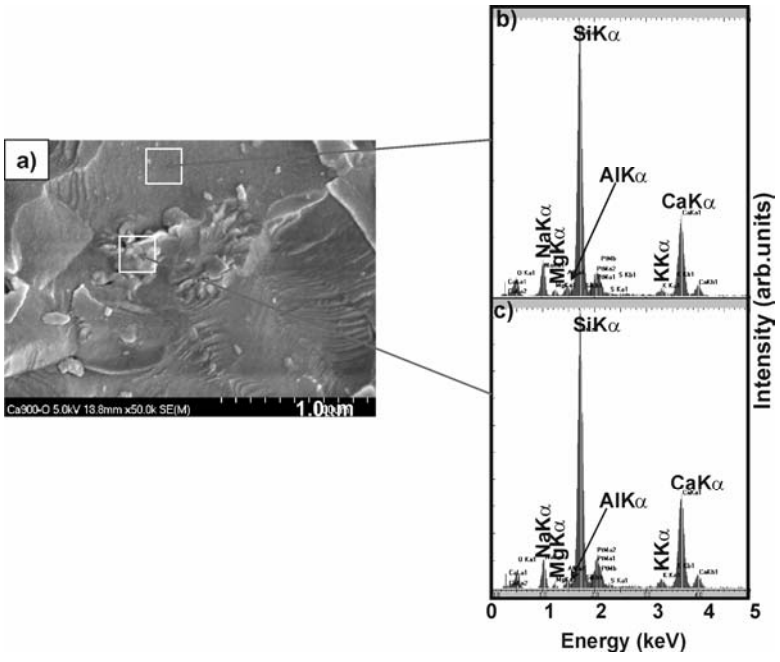

Fig. 4. FE-SEM image (a) and chemical composition of the surface (matrix (b) and grain (c)) of the glass-ceramic heat-treated at 900 °C, before acid-immersion

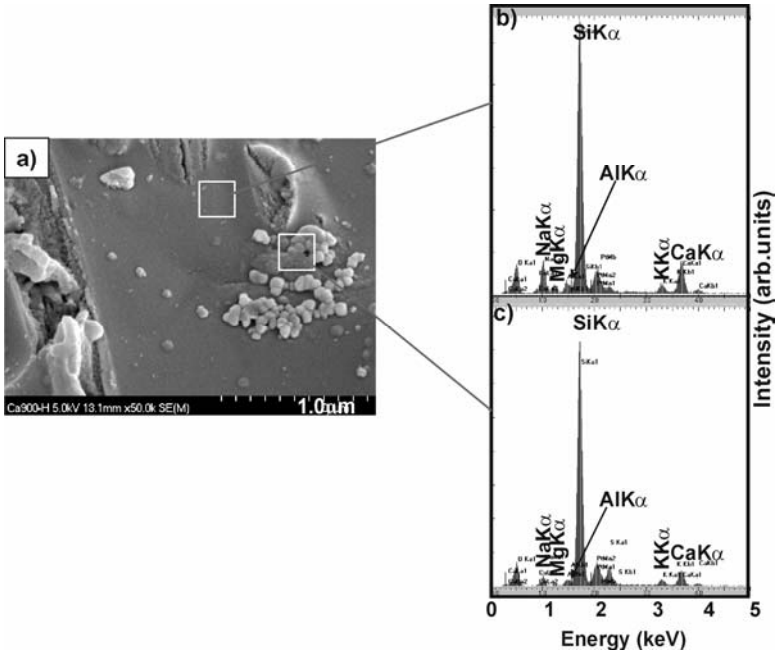

Fig. 5. FE-SEM image (a) and chemical composition of the surface (matrix (b) and grain (c)) of the glass-ceramic heat-treated at 900 °C, after acid-immersion

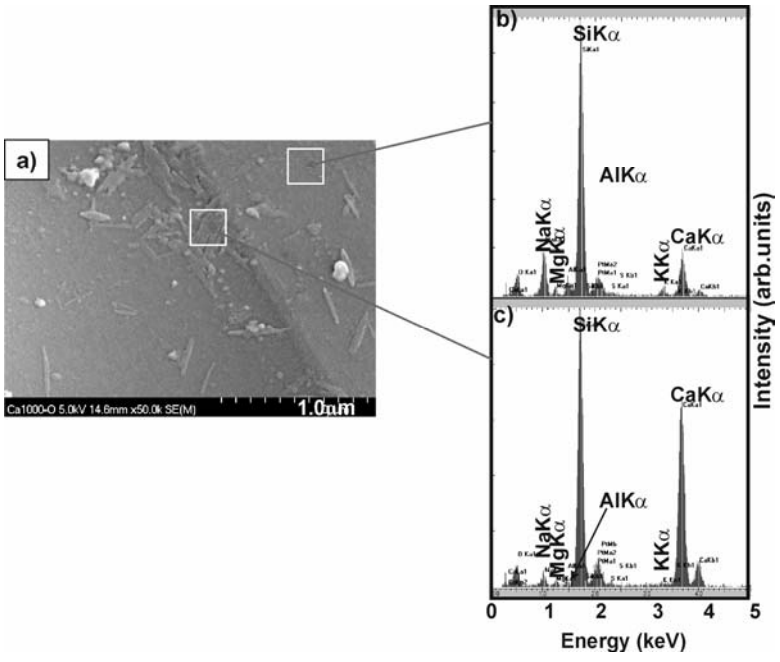

Fig. 6. FE-SEM image (a) and chemical composition of the surface (matrix (b) and grain (c)) of the glass-ceramic heat-treated at 1000 °C, before acid-immersion

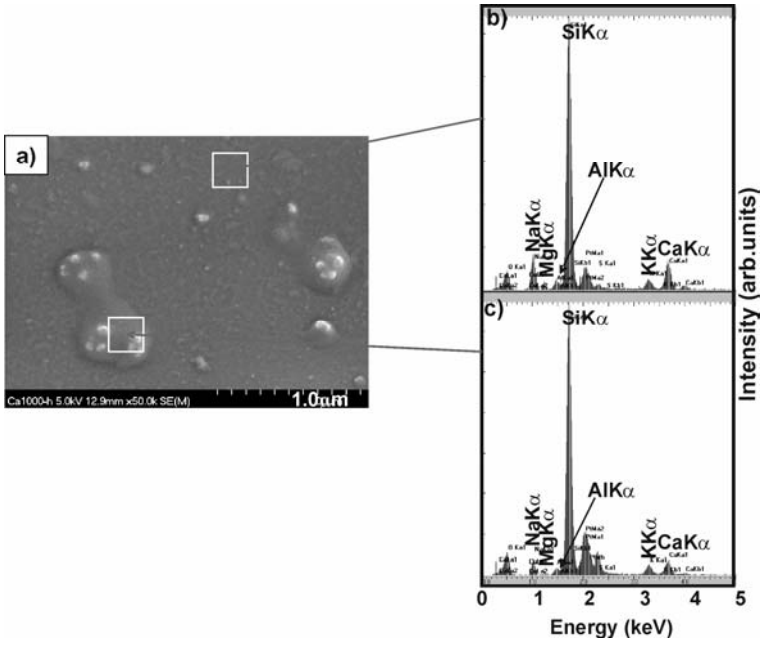

Fig. 7. FE-SEM image (a) and chemical composition of the surface (matrix (b) and grain (c)) of the glass-ceramic heat-treated at 1000 °C, after acid-immersion

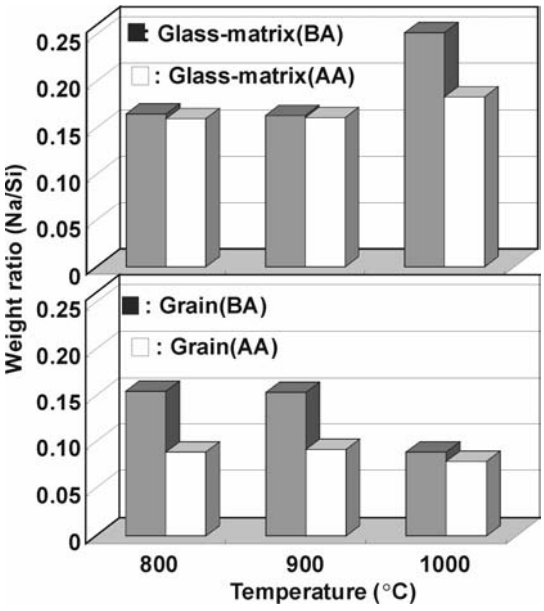

Fig. 8. Variation in the Na contents of the glass-ceramics surface at various temperatures between before (BA) and after acid-immersion(AA)

Generally, the chemical stability of glass-ceramic materials is affected by the composition of the crystalline phase and by the composition and amount of residual glass phase and its morphology. Alkali ions are much more stable in the crystalline phase than in the residual glass phase. Consequently, in order for glass-ceramic materials to have good chemical resistance, it is necessary that their residual glass phase contain low concentrations of alkali metal oxides in particular [7]. From our measurements of weight gain and EDX analysis, we conclude that the chemical durability of samples heat-treated at 800 °C and 900 °C was favourably improved, since their crystalline phase (grains) contained a larger amount of alkali ions (such as Na) as compared with the glass-matrix. On the other hand, it is assumed that chemical durability was decreased at 1000 °C, since the glass matrix contained relatively large amounts of alkali ions owing to diffusion during the high temperature heat treatment.

We also determined the compressive strength of samples heat-treated at 800 °C, 900 °C, and 1000 °C . The compressive strength of the samples decreased with increasing heat-treatment temperature, being 313.87, 230.33, and 226.6 MPa for the 800 °C-, 900 °C- and 1000 °C-heat-treated samples. Generally, glass-ceramics reinforced by whisker-type β-wollastonite crystals show high mechanical strength. However, in our work, the compressive strength was slightly decreased for samples heat-treated at 1000 °C, although well-crystallized β-wollastonite crystals were identified in the glass-matrix, as shown in our previous report [6]. Furthermore, samples treated at 800 °C, having a porous structure, showed a larger compressive strength. By com-

paring with the data for marble (110–170 MPa) [8], we conclude that our samples exhibit a compressive strength large enough for practical usage for all heat-treatment temperatures investigated. The samples treated at 800 °C are glass-ceramics with the potential to use light-weight resources having high strength.

Further experimental studies are needed to investigate chemical durability with other etching agents and in various conditions.

4. Conclusion

We prepared glass-ceramics reinforced with β-wollastonite from waste fluorescent glass and calcium carbonate. From FE-SEM and EDX analyses, we conclude that the glass-ceramics heat-treated at 800 °C and 900 °C showed favourable improvements in chemical durability, since their crystalline phase had a larger amount of alkali ions as compared with the glass-matrix. The compressive strength of the samples obtained at all investigated heat-treatment temperatures (800, 900 and 1000 °C) is large enough for practical usage. Samples treated at 800 °C are glass-ceramics with potentialities to use light-weight resources having high strength.

Acknowledgement

This work was supported by Korea Research Foundation Grant (KRF-2002-042-D00088).

References

[1] CHANG C. K., MAO D. L., WU J. S., Ceram. Int., 26 (2000), 779.
[2] BOCCACCINI A. R., PETITMERMET M., WINTERMANTEL E., Am. Ceram. Soc. Bull., 76 (1997), 75.
[3] DAVIES M.W., KERRISON B., GROSS W.E., ROBSON M.J.D., WICHALL W., J. Iron. Steel Inst., 208 (1970), 348.
[4] ROGERS P., ROBERTSON J., Interceram., 38 (1989), 37.
[5] KUBO K., U.S. Patent 3928054 (1975).
[6] YUN Y.H., YOON C.H., KIM C.K., KIM S.B., KWON J.T., KIM S.B., HWANG K.S., Ceram. Int. 28 (2002), 503.
[7] STRNAD Z., *Glass-ceramic materials*, Vol. 8, Elsevier, New York, 1986, p. 182.
[8] TANAKA M., SUZUKI S., J. Ceram. Soc. Jpn., 107 (1999), 627.

Received 19 December 2003
Revised 9 February 2004

Materials Science-Poland, Vol. 22, No. 2, 2004

The effect of film thickness on physical properties of fluorine-doped indium oxide thin films

S. M. ROZATI*, T. GANJ

Physics Department, University of Guilan, Rasht 41335, Iran

In this paper, fluorine-doped indium oxide films of thicknesses ranging from 115 nm to 1290 nm were prepared using the spray pyrolysis technique by varying the amount of spray solution and keeping constant the substrate temperature, doping concentration and air flow rate. The preferential growth orientation was determined using the X-ray diffraction (XRD) spectra of doped indium oxide films of various thicknesses. The sheet resistance decreases gradually with the film thickness and reaches a stable value. It has also been observed that an increase in thickness deteriorates the optical properties of the deposited films beyond some limit.

Key words: *In_2O_3:F; transparent conductive oxide; spray pyrolysis*

1. Introduction

Optically transparent and electrically conductive films of tin, indium and zinc oxide (doped and undoped) have been studied due to their increasing practical applications [1–7]. Owing to their high optical transmittance and electrical conductivity, the films are useful in photovoltaic and photothermal applications. Transparent conducting oxide (TCO) films, which can be deposited by numerous techniques, exhibit high transmittance in the visible spectral region, high reflectance in the IR region and relatively good metallic conductivity [4–10]. Their electrical as well as optical properties can be studied by controlling the deposition parameters [11].

The transmission of light in the visible region suggests a wide band gap, characteristic of transparent conducting materials. The only way to obtain a combination of good transparency in the visible range and simultaneous high electrical conductivity is to create electron degeneracy with appropriate dopants in the oxide films [1, 9]. In

* Corresponding author, e-mail: smrozati@guilan.ac.ir.

this report, we have characterized the physical properties of In_2O_3:F films, deposited using the spray pyrolysis technique, with respect to variations in film thickness.

2. Experimental

The spray pyrolysis unit consisted of a heater capable of heating the substrate up to 700 °C and a temperature controller unit to control the substrate temperature. The spray technique is one of the most commonly used techniques for preparing transparent and conducting oxides. It owes this to its simplicity, non-vacuum system of deposition and hence inexpensive method for large-area coatings.

In order to prepare the solution for depositing fluorine-doped indium oxide films, the following procedure was adapted. The starting material, indium metal, was dissolved in HCl and the solution heated in order to complete the reaction. After evaporating the excess water, remaining indium chloride ($InCl_3$) was recrystallized twice or thrice in order to obtain pure indium chloride, and finally a solution of ammonium fluoride was added to the $InCl_3$ solution for depositing fluorine-doped indium oxide films. The optical transmission was evaluated using a UV visible spectrophotometer (UV/VIS-2100 Shimadzu). X-ray diffraction (XRD, Philips-pw-1830) was used to characterize the crystal structure of the films. The thicknesses of the films were calculated from the interference pattern observed in the visible region with the formula given by Manifacier [12].

3. Results and discussion

In_2O_3:F films of various thicknesses were prepared by changing the time of deposition, which resulted in a change of the volume of solution sprayed. In_2O_3:F (F/In = 10 wt. %) thin films were deposited onto Corning 7059 glass substrate at film thicknesses ranging from 115 nm to 1290 nm. All other parameters were kept constant, i.e. substrate temperature T_s = 425 °C, flow rate of 6 dm^3 per minute (lpm), the distance between the substrate and nozzle D_{sn} = 30 cm and solution composition. Figure 1 shows the X-ray diffraction patterns of F-doped indium oxide films of various thicknesses T. It can be seen that the preferred orientation [400] becomes more predominant as the thickness increases, however above 920 nm the intensity of the (400) plane is saturated. A similar behaviour has been obtained by Agashe et al. in SnO_2:F films deposited by the spray pyrolysis method [13]. Films thinner than 300 nm exhibited an amorphous structure.

Figure 2 shows the variation of the sheet resistance of these films at room temperature as a function of thickness. The sheet resistance of thinner films is much higher due to a predominant contribution of the amorphous phase and that of thicker films is much lower due to the presence of crystalline phases. A similar behaviour of the dependence of sheet resistivity on thickness has been obtained by Chaudhuri et al. [14] and Martinez et al. [15].

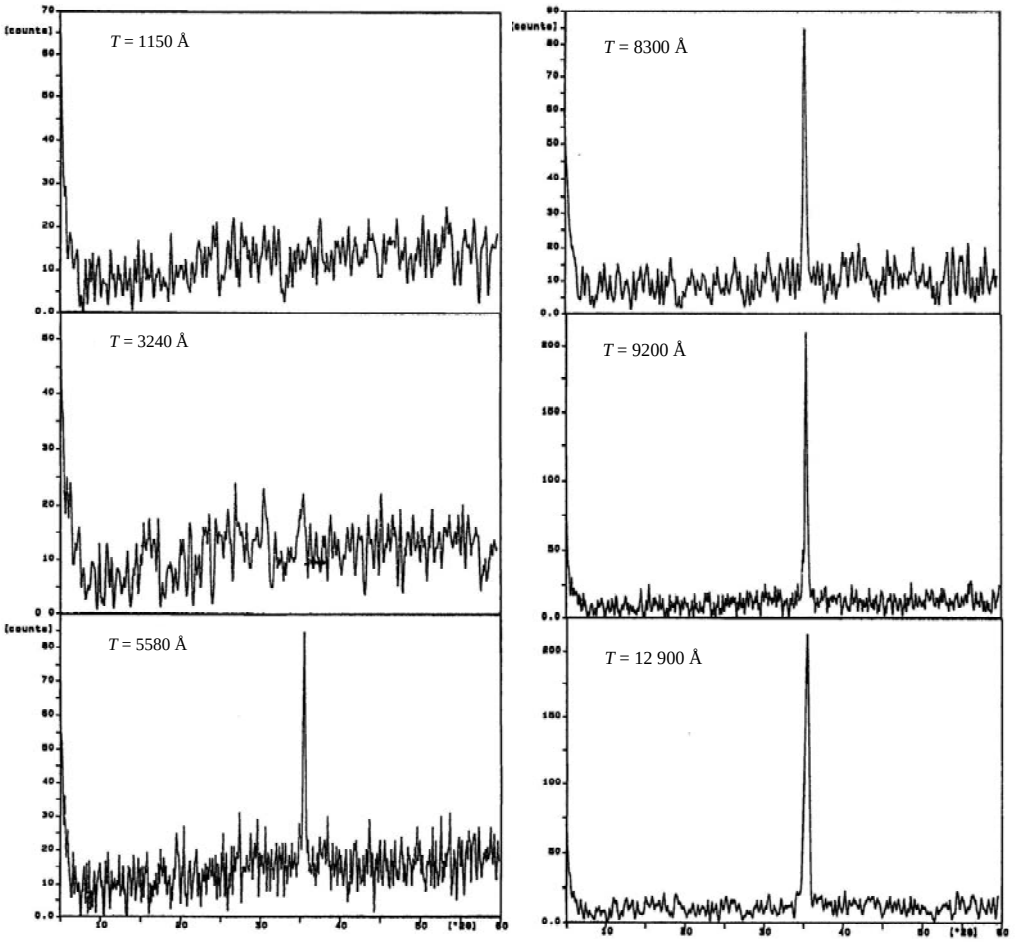

Fig. 1. Variation of X-ray diffraction patterns of F doped indium oxide thin films with thickness

Figure 3 shows the change in the average transmission (at a wavelength of 550 nm) of a series of In_2O_3:F thin films with increasing thickness. The results show that the transparency of the films decreases to a value of 70% for films having a thickness of 1300 nm.

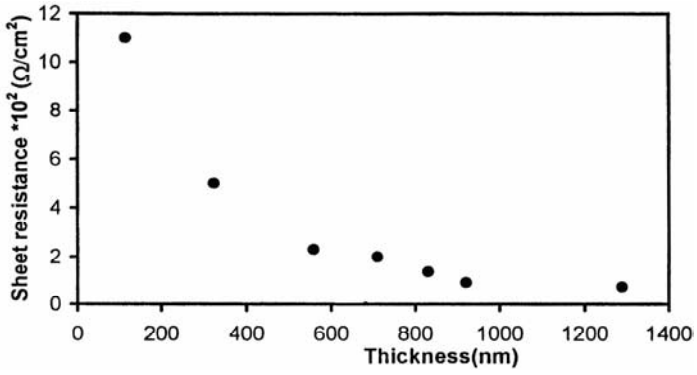

Fig. 2. Variation of room temperature sheet resistance of F-doped indium oxide thin films with thickness

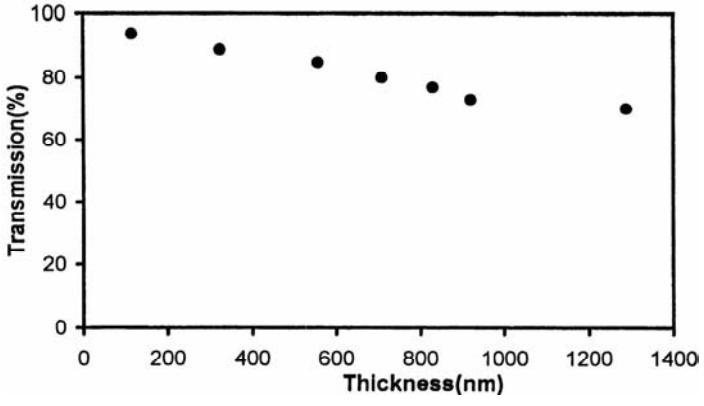

Figure 3. Variation of visible transparency of F-doped indium oxide thin films with thickness

4. Conclusions

Transparent conducting In_2O_3:F films have been prepared using the spray pyrolysis technique on glass substrate with varying the thickness. We observed that the physical properties of coated films can be improved by increasing film thickness. This results in a decrease in sheet resistance and nearly saturates at a thickness of about 600 nm. A further increase in thickness results in a decrease of the optical transmission. The structure of the films was revealed by XRD. All films exhibited a preferred orientation along the [400] direction. Films deposited with a thickness below 300 nm showed an amorphous structure.

Acknowledgement

This work was supported by the Department of Research of the University of Guilan. The authors are grateful to Professor Zanjanchi, Head of the Higher Education Department, for using the X-ray system.

References

[1] PARAGUAY F., MIKI-YOSHIDA M., MORALES J., SOLIS J., ESTRADA W., Thin Solid Films, 373 (2000), 137.
[2] HAGEROTT M., XIE W., GRILLO D.C., KOBAYASHI M., GUNSHOR R.L., Appl. Phys. Lett., 60 (1992), 2825.
[3] KIM H., HORWITZ J.S., KUSHTO G.P., QADRI S.B., KAFAFI Z.H., CHRISY D.B., Appl. Phys. Lett., 78 (2001), 1050.
[4] HARTNAGEL H.L., DAWAR A.L., JAIN A.K., JAGADISH C., *Semiconducting Transparent Thin Films*, Institute of Physics Publ., Bristol, UK,1995.
[5] COUTTS T.J, YOUNG D.L., LI X., MRS Bull., 25 (2000), 56.
[6] COUTTS T.J., MASON T.O., PERKINS J.D., GINLEY D.S., Proceeding of the Int. Symposium on Photo-voltaic for the 21st Century, USA, 99 (1999), p. 274.
[7] COUTTS T.J., YOUNG D.L., LI X., MULLIGAN W.P., WU X., J. Vac. Sci. Technol., A. Vac. Surf. Films, 18 (2000), 2646.
[8] TANG B.T., YU Q.X., LEE H.Y., LEE C.T., Mat. Sci. Eng., B82 (2000), 259.
[9] NUNES P., FORTUNATO E., TONELLO P., FORTUNATO F.B., VILARINHO P., MARTINS R., Vacuum, 64 (2002), 281.
[10] FRANK G. KAUER E., KOSTLIN H., Thin Solid Films, 77 (1991), 107.
[11] ROZATI S.M,, GANJ T., Renewable Energy (accepted for publication).
[12] MANIFACIER J.C., FILLARD J.P., BIND J.M., Thin Solid Films, 77 (1981), 67.
[13] AGASHE C., TAKWALE M.G., MARATHE B.R., BHIDE V.G., Solar Energy Mat., 17 (1988), 99.
[14] CHAUDHURI U.R., RAMKUMA K., SATYAM M., J. Phys. D: Appl.Phys., 22 (1989), 1413.
[15] MARTINEZ M.A., HERRERO J., GUTIERREZ M.T., Solar Energy Mat. Solar Cells, 31 (1994), 489.

Received 7 January 2004
Revised 10 February 2004

Materials Science-Poland, Vol. 22, No. 2, 2004

Photoelectrochemical properties of sol-gel derived TiO_2 thin films in aqueous sodium oxalate solution

ZULKARNAIN ZAINAL*, CHONG YONG LEE, MOHD ZOBIR HUSSEIN, ANUAR KASSIM

Department of Chemistry, Faculty of Science and Environmental Studies, Universiti Putra Malaysia, 43400 UPM Serdang, Selangor Darul Ehsan,Malaysia

Photoelectrooxidation of aqueous sodium oxalate on TiO_2 thin films has been investigated. The films, prepared by sol-gel dip-coating, were characterised using Scanning Electron Microscopy and X-ray Diffractometry. Photosensitivity of samples was studied using Linear Sweep Voltammetry and Chrono-amperometry techniques. The photoelectrochemical performance of thin film electrodes was evaluated in function of heat treatment, number of dip-coatings and applied potential. The percentage of oxalate degradation was determined by calculating the total charge from the photocurrent. The films heat-treated at 773 K were better fitted to indirect optical transition with E_g = 3.21 eV.

Key words*: photooxidation; TiO_2; sol-gel; sodium oxalate; titanium substrate*

1. Introduction

Sodium oxalate is a major toxic impurity in liquid alumina processing. It must be continuously removed, because it induces problems that lead to low-quality metallurgical alumina due to particle attrition [1]. Additionally, low solubility of sodium oxalate in liquid makes it easy to crystallize during alumina precipitation. This interference with agglomeration leads to an increased generation of unwanted fine alumina trihydrate [2].

Several techniques for the causticization of sodium oxalate have been reported, including physical separation, microbiological processes and other conventional thermal pathways using ambient temperature and pressure [3–5]. Among them, photocatalytic destruction of organic pollutants has emerged as the most attractive method during water purification, since it can lead to a complete mineralization of toxic compounds into unharmful products such as H_2O, CO_2, and other inorganic substances [6]. Many semiconductors, such as TiO_2, WO_3, SrO_2, ZrO_2, ZnO, Fe_2O_3, CeO_2, CdS and ZnS

* Corresponding author, email: zulkar@fsas.upm.edu.my.

[6,7], have been investigated in terms of their catalytic properties in photocatalytic degradation of a wide variety of environmental contaminants. Among these semiconductors, TiO_2 has been proven to be an excellent photocatalyst in this particular field [6,7].

Nevertheless, most of the studies on photocatalytic oxidation of sodium oxalate use TiO_2 slurry [1–2, 5, 8], while very few studies on thin film photocatalysts exist [9]. In this work, we studied TiO_2 thin films prepared by the sol-gel dip-coating method. This immobilization method is more preferable than the slurry or suspension systems, due to easy and convenient catalyst handling – the need of post-treating to separate the catalyst from the reaction mixture has been eliminated [10]. In addition, TiO_2 can be induced electrochemically when supported on electrically conducting substrates [11–13]. Thus, characteristics of the films under applied external bias potential could be investigated. The effects of various operational parameters such as heat-treatment temperature, number of dip-coating layers and applied potential were studied.

2. Experimental

2.1. Materials

All chemicals, namely sodium oxalate (Fisher, 99.5%), tetraisopropyl orthotitanate (>98% Ti, Merck-Schuchardt), ethanol (Analytical reagent grade, GmbH Chemical) and nitric acid (BDH, 69 %) were used without further purification. All solutions in this experiment were prepared using deionized water (Milipore Alpha Q system, 18.2 MΩ·cm).

2.2. Sample preparation

The sol-gel samples were prepared by adding 1 ml of concentrated nitric acid to 200 ml of water, followed by 28.1 g of tetraisopropyl orthotitanate in 10 ml of ethanol. The mixture was stirred with a magnetic stirrer for 5–6 days to obtain a thick hydrolyzate. The substrate – titanium plates (Aldrich Chemical Company, 0.25 mm thick, 99.7%) – were cut into discs 1.00 cm in diameter and polished with silicon carbide paper (a bioanalytical system PK-4 polishing kit). The plates were rinsed in an ethanol bath before use. TiO_2 films were obtained by manually dipping the titanium plates in the hydrolyzate for a few seconds and leaving them to dry at room temperature. Then the coated plates were heated at 373 K for 5 min in an oven, followed by the dip-coating procedure. This was repeated several times, until the desired number of coatings was obtained. Finally, the plates were heat-treated in a Thermolyne 21100 furnace at temperatures ranging from 373 K to 773 K for two hours to obtain titanium dioxide films**.**

2.3. Analytical measurements

A potentiostat EG&G Princeton Applied Research (PAR) VersaStat, driven by a model 270 electrochemical Analysis System Software, was used in the electrochemical and photoelectrochemical measurements. These measurements were carried out in a standard electrochemical cell. The working electrode was made by mounting the TiO_2 coated titanium plates onto a Teflon electrode holder. The exposed area was about 0.64 cm^2. The other electrodes were: Ag/AgCl (0.222V vs. NHE) as a reference electrode, and platinum as a counter electrode. All the experiments were carried out using 0.01 M sodium oxalate as the electrolyte. Two light sources were used to excite the TiO_2 electrode: a tungsten halogen projector lamp (Osram, 300 W and 120 V) and a UV light beam (BlackRay model 100AP, PAR38 mercury lamp 100 W). The light source was placed 15 cm from the sample. All measurements were carried out at room temperature, approximately 298 K.

Scanning electron microscope measurements (SEM) were performed with a SEM JSM 6400 JEOL Scanning Microscope. The morphology and surface characteristics of the coated TiO_2 on the substrate were analyzed. Gold coatings were applied to the samples before running the SEM experiments by using a BIO-RAS sputter coater. X-ray diffractometry (XRD) analysis was employed to study the structure of TiO_2 layers coated on titanium surfaces. These measurements were performed using a Shimadzu XRD 6000 diffractometer or a Siemens D-5000 Diffractometer for 2θ ranging from 5° to 60°, with an Ni-filter and CuK_α beam (λ = 1.54056 Å). Optical absorption studies were carried out using a Perkin Elmer UV/Vis Lambda 20 Spectrophotometer. The coated ITO glass plates were placed across the radiation pathway while an uncoated ITO glass plate was put across the reference channel. The band gap energy E_g was determined from an analysis of the absorption spectra.

3. Results and discussion

3.1. Morphology of the TiO_2 electrode

Figure 1 shows scanning electron micrographs of the heat-treated films. Cracks appeared on the surface of the film after treatment at 373 K. The occurrence of cracks during the gel drying process was due to large differential evaporation, large stress and variation in gel pore size [14]. Upon heating at 473 K and 573 K, the thermal gradients result in breaking the particles further into inhomogeneous forms. This occurred accompanying dehydration and decomposition of organic compounds [15]. Heat treatment at 673 K resulted in the formation of aggregates. These aggregates were transformed into a well formed and better covered layer at 773 K.

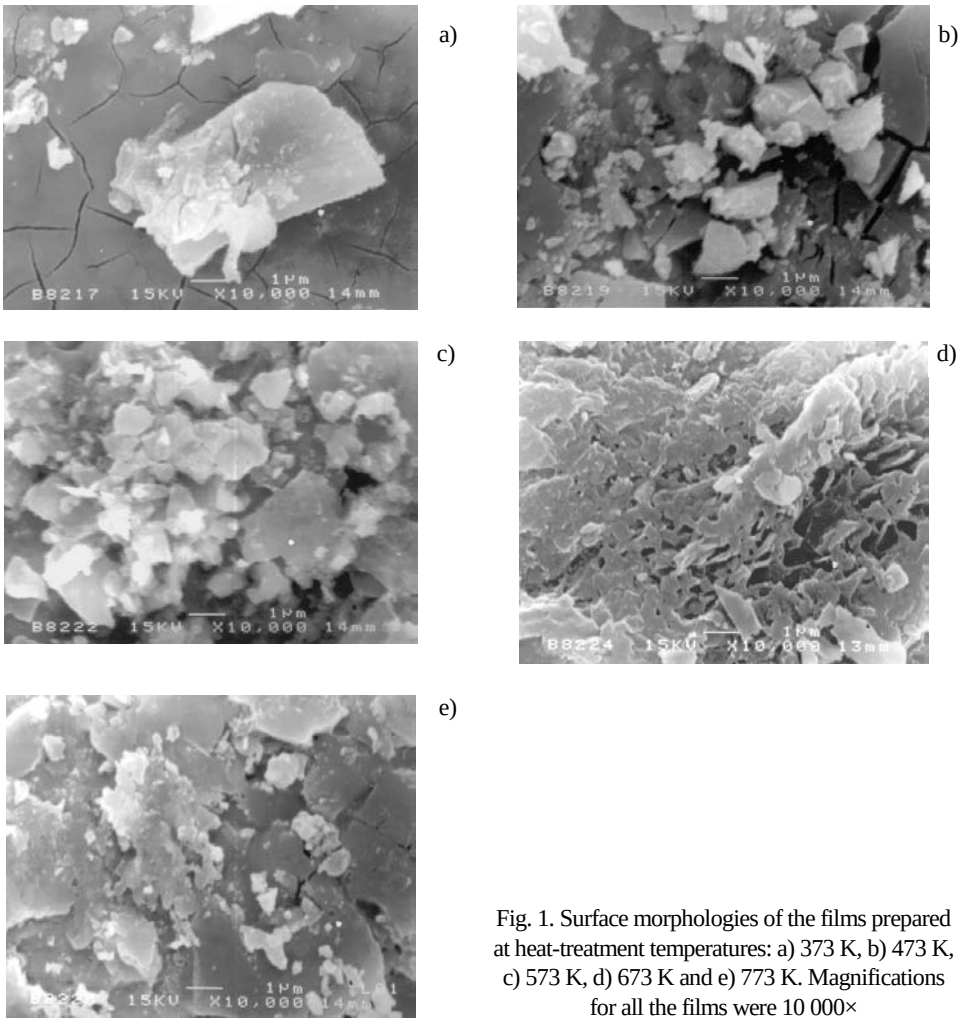

Fig. 1. Surface morphologies of the films prepared at heat-treatment temperatures: a) 373 K, b) 473 K, c) 573 K, d) 673 K and e) 773 K. Magnifications for all the films were 10 000×

3.2. X-ray Diffraction measurements

XRD data for films heat-treated at various temperatures are shown in Fig. 2. Apart from substrate (Ti) peaks, no other peaks were obtained at 573 K and below. Even though the intensity of the sample peaks is rather weak due to the nature of the thin films, the peaks belonging to TiO_2 existed when the samples were heated at 673 K and higher temperatures. The typical peak at d = 3.52 Å, which corresponds to the (101) plane of anatase TiO_2, was detected for samples heated at 673 K and 773 K. Heat treatment at 773 K improved film crystallinity and resulted in the appearance of another peak at d = 3.25 Å, which corresponds to the (110) plane of rutile TiO_2.

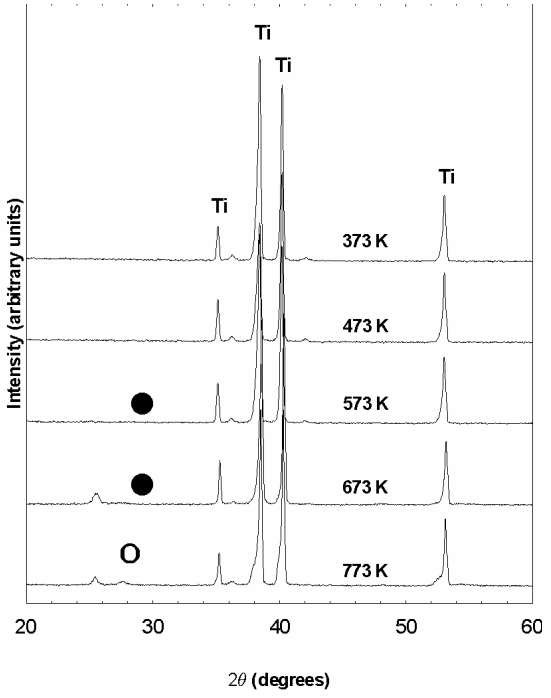

Fig. 2. The XRD pattern of films heat-treated at temperature of 373 K to 773 K (● = Anatase, ○ = Rutile, Ti = Titanium)

3.3. Effect of heat treatment

The photocurrent behaviour of the heat-treated samples was investigated by irradiation with a halogen and near-UV lamp. The photocurrents are dependent on the heat treatment temperature, as shown in Fig. 3a and b. Very strong photocurrents were observed for the electrode heated at 773 K as compared to the samples heated at 673 K and below. This indicates that more photoactive samples were obtained by heat-treating.

The photocurrent of thin-film electrodes is affected by several factors, including crystallinity, film resistance and electrode area [16]. It seems that the crystallinity contributes significantly to the photocurrent efficiency. X-ray diffraction results show that TiO_2 signals were only detected after the films were heat-treated at 673 K. The sample heated at 773 K which showed the presence of the anatase and rutile phases was found to be more photoactive compared to the sample heated at 673 K, which contained the anatase phase only.

Increase of the photocurrent may be due to a decrease in the film resistance. If the bulk resistance is too high, the quantum efficiency will become lower due to a decrease of the electrical gradient across the depletion and thin space charge layer [16, 17]. When a higher temperature was applied, a strong adhesion between the film

and substrate was achieved, successfully reducing the bulk resistance. The reduction of Ti^{4+} to Ti^{3+} in the film by decomposed organic matter or unburned free carbons during the heating process is also believed to contribute to the decrease of film resistance. The presence of Ti^{3+} ions would dominate both the photoelectrochemical reaction at the surface and bulk electrical conductivity by forming donor levels in the conduction band of TiO_2 [16, 18].

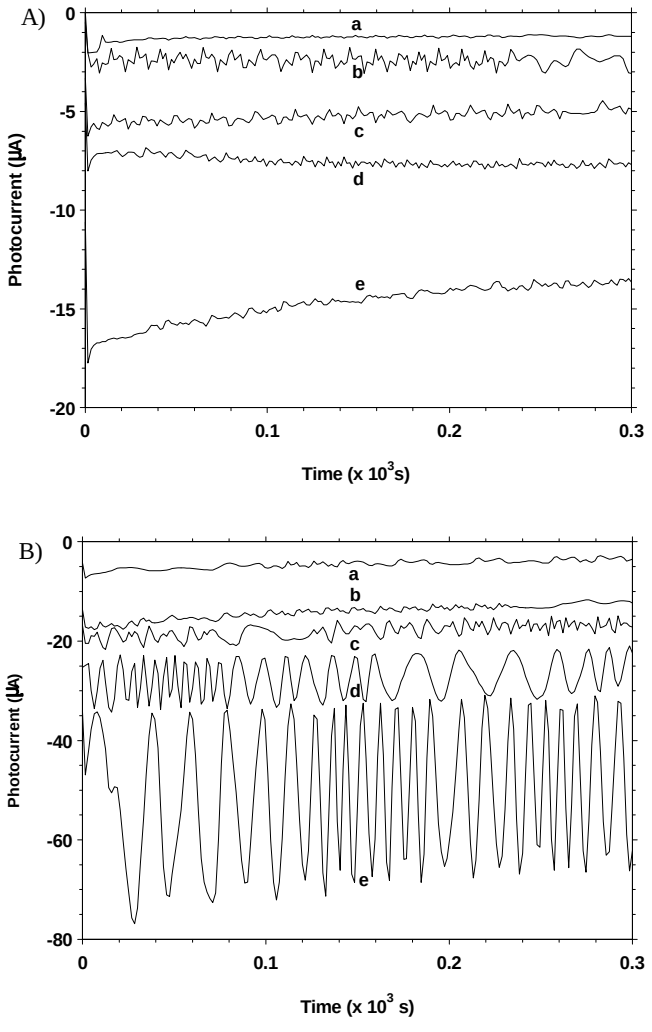

Fig. 3. Comparison of the photocurrent values for electrodes prepared at different heat-treatment temperatures under illumination of halogen lamp (A) and UV lamp (B): a) 373 K, b) 473 K, c) 573 K, d) 673 K and e) 773 K, potential fixed at 0.8 V

The results presented in Fig. 3 also compare the efficiency of generating the photocurrent with halogen and UV lamp sources. The value of photocurrent for films

illuminated with the UV lamp is much higher than that observed for the halogen lamp. Light from the halogen lamp is less efficient in promoting charge carrier activity in the films compared to UV light. This is related with the number of photons with the energy exceeding the band gap energy of TiO_2 (E_g > 3.2 eV) for each light source. Light from the near UV lamp contains more of these, and thus can better excite TiO_2 [19]. Although UV lamps are appropriate light sources for activating TiO_2 films, other light sources such as halogen lamps should also be considered to avoid the hazardous effects of UV radiation.

3.4. Effect of potential applied

The effect of the applied bias potential on the behaviour of electrodes heat treated at 773 K is shown in Fig. 4. Photocurrent values were obtained by measuring the difference between the current under illumination (I_p) and without illumination (I_d). The results show that the photocurrent increases with the applied potential when the samples are illuminated with a UV lamp.

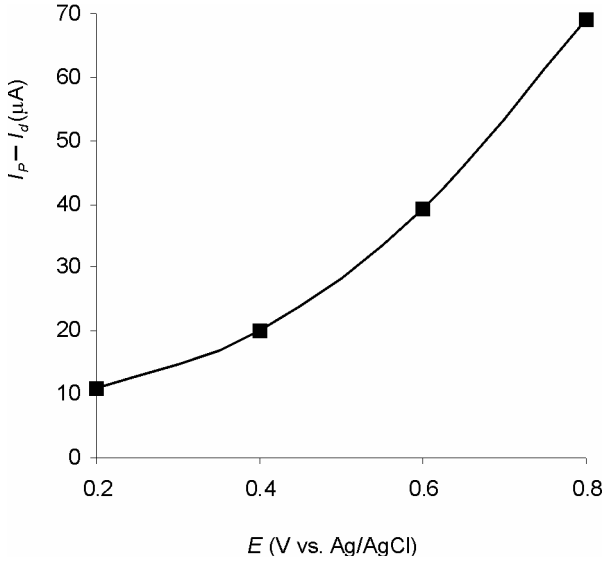

Fig. 4. Comparison of the photocurrent values of the films at potentials of 0.2–0.8 V under UV illumination

The photoactivity of the film increased when a higher potential was applied. This is because application of the anodic bias provides a potential gradient within the film, which drives the photogenerated holes and electrons in different directions [20, 21]. This can reduce the charge recombination of electrons and holes, stimulating the photooxidation process. Here, we propose the following mechanism for the photocatalytic oxidation of sodium oxalate in this electrochemical system.

In solution:

$$Na_2C_2O_4 \rightarrow 2Na^+ + C_2O_4^{2-} \quad (1)$$

At the working electrode:

$$TiO_2/Ti + h\nu \rightarrow TiO_2/Ti\left(e_{cb}^- ... h_{vb}^-\right) \quad (2)$$

$$(h^+)_{surf} + H_2O \rightarrow OH^\bullet + H^+ \quad (3)$$

$$(h^+)_{surf} + C_2O_4^{2-} \rightarrow C_2O_4^- \quad (4)$$

$$OH^\bullet + C_2O_4^- \rightarrow HCO_3^- + CO_2 \quad (5)$$

$$(h^+)_{surf} + HCO_3^- \rightarrow CO_2 + OH^- \quad (6)$$

$$TiO_2/Ti\left(e_{cb}^- ... h_{vb}^-\right) \rightarrow TiO_2/Ti + \text{heat} \quad (7)$$

At the counter electrode:

$$2H_2O + 2e^- \rightarrow H_2 + 2OH^- \quad (8)$$

Equation (1) shows the homogenous dissociation process of oxalate in water. The electron–hole recombination step (Eq. (8)) was suppressed by electron drive from the TiO_2 thin film electrode to the counter electrode (Eq. (7)). In consequence, more reactive holes are made available for the photooxidation of oxalate.

3.5. Effect of the number of dip-coatings

The photocurrent behaviour of the samples under UV lamp illumination with different numbers of dip-coated layers is shown in Fig. 5. The maximum number of layers was 7, because the catalyst began to peel off from the substrate after heat-treating of samples with a larger number of layers. As shown in Fig. 5, the photocurrent increased with the number of layers and reached 20 μA for 7 layers. This result suggests that the photocurrent strongly depends on the thickness of the film. An increase of thickness provides more active sites for the oxidation of oxalate.

In addition, the film thickness greatly affected the effectiveness of the bias potential applied to the film. This is due to the creation of the space-charge region as a region of potential variation, which makes electron movement in semiconductors easier. When the thickness of the film is low (e.g., only 1 layer), the density of carriers in the film is not large enough to generate a high electrical field at the space charge region,

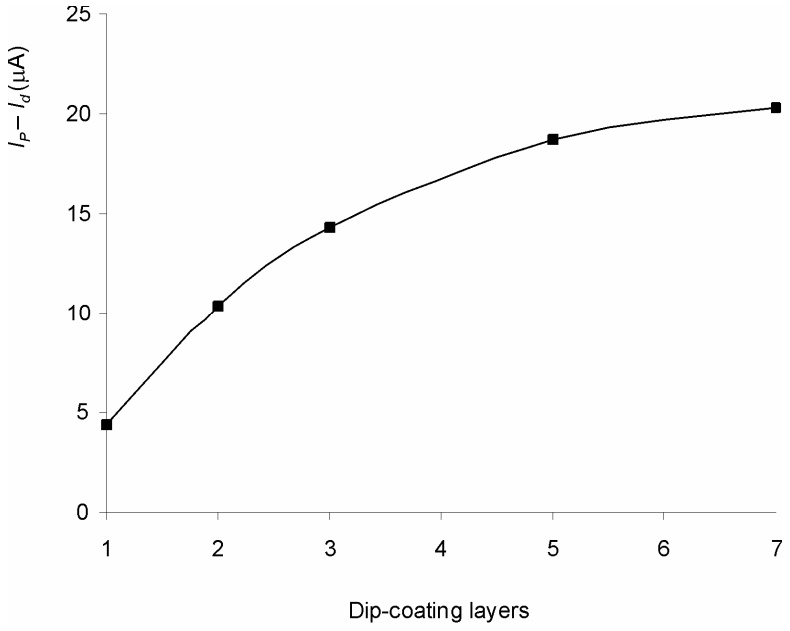

Fig. 5. The photocurrent values of the electrodes prepared with different number of dip-coating layers. Potential was fixed at 0.4 V and the illumination source is UV lamp

which results in a low photocurrent [17]. Contrary to this, an increase of the carrier density with the increase in film thickness would generate a high electrical field in the space charge layer. The photocurrent almost reaches saturation for films coated 5 and 7 times. This limitation could be overcome by applying higher light intensities and higher bias potentials.

3.6. Percentage of oxalate ions oxidised

The efficiency of oxalate oxidising during 5 min was studied under the illumination of a UV lamp using electrodes heat-treated at different temperatures. The efficiency of oxalate oxidation was calculated based on the total amount of charge produced during the experiment. The oxidation of an oxalate ion $C_2O_4^{2-}$ producing CO_2 gas is a well known two-electron process. The photocatalytic oxidation of oxalate is not complicated by the production of an intermediate species [9]. The oxidation process is:

$$^{-}OOC–COO^{-} \rightarrow 2CO_2 + 2e^{-} \tag{9}$$

Table 1 shows that the amount of oxalate ions oxidized increases with the electrode heat-treatment temperature.

Table 1. The percentage of oxalate ions oxidised during 5 min under irradiation of UV lamp on heat-treated electrodes

Light source	Heating temperature/K	Amount of charge/C	Amount of oxalate oxidised/μmol	Oxidised percentage/%
UV lamp	373	1.423	7.37	0.92
	473	4.420	22.90	2.86
	573	5.625	29.15	3.64
	673	8.554	44.32	5.54
	773	15.970	82.75	10.32

3.7. Band-gap study

The UV-Vis spectrum was obtained from TiO_2 deposited on ITO glass, which was heat-treated at 737 K. Data obtained from the optical absorbance vs. wavelength were introduced into the following relationship for near-edge absorption:

$$A = \frac{k\,(h\nu - E_g)^{n/2}}{h\nu}$$

where ν is frequency, h is the Planck constant, k is a constant, while n has the value of either 1 or 4. The bandgap energy E_g could be obtained from a straight line plot of $(Ah\nu)^{2/n}$ as a function of $h\nu$. An extrapolation of the value of $(Ah\nu)^{2/n}$ to zero gives E_g. A straight line obtained for $n = 1$ indicates a direct electron transition between the states of the semiconductor. The transition is indirect if a straight line is obtained for $n = 4$.

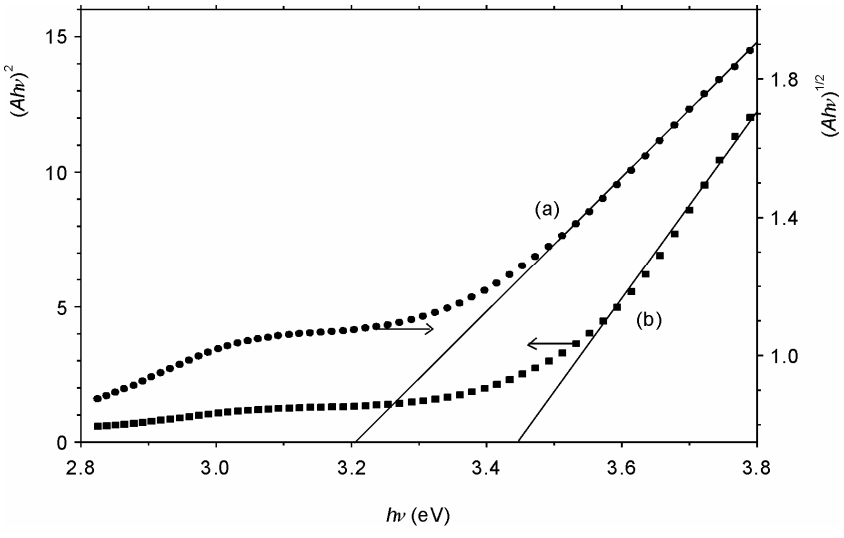

Fig. 6. Plot of $(Ah\nu)^{2/n}$ vs. $h\nu$ for the film prepared at temperature of 773 K with: a) $n = 4$, b) $n = 1$

As is seen in Fig. 6, the data plotted in coordinates expected of direct and indirect transitions yielded bandgap values of 3.45 and 3.21 eV, respectively. The linear relationship is better fitted for the indirect than direct transition. Therefore, it could be concluded that the indirect transition model is more appropriate. Similar results were also reported elsewhere [17, 22].

4. Conclusions

The results showed that the photoelectrochemical properties of TiO_2 thin film electrodes prepared by sol-gel dip-coating depend on heat-treatment temperature, on the number of dip-coated layers and on the potential applied. The largest photocurrent was achieved for films heat-treated at a temperature of 773 K. Higher percentages of oxalate oxidation were achieved when using such films with UV lamp illumination. These results indicate the significance of electrode preparation and the light source for the generation of the photocurrent. The film heat-treated at 773 K was found to be better fitted by an indirect optical transition, with bandgap energy of 3.21 eV.

Acknowledgements

We gratefully acknowledge the financial support from the Malaysian Government through the IRPA programme no: 09-02-04-0255-EA001 and 09-02-04-0369-EA001.

References

[1] WANG H., ADESINA A.A., Appl. Catal. B: Environ., 14 (1997), 241.
[2] BANGUN J., ADESINA A.A., Appl. Catal. A: General., 175 (1997), 221.
[3] OLLIS D.F., PELIZZETTI E., SERPONE N., Environ. Sci. Technol., 25 (1991), 1523.
[4] PELIZZETTI E., SERPONE N. (Eds), *Photocatalyst: Fundamental and Applications*, Wiley, New York, 1991.
[5] PAREEK V., BRUNGS M.P., ADESINA A.A., Adv. Env. Res., 7 (2002), 411.
[6] HOFFMAN M.R., MARTIN S.T., CHOI W.Y., BAHNEMANN D.W., Chem. Rev., 95 (1995), 69.
[7] NEPPOLIAN B., CHOI H.C., SAKTHIVEL S., ARABINDOO B., MURUGESAN V., J. Hazardous Materials, B89 (2002), 303.
[8] LEA J., ADESINA A.A., Chem. Eng. Sci., 54 (1999), 2209.
[9] BRYNE J.A., EGGINS B.R., J. Electroanal. Chem., 457 (1998), 61.
[10] BRYNE J.A., EGGINS B.R., BROWN N.M.D., MCKINNEY B., ROUSE M., Appl. Catal. B: Environ., 17 (1998), 25.
[11] LI X.Z., LI F.B., FAN C.M., SUN Y.P., Water. Res., 36 (2002), 2215.
[12] HIDAKA H., SHIMURA T., AJISAKA K., HORIKOSHI S., ZHAO J., SERPONE N., J. Photochem. Photobiol. A: Chem., 109 (1997), 165.
[13] VINODGOPAL K., KAMAT P.V., Sol. Energy Mater. Sol. Cells, 38 (1995), 401.
[14] ULRICH D.R., Chemtech (1988) April 242.
[15] COLOMER M.T., JURADO J.R., Chem. Materials, 12 (2000), 923.
[16] YOKO T., YUASA A., KAMIYA K., SAKKA. S., J. Electrochem. Soc., 138 (1991), 2279.
[17] YOKO T., HU L., KOZUKA H., SAKKA S., Thin Solid Films, 283 (1996), 188.

[18] MIZUSHIMA K., TANAKA M., ASAI A., IIDA S., GOODENOUGH J.B., J. Phys. Chem. Solids, 40 (1979), 1129.
[19] MIKULA M., BLEACHA J., CEPPAN M., J. Electrochem. Soc., 139 (1992), 3470.
[20] VINODGOPAL K., HOTCHANDANI S., KAMAT P.V., J. Phys. Chem., 97 (1993), 9040.
[21] VINODGOPAL K., STAFFORD U., GRAY K.A., KAMAT P.V., J. Phys. Chem., 98 (1994), 6797.
[22] POZNYAK S.K., TALAPIN D.V., KULAK, A.I., J. Phys. Chem. B, 105 (2001), 4816.

Received 25 February 2004
Revised 16 April 2004

Materials Science-Poland, Vol. 22, No. 2, 2004

Yttrium iron garnet surface modification during pulsed laser ablation deposition

NOOR BAA'YAH IBRAHIM[1*], CHRIS EDWARDS[2], STUART B. PALMER[2]

[1]PPFG, Fakulti Sains dan Teknologi, Universiti Kebangsaan Malaysia, 43600 Bangi, Selangor, Malaysia

[2]Department of Physics, University of Warwick Coventry CV4 7AL, United Kingdom

This paper reports on the formation of cone-like structures on yttrium iron garnet (YIG) targets during the ablation of YIG thin films. Energy dipersive X-ray analysis (EDS) performed in the targets show that the cones are rich in yttrium.

Key words: *PLAD; surface modification; YIG*

1. Introduction

Pulsed laser ablation deposition (PLAD) has become a popular technique for the preparation of various kinds of thin films of metals, chemical compounds and organic materials [1]. This technique has many advantages: it can easily produce thin films from materials with high melting points and it can produce thin films with compositions similar to the target material compositions. Despite these advantages, one of the disadvantages is that the ablation rate can be influenced by cone-like structures, which form on the surface of an ablation target during ablation [2]. Dyer et al. [3] studied laser cone formation on polyimide films and showed how seeding with impurities affected their formation. The high-temperature superconductor – yttrium-barium-copper oxide (YBCO) has been extensively studied by Foltyn et al. [4, 5] who suggested that vaporization-resistant impurities are responsible for the cone formation. They demonstrated that the cone tips are rich in yttrium. With incongruent melting compounds like YBCO or Yittrium Iron Garnet (YIG) surface segregation can occur with the resolidification of higher melting components such as Y_2O_3 [6].

This paper reports the study of cone formation on YIG targets due to ablation.

*Corresponding author, e-mail: baayah@pkrisc.cc.ukm.my.

2. Experimental details

YIG ($Y_3Fe_5O_{12}$) targets were prepared using conventional ceramic methods as reported by Ibrahim et al. [7]. The laser used was a Lambda Physik Excimer (LPX100) XeCl laser (λ = 308 nm and repetition rate – 21 Hz). It hit the target at an incidence angle of 45°. Laser fluence was 1 J·cm^{-2}. During the process of ablation the laser was moved horizontally by wobbling lens.

An optical microscope and scanning electron microscope (SEM) were used to study the surface morphologies of the unablated and ablated YIG targets. X-ray analysis of the targets was done using energy dispersive X-ray analysis (EDS).

3. Results and discussion

Optical micrographs in Fig. 1 show three different stages of cone formation. Shallow ripple-like structures occur at the edge of the ablated area, which become deeper as the laser damage increases and eventually full cones develop.

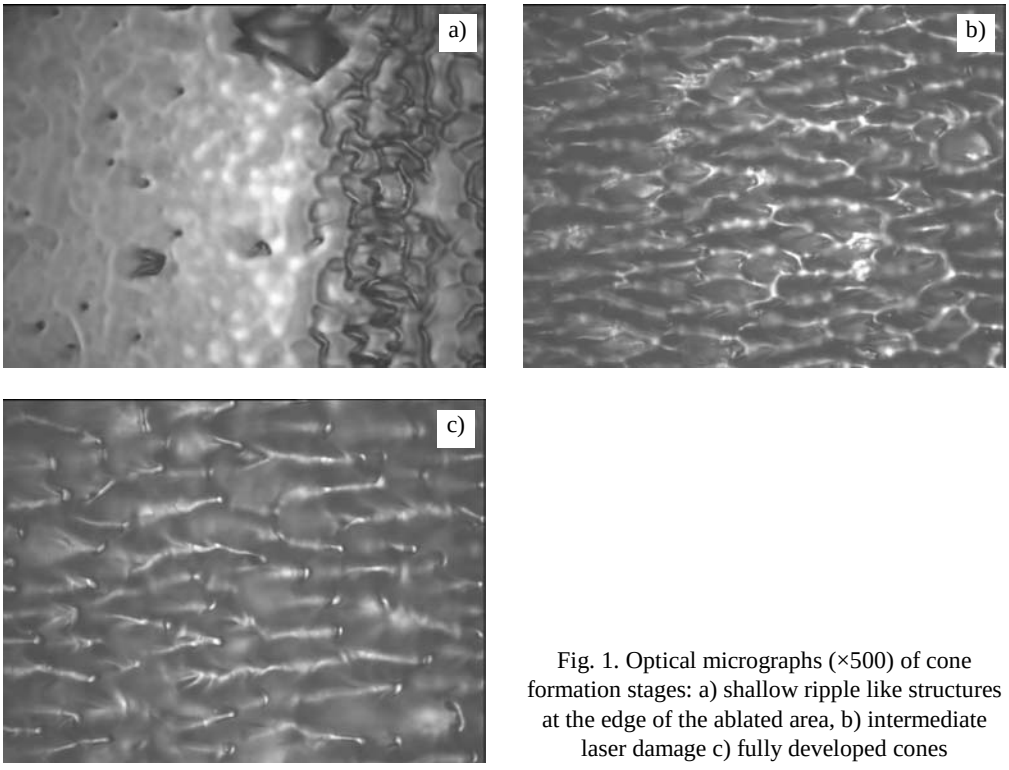

Fig. 1. Optical micrographs (×500) of cone formation stages: a) shallow ripple like structures at the edge of the ablated area, b) intermediate laser damage c) fully developed cones

Figures 2a and b show SEM micrographs of the YIG target before (×1700 magnification) and after ablation (×200 magnification). The surface has cone-like structures

approximately 70 μm long and 30 μm wide, and the surfaces of these structures are smooth (the facetted structure is caused by the resolution of the digital photograph and printer). The ablated target was hit with ~30 000 shots per site and heated to 500 °C during ablation. The number of laser shots per site was calculated by multiplying the total number of laser pulses by the ratio of beam area to total exposed area. The cone axes are not normal to the surface; they appear to be lying at an angle. Similar cone structures have been observed by several researchers on YBCO targets [4, 5, 8] and on aluminium [9]. They observed that the cones point towards the laser beam. As the beam in this study is incident at 45° to the target, they would be expected to form at 45° to the surface of the YIG targets. Figure 3 shows a cone under higher magnification. It has a rounded surface with some evidence of flowing, which indicates that the surface has been in a liquid state.

To study the nature of the cones on YIG, EDS analysis was done on the unablated and ablated targets. Figures 4 a and b show the results. They indicate that the ablated target contains more yttrium and less iron (49%Fe_2O_3:51%Y_2O_3) as compared to the unablated target (67%Fe_2O_3:33%Y_2O_3). This yttrium enrichment may be due to the incongruent melting of YIG.

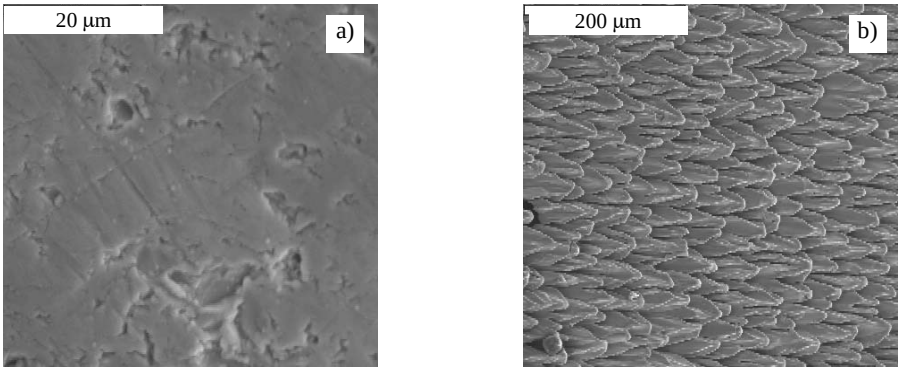

Fig. 2. SEM micrographs of YIG target: a) unablated target, b) ablated target showing cone structures

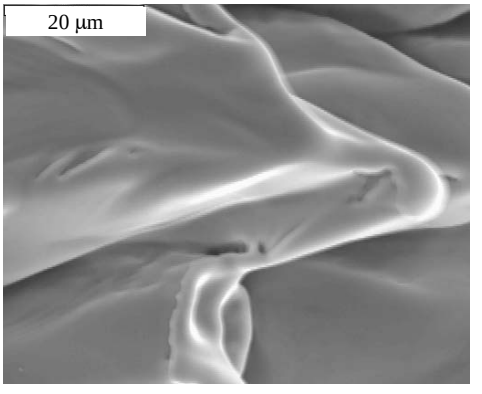

Fig. 3. Close-up SEM micrograph of ablated YIG target

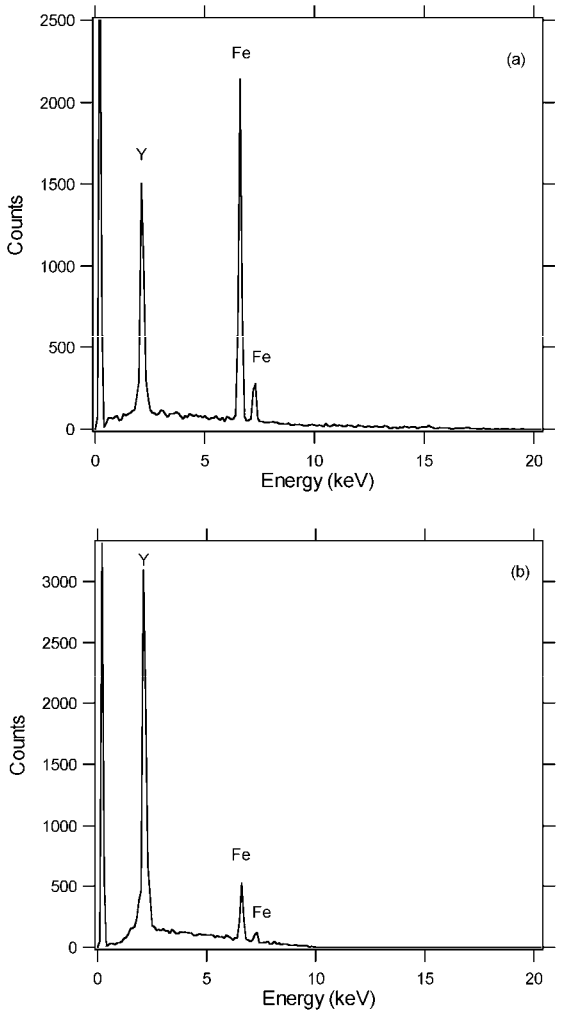

Fig. 4. SEM X-ray analysis of YIG target:
a) before ablation, b) after ablation (~30 000 shots/site)

A similar yttrium enrichment process has also been observed on YBCO targets, which also melt incongruently [4, 5]. The laser rapidly heats the target to form a very high-temperature plasma. Some liquid will be present on the target's surface, and this will cool between laser pulses and resolidify. As the resolidification process on the YBCO target begins, Y_2O_3, the solid phase with the higher melting point will tend to freeze first, leading to yttrium enrichment [6]. This segregation does not occur significantly in a single ablation pulse, but when the process is repeated thousands of times during an ablation. As Y enrichment proceeds, the laser will begin to interact with the transparent material (Y_2O_3 is used for UV optics) [2]. The Y rich material then shields the underlying material, leading to cone formation and an decrease in the ablation rate.

YIG melts incongruently to form liquid and yttrium orthoferrite ($YFeO_3$). In this case, $YFeO_3$ is the solid phase with the higher melting point, and will tend to freeze first, leading to yttrium enrichment and cone formation. The cones have larger surface area than the original target; the laser's fluence is therefore lowered, leading to a reduction in the ablation rate. This effect was visible during ablation, as there was a noticeable decrease in the size of the ablation plume after approximately half an hour. Foltyn et al. [4] reported a drop in the deposition rate by a factor of 4 after 1000 laser shots per site for YBCO targets. Krajnovich and Vasquez [10] reported that the reduction trend stops when cones have completely formed on excimer irradiated polymers.

As the formation of these cones reduces the film deposition rate, we suggest using an adjustable mirror to move the laser beam to a fresh area of the target whenever there is a noticeable decrease in the size of ablation plume.

4. Conclusions

Cone-like structures and yttrium enrichment processes have been observed on YIG ablation pellets. Cone formation reduces the ablation rate. This is believed to be the first report of cone structures on ablated YIG targets.

Acknowledgement

The authors would like to thank all those who have been involved in this project.

References

[1] SOCOL G., TORRICELLI P., BRACCO B., ILLIESCU M., MIROIU F., BIGI A., WRECKMANN J., MIHAILESCU I.N., Biomaterials, 25 (2004), 2539.
[2] FOLTYN S.R., *Surface Modification of Materials By Cumulative Laser Irradiation*, [in:] D.B. Chrisey and G.K. Hubler (Eds.), *Pulsed Laser Deposition of Thin Films*, Wiley, New York, 1994, p. 89.
[3] DYER P.E., JENKINS S.D., SIDHU J., Appl. Phys. Lett., 49 (1986), 453.
[4] FOLTYN S. R., MUENCHAUSEN R.E., ESTLER R.C., PETERSON E., HUTCHINSON W.B., OTT K.C., NOGAR N.S., HUBBARD K.M., DYER R.C., WU K.D., Mater. Res. Soc. Symp. Proc., 191 (1990), 205.
[5] FOLTYN S.R., DYER R.C., OTT K.C, PETERSON E., HUBBARD K.M., HUTCHINSON W., MUENCHAUSEN R.E., ESTLER R.C., WU X.D., Appl. Phys. Lett., 59 (1991), 594.
[6] OSWLAGE T. AND KEEFER K., J. Mater. Res., 3 (1988), 1279.
[7] IBRAHIM N.B., EDWARDS C., PALMER S.B., J. Magn. Magn. Mat., 220 (2000), 183.
[8] AUCIELLO O., KRAUSS A.R., SANTIAGO-AVILES J., SCHREINER A. F., GRUEN D.M., Appl. Phys. Lett., 52 (1988), 239.
[9] KELLY R., ROTHENBERG J.E., Nucl. Instrum. Meth. Phys. Res., B7/8 (1985), 755.
[10] KRAJNOVICH D.J., VASQUEZ J.E., J. Appl. Phys., 73 (1993), 3001.

Received 6 April 2004
Revised 4 May 2004

Materials Science-Poland, Vol. 22, No. 2, 2004

A shock-wave model of the effect of superdeep penetration of powder particles into metallic materials*

A. E. KHEIFETS**, V. I. ZEL'DOVICH, N. YU. FROLOVA, I. V. KHOMSKAYA

Institute of Metal Physics, Ural Division, Russian Academy of Sciences, Ekaterinburg, 620219, Russia

A shock-wave model of the effect of superdeep penetration of explosion accelerated powder particles into metallic materials has been created. A criterion for the phenomenon proceeding by explosive loading of a target by a flow of particles is obtained. It is established that a flow action results in an homogeneous radial stretching of the target material. The stretching occurs by mobile cavities which carry particles into the target material.

Key words: *superdeep penetration; shock waves; explosive loading; powder particles*

1. Introduction

Under special conditions of loading, a small part of the torrent of explosion accelerated dispersed powder particles can penetrate into metal barriers. The depth of their penetration exceeds the size of the particles by 100–1000 times. The phenomenon is known as superdeep penetration (SDP). For "traditional" penetration, the relation of the depth to the diameter of the particles does not exceed 10. The conditions necessary for SDP are: particle speed greater than 300 m/s, particle size less than 500 μm, loading time over 100 ms, and an average torrent density of more than 10^3 kg/m^3 [1].

The equipment used in experiments with superdeep penetration is shown in Fig. 1. The charge of explosive substance 1 is detonated by means of the detonator 2. The powder 3 is located in a focusing lens 4. The discoverers of the phenomenon [1] empirically estimated an optimum form of the lens for achieving the superdeep penetration. The lens forms a homogenous flow of powder particles, flying at a speed of 500–1000 m/s. The diameter of the flow is approximately 50 mm. An aluminum plate 5 holds the powder

---

*The paper presented at the 5th High Pressure School on High Pressure Methods in Biotechnology and Materials Science, E-MRS Fall Meeting, Warsaw, 13–15 September, 2003.

**Corresponding author, e-mail: alex.home@r66.ru.

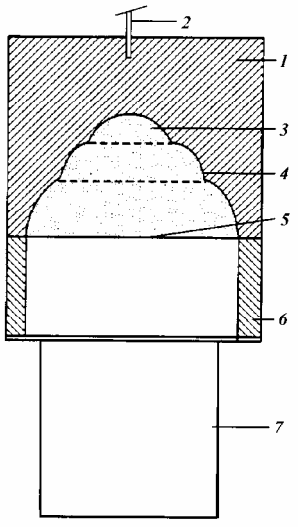

Fig. 1. Scheme of the experimental equipment

in the lens until the explosive charge detonates. The distance from plate 5 to the target 7 is adjusted by the height of the support 6. An all-metal sample or cartridge containing several samples usually forms the target. The majority of the particles do not penetrate the target – about 99% of the powder will stay on the surface and only 1% of particles will achieve the superdeep penetration. These particles can move in the target material. The length of the motion is tens of millimetres [1].

At present there is no theory of the physical nature of SDP. The purpose of this work was to construct a physical model of the phenomenon, to prove empirically the estimated conditions of superdeep penetration, and to answer the following questions:

1. Why does SDP occur only with a dense flow of particles? SDP never occurs for a lonely particle.

2. Why does not the superdeep penetration occur with large (more than 500 μm) particles?

3. How do low-strength particles penetrate into high-strength targets?

The existing models contain the assumption that the toughness of a particle exceeds the toughness of the target. According to these models, the particle can “resist” external influence, such as a cumulative jet [2].

2. Results

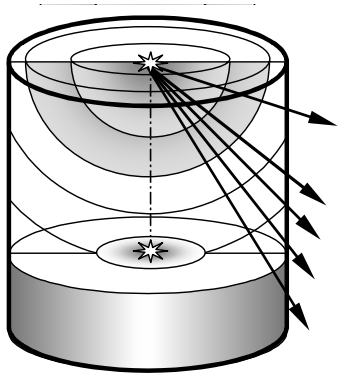

Fig. 2. “Spreading” of a cylindrical target

The model of the phenomenon put forward in this note is based on the shock-wave description of the interaction between a particle and a target material. When a particle strikes the surface of a cylindrical target (Fig. 2), an unconvergent shock wave appears in the target material. The wave carries the substance of the target. In the place where the particle hits the surface of the target, a crater is formed, its diameter being approximately equal to the diameter of the particle. The deformation of the target occurs, but the volume of the substance is constant. The target “spreads” as is shown in Fig. 2.

It is shown that the field of distortion of a substance in the target is a Coulombian field. The generalization from a single particle to a flow using the appropriate integrated equation allows the curve of the radial dependence of the deformation $\varepsilon^{(r)}$ of a cylindrical target (Fig. 3) to be drawn. Inside the area covered by the flow of particles

$$\varepsilon^{(r)} = \text{const}$$

outside this area

$$\varepsilon^{(r)} = -2\pi \frac{\sigma R_p^2}{r^2}$$

where R_p is the radius of the area covered by the flow, σ is the constant of the density distribution of particles.

In Figure 3, it is shown that the integrated field of a stress created in the target by a flow of particles results in a radial deformation of the material. In the area covered by the flow ($r < R_p$), this deformation is caused by homogeneous radial stretching. Outside the flow there is a radial compression. The compression is inversely proportional to the distance squared (Fig. 2). The extent of deformation is determined only by the physical characteristics of the flow and target, and does not depend on the size of particles. The field of stress created by a flow of particles is inhomogeneous, because each strike of a separate particle on the surface of the target has a discrete influence resulting in fluctuations of the stress field. The characteristic time τ of this process (the time during which stress at any point in the target is nearly constant) is approximately 10^{-7} s for particles with the diameter d_0 = 100 μm. In such dynamically varied conditions, the deformation of the target is basically elastic. The relaxation of the stretching stresses occurs by means of fractures in the target material. Thus, the homogeneous radial stretching of the target in the field of a flow means that cavity formation decreases the average density of the material. The lifetime of a cavity $\tilde{\tau}$ is the interval between the moment of its opening and closing. This time is about 10^{-6} s. During loading, the stress situation in the depth of the target is the same as on the surface, but there is a time delay corresponding to the limitations of shock-wave velocity c (approximately equal the velocity of sound, because the shock wave is not powerful). Thus the point of closing follows the point of opening into the target.

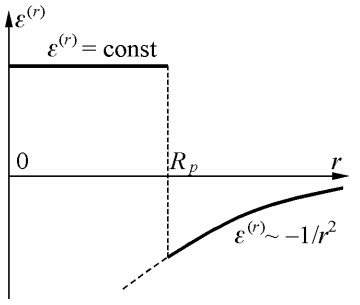

Fig. 3. Radial dependence of deformation. R_p is the boundary of the flow

The movement of a cavity is shown in Fig. 4. The plane (X, Y) in a Cartesian system of coordinates is connected with the surface of the target (Z = 0). Assuming that at the point (X_1, Y_1, 0) and at the moment $t = t_0$ the conditions were most favourable for the formation of a cavity, the situation will be repeated at the point (X_1, Y_1, Z) and time t_0+Z/c. Thus, the disclosing point of the channel will move along the Z axis with the

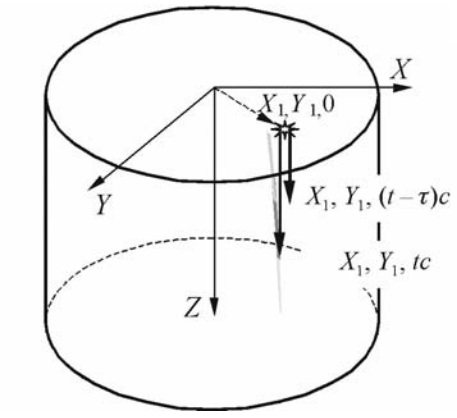

Fig. 4. Motion of a cavity ("transport capsule")

velocity of sound c. If at time $t = t_0 + \tilde{\tau}$ the conditions at the point (X_1, Y_1, 0) become unfavourable, the channel will close. The same situation will be observed at the point (X_1, Y_1, Z) and moment $t_0 + \tilde{\tau} + Z/c$. Hence, the point of closing follows the point of disclosing at a distance of $c\tilde{\tau}$ (the length of the cavity). The mobile cavities (transport capsules) carry particles inside the barrier. For $\tilde{\tau}$ of the order of 10^{-6} s, the length of a capsule is approximately 5 mm. If a particle is located in the capsule, it will be transported inside the target. Thus, the movement of a transport capsule can be accompanied by cumulative jets [2, 3] or high-speed fracturing of the material [4, 5]. The particle located in the capsule can be crushed [6]. Within the framework of the shock-wave performance, these effects are secondary, because the particle does not participate in the creation of its own capsule. The transported particle passively enters a capsule and does not spend energy on punching the material.

The diameter of capsules depends on the depth:

$$\delta(L)/\delta|_{L=0} = \sqrt{\frac{\Delta R(L)}{\Delta R\big|_{L=0}}} = \left(\frac{R^2}{R^2+L^2}\right)^{3/4} = \left(\frac{1}{1+\xi^2}\right)^{3/4}$$

where L is the depth, R is the radius of the target, $\xi = L/R$ is the relative depth.

The following criterion for SDP is obtained:

$$\frac{4\pi}{3}\sqrt[3]{\frac{1}{c}\frac{h}{\Delta t}} > 1$$

where h is the thickness of a layer of particles in the explosive accelerator (lens 4 in Fig. 1), Δt is the duration of loading, c is the velocity of sound. In the real experiment, h and Δt are not independent. An increase in h results in an increase in the flow length of particles, therefore Δt will also increase. Actually, the value of $h/\Delta t$ characterizes the density of the flow of particles.

3. Conclusions

• According to the established criterion for SDP, the penetration of particles into metallic materials can occur under the condition that $h/\Delta t > 5\times10^{-2}$, which corre-

sponds to the particle flow density of $\rho \geq 1$ g/(s·m^3). The penetration of particles at a flow density less than 1 g/(s·m^3) is impossible.

- The characteristic time of fluctuations τ is proportional to the size of particles d_0. If the diameter of a particle is larger than 500 μm, the value of τ will be of the order of 10^{-6}. This value exceeds the time of plastic relaxation for the majority of metals. In this case, the target is deformed plastically and transport capsules do not arise.
- Within the framework of the model offered, the toughness of particles does not play a significant role, because transport capsules can even carry liquids inside the target.

Acknowledgement

The work was supported by RFBR (Grants Nos. 03-03-33028 and SS-778.2003.3).

References

[1] USHERENKO S.M., *Superdeep penetration of particles into targets and creation of composite materials*, Minsk, NII IPs OP, 1998.
[2] ALTSHULER L.V., ANDILEVKO S.K., ROMANOV G.S., USHERENKO S.M., JETP Letters, 15 (1989), 55.
[3] MAKAROV P.V., *Chemical physics of processes of burning and explosion.* Proceedings of XI Symposium on Burning and Explosion, Chernogolovka, 1996, Vol.1, Part II, p. 331.
[4] CHERNYI G.G., Dokl. Ross. Akad. Nauk, 292 (1987), 1324.
[5] GRIGORYAN S.S., Dokl. Ross. Akad. Nauk., 292 (1987), 1319.
[6] ZEL'DOVICH V.I., KHOMSKAYA I.V., FROLOVA N.YU., KHEIFETS A.E., USHERENKO S.M., DYBOV O.A., Physics of Metals and Metallurgy, 93 (2002), 86.

Received 18 February 2004
Revised 15 May 2004

Materials Science-Poland, Vol. 22, No. 2, 2004

Propagation and interaction of dodecahedral converging shock waves in steel balls*

A. E. KHEIFETS[1**], V. I. ZEL'DOVICH[1], I. V. KHOMSKAYA[1], N. YU. FROLOVA[1], B. V. LITVINOV[2], N. P. PURYGIN[2], V. I. BUZANOV[2]

[1]Institute of Metal Physics, Ural Division, Russian Academy of Sciences, 620219 Ekaterinburg, Russia

[2]Russian Federal Nuclear Centre, 454070 Snezhinsk, Russia

Physical metallurgical and computer simulation methods were used to study the propagation and interaction of shock waves in steel balls subjected to convergent dodecahedrally symmetric shock waves. Conditions for energy cumulation and the realization of regular and irregular types of shock wave interactions were studied. Based on microstructural investigations of intact samples, the parameters of the shock-wave loading, namely pressure, residual temperature, and the density of the material were calculated.

Key words: *shock waves; microstructure; explosive loading; cumulating*

1. Introduction

As is known, the application of high dynamic pressures ensures that plastic deformation, fracture, polymorphic and phase transformations, chemical reactions and many other physical and chemical phenomena occur at extremely high rates. Therefore, the shock wave loading of condensed media permits fundamental properties of substances to be studied under extremal conditions.

The development of new technologies based on explosive methods permits one to increase the complexity of experiments conducted with the purpose of obtaining unusual dynamic loading conditions. The increasing complexity of experiments in turn imposes new requirements on the understanding of processes that occur upon the propagation of shock waves with a complex wave front configuration in the material. It is for this reason that studying effects of shock waves with a complex shock-wave-

---

*The paper presented at the 5th High Pressure School on High Pressure Methods in Biotechnology and Materials Science, E-MRS Fall Meeting, Warsaw, 13–15 September, 2003.

**Corresponding author, e-mail: alex.home@r66.ru.

front geometry on metallic materials is not only of pure scientific, but also of practical interest from the standpoint of several branches of science.

Under the action of a powerful pulse impact, structural changes can arise in a metal that prove to be unattainable under usual (static) conditions. On the other hand, an analysis of the results of shock-wave impacts on a sample permits one to draw conclusions about the character of shock-wave motion and about the processes of shock wave interaction and energy cumulation, i.e., to solve nonlinear problems of the physics of shock waves. With such an approach, the loaded sample is considered to be not only an object of investigation, but also a probe for obtaining information on complex shock-wave processes.

The properties of metals and alloys are closely related to their structure. It is therefore very important to establish a reliable correlation between microstructural changes and the parameters of shock-wave impact (pressure, degree of compression, residual temperature). In this work, we show how residual microstructural changes can help in answering some questions that arise when studying shock-wave motion in terms of hydrodynamics and gas dynamics.

2. Methods

Solid steel balls 60 or 40 mm in diameter were shock-loaded by exploding a spherical layer of explosive 10 or 20 mm thick (the ratio $R_{sp}/R_{\exp}$ of the ball radius to the outer radius of the explosive layer was 3/4 and 1/2, respectively). The explosion was initiated (with an asynchronism not exceeding 10^{-7} s) at the surface of the charge at twelve points uniformly located over the sphere surface. The explosive-covered sample was placed in a massive metallic casing, which ensured that the ball remained intact after it had been subjected to a convergent quasi-spherical shock wave. The pressure in such a wave grows from the sample surface toward the focusing centre as the amount of the substance encircled by the wave progressively decreases. The growth of pressure results in a temperature rise. The shape of the shock-wave front changes in the course of motion. At the centre of the ball, the shock wave is focused, after which a divergent compression shock wave propagates from the centre to the surface. The interaction of the wave with the rarefaction wave that propagates from the sample surface leads to the appearance of tensile stresses and related spalling phenomena in the material. Since the magnitude of tensile stresses is determined by the rate of unloading, the sample usually fails if unloading occurs too rapidly. Therefore, a massive metallic casing was used in order to retain the sample intact, which allowed a lower rate of unloading and decreased the tensile stresses occurring in the sample [1].

Shock-wave loading of a 40 mm steel ball. The formation of a quasi-spherical shock-wave front was studied using a ball made of steel containing 0.37 wt. % C and 1.1 wt. % Cr ($R_{sp}/R_{\exp}$ = 1/2). Various techniques of chemically etching diametrical cross sections reveal radial changes in microstructure near the centre of the sample,

indicating the effect of cumulation and show the "nonsphericity" of the loading method. The diametric cross section of a ball is shown in Fig. 1.

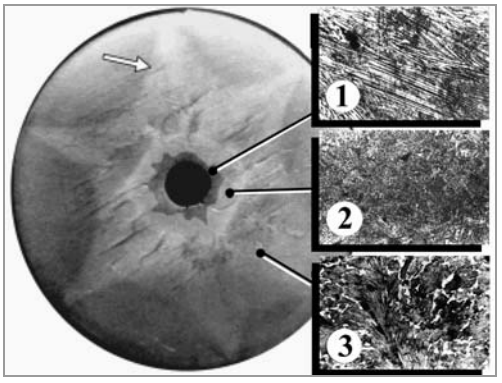

Fig. 1. Diametric section of a 40-mm ball:
1 – dendritic structure, 2 – bainite
3 – ferritic-pearlitic structure

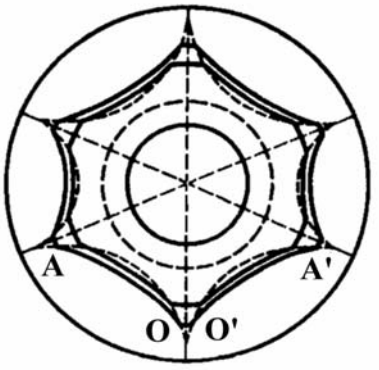

Fig. 2. Scheme of shock-wave propagation in a 40 mm ball

The patterns of various etchabilities were first observed by Al'tshuller et al. [2] on samples loaded with cylindrical shock waves from six and four points. Therefore, the patterns obtained by etching are called Al'tshuller patterns. Measurements of microhardness indicate that a significant reduction in strain hardening is observed in the light regions of Al'tshuller patterns [3]. All the experimental data obtained for this sample can be explained with the help of the sketch shown in Fig. 2 illustrating temporal changes in the initially three-dimensional front. The leading waves of three-wave Mach configurations (segment *OO'* in the scheme), which arise at the collision sites of divergent shock waves moving from neighbouring initiation points (lines *AO* and *A'O'*), have higher velocities, resulting in a smoothing of the front. According to [4], the traces of the points *O* and *O'* represent the boundaries of the contact discontinuity. In Fig. 1, these boundaries separate the Al'tshuller regions, which are light and dark on etching. The boundaries are indicated by arrows in Fig. 1. According to [4], the final magnitude of the pulse pressure is the same on both sides of a boundary of contact discontinuity (with allowance for an additional pressure on the substance due to the waves reflected from the surface of interaction, not shown in the scheme). However, the final state in dark Al'tshuller regions (Fig. 1) is a result of repeated (twofold) compression; i.e., the loading regime is in this case closer to static, which leads to a greater degree of strain hardening in the material.

The shock-wave motion acquires a quasi-spherical character beginning from a certain radius ($r \sim 9$ mm), and therefore can be considered to be one-dimensional. Figure 1 shows an almost spherical cavity of about 5mm in diameter in the centre of the quasi-dodecahedron. Around this cavity, there is a narrow (0.5–1.0 mm wide) region of columnar crystals that have a pronounced dendritic structure (Fig. 1). The presence

of this structure indicates that near the centre, where the focusing occurs, the steel melts (and it may, at the very centre, even evaporate) and then solidifies on cooling. Around the zone of columnar crystals there is a circular zone (about 2 mm thick), in which γ-iron is formed. Microstructural studies show that, in the outer portion of this zone, the formation of the γ phase occurs in place of the pearlitic one found in the initial microstructure of the steel. The inner portion of this zone is completely transformed into austenite. During cooling, after the explosive loading, the austenite transforms into an acicular structure (bainite) whose hardness is greater than that of pearlite and smaller than that of martensite. The outermost zone (about 14 mm thick) retains the initial ferritic-pearlitic structure, although a localized deformation was observed in some regions (Fig. 1).

As previously stated, near a certain critical radius $r \sim 9$ mm, a quasi-spherical convergent shock wave is formed as a result of the interaction of shock waves moving from different initiation points. According to [5], the pressure in a convergent spherical shock wave grows as $P \approx P_0(r_0/r)$. Based on this and on the fact that a clearly pronounced zone of melting exists in the sample (the distance from the centre of the sample to the outer boundary of the melting region is $r = 3.2$ mm), the pressure in the melting zone can be estimated considering the melting point of the steel and that solidification occurs after unloading. Results of such calculations are given in Table 1.

Table 1. Dependence of pressure P and residual temperature T on the distance to the ball centre r in the field of one-dimensional shock-wave motion

r, mm	P, GPa	T, K
9	52	520
8	60	590
7	68	680
6	81	830
5	102	910
4.5	115	990
4.0	134	1150
3.5	161	1450
3.0	224	2100

The residual temperature, pressure and specific volume were calculated in the three-dimensional (non-spherical motion) field of the ball by means of computer modelling of shock-wave motion on the basis of the form of the boundaries of contact discontinuity (indicated by arrows in Fig. 1). The results of these calculations for three-dimensional fields of the ball are given in Table 2.

Shock-wave loading of a 60-mm steel ball. Figures 3a, b display macro- and micrographs of the surface of a diametrical cross section of a 60-mm steel ball with $R_{sp}/R_{exp} = 3/4$. The changes observed in the microstructure (Fig. 3b) and the results of

microhardness measurements indicate that in matted Al'tshuller regions (which look brighter in Fig. 3a) cycles of $\alpha\rightarrow\varepsilon\rightarrow\alpha$ polymorphic transformations took place. Since the ε phase is formed in steel at pressures exceeding 13 GPa, the absence of traces of the $\alpha\rightarrow\varepsilon\rightarrow\alpha$ transformations in certain regions of the surface means that the pressure in these regions did not exceed this value.

Table 2. Dependence of pressure P, density ρ, and residual temperature T on the distance r to the ball centre in the field of three-dimensional shock-wave motion*

r, mm	P, GPa	ρ_1, g/cm^3	ρ_2,g/cm^3	T_1, K	T_2, K	ΔT, K
16.58	49.0	9.86	9.83	333	485	152
16.09	53.1	9.97	9.94	345	527	182
15.61	57.6	10.08	10.05	537	575	218
15.20	62.1	10.19	10.16	370	625	255
14.87	66.2	10.29	10.26	381	672	291
14.53	71.0	10.40	10.37	395	729	334
14.27	75.0	10.49	10.45	406	778	371
14.00	79.2	10.58	10.54	419	831	412
13.83	82.1	10.64	10.60	429	869	440

ρ_1 and T_1, ρ_2 and T_2 are densities and temperatures in dark (1) and light (2) A'tshuller's patterns. ΔT is temperature on the boundary.

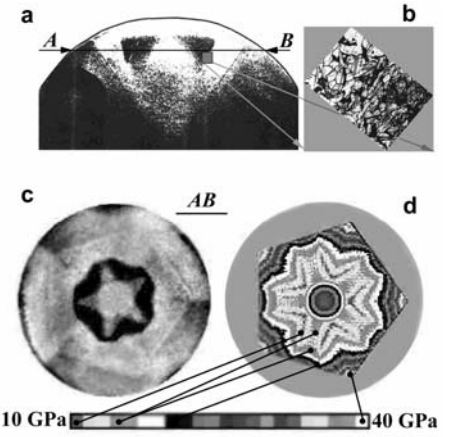

Fig.3. Shock-wave loading of a 60-mm steel ball: a) diametric section of the ball, b) traces of $\alpha\rightarrow\varepsilon\rightarrow\alpha$ transformations in light regions and absent of the traces in dark regions, c) macrostructure in the section *AB*, d) result of modelling (map of pressure)

The observed shock wave effects suggest that the interaction of shock waves moving from different explosion-initiation points obeys the laws of regular reflection. As a consequence, no energy cumulation or related significant increase in pressure occurs with the approach of the shock waves to the focusing centre. Three observations led to this conclusion.

1. No microstructural changes, such as traces of the $\alpha\rightarrow\gamma\rightarrow\alpha$ transformation cycles or melting, that could indicate a marked growth of pressure as shock waves approach the ball centre are seen.

2. The initial shock-wave loading symmetry is retained throughout the entire propagation of shock waves to the focusing centre (Fig. 3a). As stated above, the shock-wave motion acquires a spherical symmetry for irregular interactions, with the pressure growing according to the l/*r* law, where *r* is the distance to the ball centre.

3. No traces of contact discontinuities are present upon the motion of a three-wave Mach configuration.

A regular character of the interaction of shock waves leads to a situation where the nonsphericity of the shock-wave front is retained in the course of wave motion toward the focusing centre. This substantially complicates the theoretical description of shock-wave motion. The solution of the nonlinear problem of the propagation and interaction of shock waves in the general case with such complex initial and boundary conditions proved impossible. However, the allowance for specific features in the geometry of the experiment permitted us to numerically simulate shock-wave motion from the results of metallographic investigations. Te cross section *AB* (Figs. 3a, c) of the ball was used for modelling. A number of assumptions were made concerning the allowance for nonlinear effects. The agreement achieved between the experimental and theoretical results can be considered as an evidence of the validity of these assumptions. Figure 3d shows the results of the simulation, along with the experimental pattern of microstructural changes observed in the ball cross section given in Fig. 3c. A virtually complete agreement of the calculated results with experimental data is observed.

3. Conclusions

Two types of shock-wave motions in metallic balls upon quasi-spherical shock-wave loading were considered. In the first case, the initial conditions become "forgotten" at the stage of convergence, after which the motion acquires a spherical one-dimensional character. In the other case, the initial conditions are not "forgotten" during convergence. It has been established that for the first type of shock-wave motion there is a corresponding Mach (irregular) regime of interaction of shock waves. This occurred in the 40-mm steel balls. The experimental investigations allowed a scheme to be developed for the transformation of dodecahedral shock-wave front into a spherical one. Based on the experimental data, the thermodynamic parameters of shock-wave loading for a steel ball 40 mm in diameter ($R_{sp}/R_{exp} = 1/2$) were calculated in both the region of one-dimensional and three-dimensional shock-wave motion. When simulating the shock-wave motion, we used a real geometry of the boundaries of contact discontinuity. The second regime of the shock-wave motion is associated with a regular interaction of primary shock waves, as realized in the 60-mm steel balls ($R_{sp}/R_{exp} = 3/4$). A computer simulation of shock-wave motion based on the metallographic investigations of microstructural changes in the steel permitted us to reconstruct a picture of the shock-wave motion and to describe the spatial distribution of pressures in the ball.

Acknowledgement

This investigation was carried out within the Presidium of the RAS program *Thermal physics and mechanics of intensive energy influence* and was supported in part by the Russian Foundation for Basic Research, grant No. SS-778.2003.3 (Scientific School).

References

[1] BUZANOV V.I., PURYGIN N.P., Deformation of the metallic balls at quasispherical shock wave loading, [in:] *Detonatsiya* (Detonation), Proc. Symp. on Burning and Explosions, Chernogolovka, Moscow Ohlast (1992), p. 131.

[2] AL'TSHULLER L.V., TARASOV D.M., SPERANSKAYA M.P., Fiz. Met. Metalloved., 13 (1962), 738.

[3] KHEIFETS A.E., FROLOVA N.YU., ZEL'DOVICH V.I., LITVINOV B.V., PURYGIN N.P., RINKEVICH O.S., KHOMSKAYA I.V., Izv. Ross. Akad. Nauk. Ser. Fiz., 62 (1998),1303.

[4] COURANT R., FRIEDRICHS K.O., *Supersonic Flow and Shock Waves,* Interscience Publ., New York, 1948.

[5] ZABABAKHIN E.I., ZABABAKHIN I.E., *Yavlenie neogranichennoi kumulyatsii* (Phenomenon of Unrestricted Cumulation), Moscow, Nauka, 1988.

[6] KHEIFETS E., ZEL'DOVICH V.I., LITVINOV B.V., PURYGIN N.P., FROLOVA N.YU., KHOMSKAYA I.V., RINKEVICH O.S., BUZANOV V.I., Phys. Metals Metallography 90 (2000), S108.

Received 18 February 2004
Revised 15 May 2004

Materials Science-Poland, Vol. 22, No. 2, 2004

Transport phenomena in ammonium halides under high pressures*

G.V. TIKHOMIROVA**, A.N. BABUSHKIN

Physics Department, Ural State University, Lenin Avenue 51, Ekaterinburg, 620083, Russia

Polycrystalline ammonium chloride (NH_4Cl), fluoride (NH_4F) and bromide (NH_4Br) were studied at pressures from 20 to 50 GPa in the temperature range of 77–400 K. Phase transitions from a high-resistance to low-resistance state was found. The transition pressures were about 15 GPa for NH_4Br, 27 GPa for NH_4Cl, and 42 GPa for NH_4F. The transition temperatures and pressures were shown to depend on the preliminary pressure treatment. All ammonium halides show metal-like behaviour under high pressures, similar to that of alkali halides.

Key words: *ammonium halides; high pressure; resistivity*

1. Introduction

Alkali halides of cubic structure with mainly ionic bonds have been studied as model objects for high-pressure physics [1–3]. However, ammonium halides, with the ion $(NH_4)^+$ being an analogue of an alkali metal, have hardly been studied at high pressures at all. Their structures have been studied only up to 9 GPa [4, 5]. In this work, the conductivity of ammonium chloride (NH_4Cl), fluoride (NH_4F), and bromide (NH_4Br) under high uniaxial pressures from 15 to 50 GPa in the temperature range of 77–400 K was studied. Similar to microscopic structural analysis, i.e. X-ray or Raman-scattering measurements, transport measurements can be used to detect phase transitions. Recently, for NH_4Cl and NH_4F, we have found a transition from a high-resistance state to a low-resistance one under high pressures. In this paper, we present studies of this transition in these two ammonium halides and, additionally, in NH_4Br. The time dependence of the resistivity of the ammonium halides with changing pressure was also studied.

---

*The paper presented at the 5th High Pressure School on High Pressure Methods in Biotechnology and Materials Science, E-MRS Fall Meeting, Warsaw, 13–15 September, 2003.

**Correspomding author, e-mail: galina.tikhomirova@usu.ru.

2. Experimental

High pressures were generated in a high-pressure cell with synthetic carbonado-type diamond “rounded cone-plane” anvils [6]. These anvils are good conductors and can be used as electric contacts, making it possible to measure temperature and pressure dependencies of resistance. At the temperatures and pressures used, the contact resistance did not exceed several ohms. The behaviour of the samples was examined during several pressure cycles. The samples, produced by a high-pressure treatment from powder materials of chemical purity, were ~0.2 mm in diameter and 10–30 μm in thickness.

3. Results and discussion

A hysteresis in the pressure dependence of resistivity was observed for the ammonium halides studied (Figs. 1, 2). For all three materials, a sharp decrease in resistivity by orders of magnitude from more than 10^8 Ohm to kOhms was observed above some threshold value P_{c2}. On reducing pressure down to $P_{c1}<P_{c2}$, the materials returned to their high-resistive state. P_{c1} was about 42, 25–27 and 15–17 GPa for NH_4F, NH_4Cl

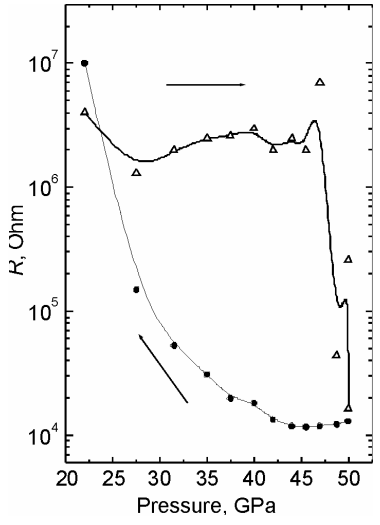

Fig. 1. Pressure dependencies of resistivity of NH_4Cl at room temperature

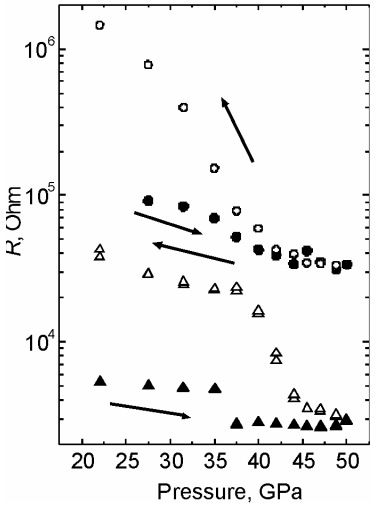

Fig. 2. Pressure dependencies of resistivity of NH_4Br at room temperature: circles – initial increasing and decreasing pressure, triangles – after long exposure under stress

and NH_4Br, respectively. A similar sharp transition was observed near P_c in the temperature dependence of resistivity (Figs. 3, 4). The values of P_c correspond to a stationary state, which was reached after sufficiently long exposure of the samples to stress. The time of pressure treatment necessary to stabilize P_c was quite different for the three materials. Initial loading of the samples with the pressure of 50 GPa caused a change in the resistance only after one-month exposure to stress for for NH_4F, and for about 10 days for NH_4Cl. NH_4Br samples did not require long pressure treatment; they became conductive at P_{c2} = 20–22 GPa. There is a correlation between the times of treatment, as well as the values of P_c, and the densities of the materials (the atomic weight of the halogens F, Cl and Br).

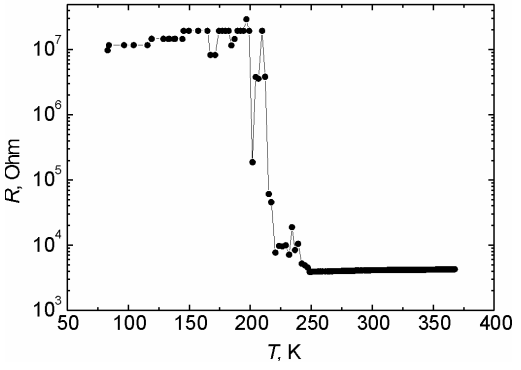

Fig. 3. Temperature dependence of resistivity of NH_4Cl at the pressure $P_{c1} \approx 27$ GPa

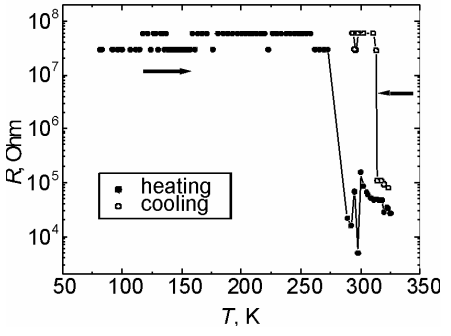

Fig. 4. Temperature dependence of resistivity of NH_4F at the pressure $P_{c2} \approx 50$ GPa

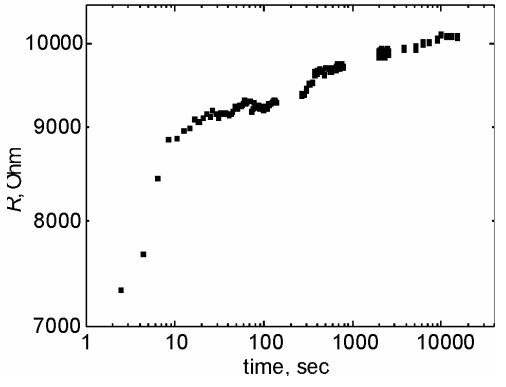

Fig. 5. Time dependence of the resistance of NH_4Br

Relaxation times of conductivity were found to be different for increasing or decreasing pressure (Fig. 5). The time dependencies of resistivity also demonstrated quite different relaxation times: one was seconds; another could be hours or days. The relaxation time was essentially larger at pressures near P_{c1}. At pressures far above P_{c1}, the relaxation times were several minutes. At pressures between P_{c1} and P_{c2}, a thermal hysteresis of the resistance of all three materials was observed, indicating the existence of intermediate states. The magnitude of hysteresis decreased after each cycle of

applied and removed pressure and/or after each time of exposure to a high pressure. All ammonium halides have shown a metal-like behaviour under high pressures similar to that of alkali halides. Details of the behaviour of the resistance for each of the ammonium halides are given below.

Ammonium fluoride. The main feature of the temperature dependencies of the conductivity of NH_4F under pressure was hysteresis; it is likely to be due to compacting the polycrystalline structure of the sample by a thermal expansion under high pressure. On heating, the conductivity had a metal-like character up to some critical temperature. The conductivity was practically temperature independent at higher temperatures. A long application of pressure, for several weeks, dramatically changed the character of the temperature dependence as it became metal-like. Below 42 GPa, a reversible transition from a low-resistive state (kOhms) to a high-resistive state (more than 100 MOhm) was observed independently of previous pressure treatment. (For more details, see [8].)

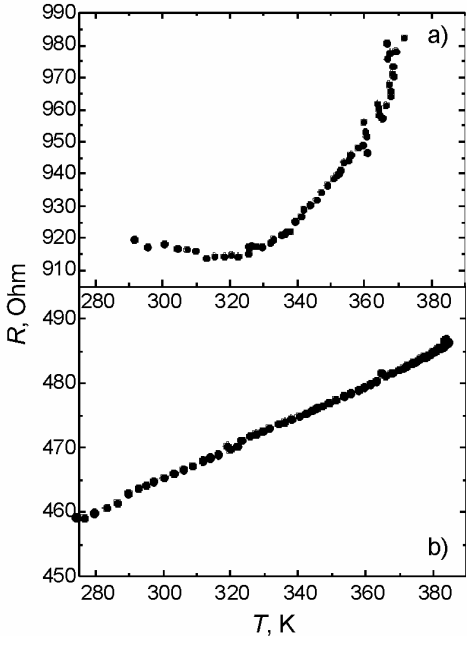

Fig. 6. Temperature dependencies of resistivity of NH_4Cl at 45 GPa: a) after two weeks, b) after two-month exposure under high pressure

Ammonium chloride. The pressure dependence of the resistivity of NH_4Cl was similar to that of NH_4F. However, the temperature dependencies were quite different. The conductivity of NH_4Cl at temperatures below 340 K had an activated character. At temperatures higher than the critical value, a transition to the metal-like state was observed. A minimum in the $R(T)$ dependence indicates the existence of a transition to an intermediate state. This transition did not disappear after long (up to six months) exposure to stress, but was observed in this case only at pressures below 35 GPa.

Figure 6 shows the temperature dependencies of the resistivity of NH_4Cl at 45 GPa after high-pressure treatment for 2 weeks (a) and for more than 2 months (b). Below 25–27 GPa, all ammonium chloride samples became high-resistive (MOhms).

Ammonium bromide. The temperature dependencies of the resistivity of NH_4Br had a positive slope in the temperature range 77 to 300 K. At pressures from 40 to 44 GPa and temperatures above 300 K, anomalies in the dependencies were found, indicating a transition to another state. The transition of ammonium bromide into a high-resistive state was observed at pressures below 15–20 GPa, depending on previous pressure treatment.

4. Conclusion

Phase transitions are shown to exist in ammonium halides at high pressures. They are revealed by sharp changes in resistance by several orders of magnitude. Above the transition, the resistivity is, as a rule, metal-like and similar to that of alkali halides. However, after a period of time, a non-monotonic dependence of resistivity on temperature was observed, indicating the existence of intermediate states. The data obtained show that transport measurements can be used to recognize phase transitions in ammonium halides. To determine the microscopic structure of the phases, X-ray or Raman-scattering measurements are needed.

Acknowledgements

The work was supported, in part, by CRDF grant No. EK-005-X1 for Ural Centre of Research and Education “Advanced materials”.

References

[1] VERESCHAGIN L.F., YAKOVLEV E.N., VINOGRADOV B.V., Pisma Zh. Eksp. Theor. Phys. (JETF Lett.), 20 (1975), 540.
[2] BABUSHKIN A.N., BABUSHKINA G.V., IGNATCHENKO O.A., J. High Pressure School, 1 (1999), 32.
[3] BABUSHKIN A.N., BABUSHKINA G.V., Fiz. Khim. Obrabotki Mat. (Phys. Chem. Mat. Treatment, in Russian, 3 (1996), 19.
[4] BALAGUROV A.M., SAVENKO B.N., KOZLENKO D.P., GLAZKOV V.P., SOMENKOV V.A., Fiz. Tv. Tela (Phys. Sol. State), 40 (1998), 143.
[5] BALAGUROV A.M., SAVENKO B.N., M.KOZLENKO D.P., GLAZKOV V.P., SOMENKOV V.A., HULL S., Physica B, 265 (1999), 92.
[6] VERESCHAGIN L.F., YAKOVLEV E.N., VINOGRADOV B.V., STEPANOV G.N., BIBAEV K.KH., ALAEVA T.J., SAKUN V.P., High Temp., High Pressures, 6 (1974), 99.
[7] BABUSHKIN A.N., PILIPENKO G.I., GAVRILOV F.F., J. Phys. Cond. Matter, 5 (1993), 8659.
[8] TIKHOMIROVA G.V., BABUSHKIN A.N., Defect Diff. Forum, 208–209 (2002), 271.

Received 18 February 2004
Revised 15 May 2004

Materials Science-Poland, Vol. 22, No. 2, 2004

Properties and applications of silica submicron powders with surface Ag nanoclusters

M. JASIORSKI[1*], S. BAKARDIJEVA[2], W. DOROSZKIEWICZ[3], S. BRZEZIŃSKI[4], G. MALINOWSKA[4], D. MARCINKOWSKA[4], M. ORNAT[4], W. STRĘK[5], K. MARUSZEWSKI[5, 6]

[1]Institute of Inorganic Chemistry and Metallurgy of Rare Elements, Wrocław University of Technology, ul. Smoluchowskiego 23, 50-372 Wrocław, Poland

[2]Institute of Inorganic Chemistry, Academy of Sciences of the Czech Republic, 25-068 Rez, Czech Republic

[3]Department of Microbiology, Institute of Genetic and Microbiology, University of Wrocław, ul. Przybyszewskiego 63/72, 51-148 Wrocław, Poland

[4]Institute of Textile Materials Engineering, Gdańska 118, 90-520 Łódź, Poland

[5]Institute for Low Temperature and Structure Research, Polish Academy of Sciences, ul. Okólna 2, P.O. Box 1410, 50-950 Wrocław 2, Poland

[6]Institute of Materials Sciences and Applied Mechanics, Wrocław University of Technology, ul. Smoluchowskiego 25, 50-370 Wrocław, Poland

Key words: *sol-gel method; Ag nanoparticles; submicron silica spheres; SERS; bacteriostatic properties*

Spherical silica powders with uniform, submicron grain diameter have been obtained using the sol -gel technology. Subsequently, metallic silver nanoparticles have been produced on the surfaces of the grains. Raman scattering spectra of such SiO_2–Ag^0 powders impregnated in ethanol solutions of tris(2,2' -bipyridyl)ruthenium(II) can be recorded for solutions four orders of magnitude more diluted than the lowest possible concentration detectable for complex liquid solutions in the same experimental conditions (the SERS effect). Also, such silver-doped silica powders display anti-microbial capabilities and can be used to obtain doped thin-film coatings, e.g. for the production of bacteriostatic textiles.

1. Introduction

Nanostructured materials possess unique mechanical, chemical and optical properties [1]. Nanometre-sized metal and semiconductor particles have attracted much attention due to their novel properties significantly different from those of correspond-

*Corresponding author, e-mail: marjas@immt.pwr.wroc.pl.

ing bulk materials, such as the quantum-size effect, nonlinear optical properties and unusual luminescence [2–4].

Sol-gel technology [5–7] provides an excellent way of obtaining transparent and mechanically stable glasses and glass-like materials (xerogels). The sol-gel technique is based on the hydrolysis of liquid precursors and formation of colloidal sols. The precursors are usually organosilicates (e.g. tetraethoxysilane, TEOS) yielding silicate sol-gel materials. In the case of the most often employed silicate sol-gel matrices, manufactured from hydrolyzates of various alkoxysilanes, the chemical reactions involved in gel formation are shown below.

The hydrolysis:

$$\equiv Si{-}OR + H_2O \xrightarrow{H^+/OH^-} \equiv Si{-}OH + ROH \tag{1}$$

and subsequent formation of the silicate network:

$$\equiv Si{-}OH + HO{-}Si\equiv \longrightarrow \equiv Si{-}O{-}Si\equiv + HOH \tag{2}$$

$$\equiv Si{-}OR + HO{-}Si\equiv \longrightarrow \equiv Si{-}O{-}Si\equiv + ROH \tag{3}$$

Another interesting property of sol-gel materials stems from the fact that they are prepared from liquid solutions, which allows doping by dissolving or suspending dopants in the hydrolyzates. An alternative way of introducing various substances to sol-gel matrices is via their impregnation in solutions/suspensions of the target molecules. Various oxide matrices obtained by the sol-gel method are essential for the development of a broad variety of advanced materials such as electrochemical solar cells, photocatalytic materials, electron-sensitive devices, optical coatings, etc. A very attractive and new development of the sol-gel technology is its application to manufacturing free and doped uniform silica spheres of submicron sizes [8–10]. Films of self-organized silica nanospheres deposited on a glass support exhibit the photonic crystal effect [10]. Such materials are potentially appliccable in a variety of fields such as medicine or optoelectronics. In the last decade, the synthesis and optical properties of photonic crystalline structures have been intensely investigated. Photonic crystals are characterized by frequency-forbidden band-gaps in a broad frequency region of electromagnetic radiation [5, 11–13]. The characteristic feature of such materials is their opalescence. It has been demonstrated [14–17] that photonic crystals offer a number of potential applications as filters, inhibitors of spontaneous emission, or thresholdless lasers.

Raman spectroscopy can be a powerful and flexible tool for detecting and characterizing organic and biological molecules. This method is, in general, quite sensitive and capable of detecting low quantities of analytes. However, in certain situations (especially in the case of biological and forensic studies) the need arises to detect molecules at concentrations below a typical limit of detection of conventional Raman techniques. It is well known that in certain cases the adsorption of organic molecules

on silver or gold electrodes results in a significant increase of the intensity of Raman scattering of adsorbed molecules. This phenomenon is known as Surface Enhanced Raman Scattering (SERS) [18]. Such enhancement has also been observed for molecules adsorbed on aqueous Ag sols [19], on silver nanoparticles embedded in a cellulose film [20], and on Ag evaporated onto SiO_2 nanoparticles [21]. The sol-gel method has been successfully used for obtaining sol-gel matrices doped with various nanoparticles of metals (e.g., Ag, Pt, etc.) and semiconductors (e.g., Ag_2S, CdS, etc.) [22–24]. Silica submicron spheres with surface-deposited metallic silver nanoclusters have been shown to exhibit the SERS effect for organic dye molecules adsorbed on the Ag islands [25]. This phenomenon can also be observed for submicromolar concentrations of organometallic complexes as presented in this contribution. Also, such Ag-doped powders possess bacteriostatic properties and can be used for doping various layered materials (e.g., textile impregnation thin films), giving them anti-microbial capabilities.

2. Experimental

Uniform, submicron-sized silica particles were synthesized following the base-catalyzed polycondensation of tetraethoxysilane (TEOS) in an alcoholic medium [5]. Briefly, ethanol (99.6%; POCh Gliwice) and a water solution of ammonia (POCh Gliwice) were mixed with the precursor (TEOS, 99%; Fluka). The solution was stirred in a plastic flask at room temperature for 2 h. During the stirring, the silica powder was formed and after filtering it was impregnated in an aqueous solution of $AgNO_{3(aq)}$. The impregnated silica powders were soaked in a series of solutions in order to reduce Ag^+ to Ag^0 ($NaOH_{(aq)}$, $formaldehyde_{(aq)}$, $NaBH_{4(aq)}$ [20]). Tris(2,2'-bipyridyl)ruthenium(II) ($Ru(bpy)_3^{2+}$) was obtained from Aldrich and used as received. For the SEM measurements, an XL 30 Philips CP microscope equipped with EDX, SE, BSE and Robinson detectors was used. Raman scattering spectra were obtained with a Raman Spectrometer Bruker RFS 100/S. In order to analyze the antibacterial effects of the SiO_2–Ag powders on bacteria, the *Escherichia coli* ATCC 25922 strain was used. To investigate the inhibition of bacteria growth, the standard agar diffusion method was used, according to the protocols of the National Committee for Clinical Laboratory Standards [26]. The overnight bacterial cultures, diluted 1000 times, were plated on Petri dishes containing Mueller–Hinton II Agar, (Becton, Dickinson Comp.). Next, 50 μl aliquots of water suspensions of the silver-doped powders were dropped on the surface of the medium and the plates were incubated at 37 °C for 24–48 h. After incubation, the diameter of the zones around the plated material (indicating inhibition of bacterial growth) were measured. The diameters of the zones are proportional to the amount of the anti-microbial agent, the way of its immobilization, the solubility of the agent, and the diffusion coefficient. As a control, water suspensions of pure (without silver) silica powders were dropped onto medium. The coated textile samples were prepared on PES/CO 67/33 fabric supports by doping a Dicrylan SL-MPU/SL-MPA polymeric paste with the SiO_2–Ag powders.

3. Results and discussion

Figure 1 presents a SEM micrograph of silica submicron spheres obtained by the sol–gel method. The diameter of the spheres is about 500 nm. As can be seen, the grains have a natural tendency to form very regular layers, which results in their photonic behaviour [10].

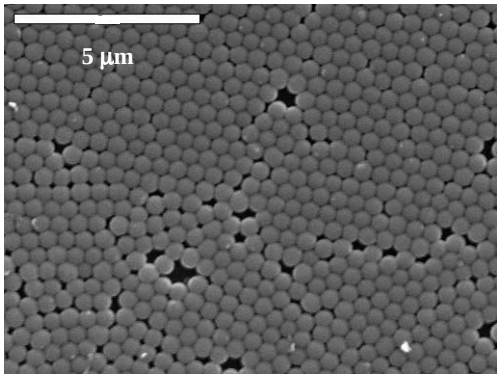

Fig. 1. Scanning electron micrograph of submicron sol-gel silica spheres

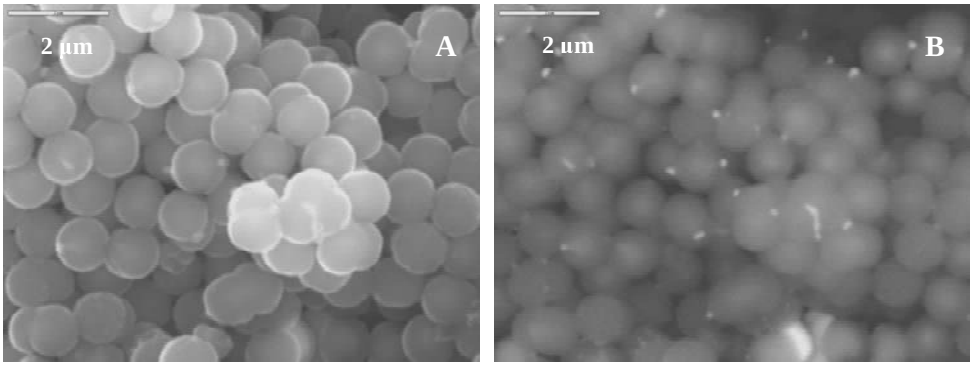

Fig. 2. SEM (A) and SEM-BEI (B) pictures of submicron silica spheres with silver “islands”

Silver nanoparticles obtained on the surfaces of silica submicron spheres are shown in Figure 2. Figure 2A presents a conventional SEM micrograph of silica spheres with Ag^0 clusters on their surfaces, while Figure 2B presents the BEI (Back-Scattered Electron Image) picture of the hybrid powder. Analogous nanoparticles have been obtained during the preparation of Ag/TiO_2 and Au/TiO_2 hybrid materials [27]. However, the sizes and shapes of those Ag^0 (Au^0)-doped TiO_2 nanoparticles are significantly different from those of the reported Ag^0-doped SiO_2 particles. The size of the silica spheres plays an important role in stabilizing the silver nanoparticles. Their interaction with silver ions or clusters inhibits aggregation of larger particles [28].

Silica powders with grains containing Ag^0 "islands" on their surfaces have been demonstrated to work as "amplifiers" of Raman scattering in the case of a simple organic dye [25]. In order to establish if the SERS effect also works for organometallic molecules possessing D_3 symmetry adsorbed on silver nanoclusters, the SiO_2–Ag^0 powders were soaked in $Ru(bpy)_3^{2+}$ ethanol solutions. Subsequently, the powders were filtered, washed, dried and their Raman spectra obtained.

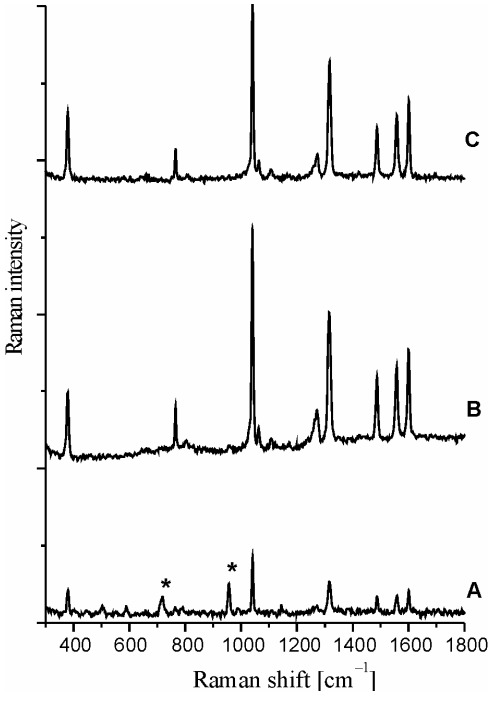

Fig. 3. FT-Raman spectra of the Ag^0-doped submicron silica powders after impregnation in solutions of tris(bipirydyne)ruthenium(II) with the complex concentrations of: 5.2×10^{-7} M (Trace A), 7.81×10^{-6} M (Trace B) and 7.81×10^{-5} M

Figure 3 presents the FT-Raman spectra of Ag^0-doped submicron silica powders after impregnation in solutions of tris(bipirydyne)ruthenium(II) with complex concentrations of: 5.2×10^{-7} M (Trace A), 7.81×10^{-6} M (Trace B) and 7.81×10^{-5} M. As can be seen, the $Ru(bpy)_3^{2+}$ Raman spectrum can easily be observed even for concentrations as low as ca. 5×10^{-7} M. Comparison with the results obtained for aqueous solutions of the ruthenium complex reveals that using the Ag^0-doped silica powders for SERS measurements allows the $Ru(bpy)_3^{2+}$ detection limit to be lowered by approximately four orders of magnitude (with the experimental setup used). It is important to note that in the case of silica powders without silver nanoclusters no Raman signal was observed upon their impregnation even in the concentrated $Ru(bpy)_3^{2+}$ solutions.

Thus, such materials could be used for improving analytical methods employed in, for example, medicine (detection of drugs or important metabolites), crime prevention (detection of chemical or biological weapons), environmental sciences (spills of dangerous substances), etc.

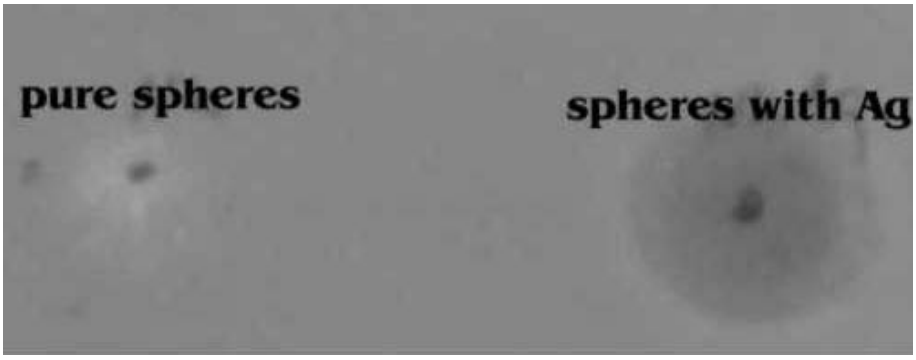

Fig. 4. A plate with E. Coli culture. Left – with pure silica particles, right – silica particles with Ag^0 nanoclusters

The obtained silica powders with silver intrusions display bacteriostatic properties. The inhibition of *E. coli* growth on an agar plate is shown in Figure 4. In this case, the lack of effect of pure silica spheres can be compared to the growth inhibition zone caused by the silica spheres doped with silver. An analogous effect has been observed for *Salmonella techimurium*, *Staphylococcus aureus* and *Hafnia alvei*.

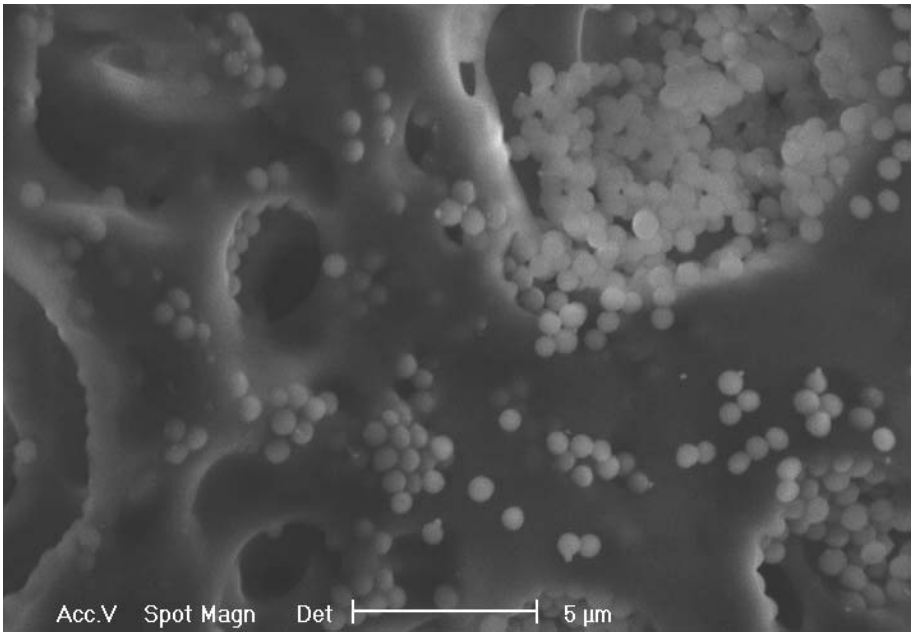

Fig. 5. SEM micrograph of a textile coating with SiO_2–Ag^0 powder

Such powders can be added to thermo-polymeric films used for the impregnation of textiles. Figure 5 presents a SEM micrograph of a doped textile coating surface. One of the practical problems to be overcome in the production of such doped coat-

ings is avoiding particle agglomeration. It is expected that textiles equipped with well-dispersed nanoclusters of metallic silver on their surfaces will become bacteriostatic. This could be employed for the production of, for example, medical fabrics.

4. Conclusions

A sol-gel based method for the preparation of submicron spherical silica particles doped with Ag^0 clusters is reported. Sphere morphology has been studied by the SEM method. It has been found that all silica particles have identical size (ca. 450 nm). SEM micrographs show that the silver clusters produced by chemical reduction occur on the surface of the silica spheres. Good quality FT-Raman spectra of $Ru(bpy)_3^{2+}$ molecules adsorbed on the doped powder grains have been obtained. Concentrations of the soaking solutions were a few orders of magnitude smaller than the concentrations of the reference solutions capable of yielding direct Raman spectra. The observed phenomenon can be explained by the enhancement of the Raman signal from molecules adsorbed on metallic Ag^0 particles (Surface Enhanced Raman Spectroscopy - SERS). Such materials offer a broad scope of potential applications in various fields of analytical chemistry. This effect could be employed in the detection of trace amounts of chemicals. Possible applications of such detection systems range from forensic investigations, through medicine, and to environmental issues. The SiO_2-Ag^0 powders also exhibit bacteriostatic properties. The powders can be used as additives to thin-film textile coatings, yielding textiles with anti-microbial capabilities. Such materials could be used e.g. for medical purposes.

References

[1] GLEITER H., Acta Mater., 48 (2000), 1.
[2] BARD A.J., Science, 207 (1980), 139.
[3] BARD A.J., J. Phys. Chem., 86 (1982), 172.
[4] JOSELEVICH E., WILLNER I., J. Phys. Chem., 98 (1994), 7628.
[5] BRINKER C.J., SCHERER G.W., *Sol-Gel Science*, Academic Press, San Diego, 1990.
[6] KLEIN L.C., Sol-Gel Optics, Kluwer Acad. Publishers, Boston, 1994.
[7] REISFELD R., JORGENSEN C.K., *Chemistry, Spectroscopy and Applications of Sol-Gel Glasses*, Springer-Verlag, Berlin, 1992.
[8] ROGACH O.E., KORNOWSKI A., GAPONENKO N.V., KAPITONOV A.M., GAPONENKO S.V., ROGACH A.L., EYCHMÜLLER A., [in:] *Physics, Chemistry and Application of Nanonstructures*, V.E. Borisenko, A.B. Filonov, S.V. Gaponenko, V.S. Gurin (Eds.), World Scientific, Singapore, 1999, p. 111.
[9] BLANCO A., CHOMSKI E., GRABTCHAK S., IBISATE M., JOHN S., LEONARD S.W., LOPEZ C., MESEGUER F., MIGUEZ H., MONDIA J.P., OZIN G.A., TOADER O., VAN DRIEL H.M., Nature, 405 (2000), 437.
[10] JASIORSKI M., HRENIAK D., MARUSZEWSKI K., STRĘK W., Mat. Sci., 20 (2002), 51.
[11] JABLONOVICH E., Phys. Rev., 58 (1987), 2059.
[12] McClelland D.C., Bachor H.-A., Wang J.C., J. Opt. Soc. Am. B, 10 (1993), 2.
[13] STOBER W., FINK A., BOHN E., J. Coll. Interface Sci., 26 (1968), 62.

[14] SALVAREZZA R.C., VAZQUEZ L., MIQUEZ H., MAYORAL R., LOPEZ C., MESEGUER F., Phys. Rev. Lett., 77 (1996), 4572.
[15] LOPEZ C., VAZQUEZ L., MESEGUER F., MAYORAL R., OCANA M., MIGUEZ H., Superlattices Microstructures, 22 (1997), 399.
[16] BOGOMOLOV V.N., KURDYUKOV D.A., PROKOFEV A.V., SAMOILOVICH S.M., Pisma Zh. Eksp. Teor. Fiz. (in Russian), 63 (1996), 496.
[17] BOGOMOLOV V.N., GAPONENKO S.V., GERMANENKO I.N., KAPTONOV A.M., PETROV A.P., GAPONENKO N.V., PROKOFIEV A.V., PONYAVINA A.N., SILVANOVICH N.I., SAMOILOVICH S.M., Phys. Rev. E, 55 (1997), 7619.
[18] CAMPION A., KAMBHAMPATI P., Chem. Soc. Rev., 27 (1998), 241.
[19] LI X.Y., PETROV V.I., CHEN D., YU N.T., J. Raman Spectr., 32 (2001), 503.
[20] KUROKAVA Y., IMAI Y., TAMAI Y., Analyst, 122 (1997), 941.
[21] LITORJA M., HAYNES C.L.. HAES A.J., JENSEN T.R., VAN DUYNE R.P., J. Phys. Chem. B, 105 (2001), 6907.
[22] STREK W., MARUSZEWSKI K., JASIORSKI M., LUKOWIAK E., BRYJA L., CIORGA M., SITAREK P., MISIEWICZ J., Optica Applicata, 29 (1999), 401.
[23] SAMUNEVA B., DIMITRIEV Y., DIMITROV V., KASCHIEVA E., ENCHEVA G., J. Sol-Gel Sci. Techn., 13 (1998), 969.
[24] ARMELAO L., COLOMBO P., FABRIZIO M., GROSS S., TONDELLO E., J. Mater. Chem., 9 (1999), 2893.
[25] MARUSZEWSKI K., JASIORSKI M., HRENIAK D., STRĘK W., HERMANOWICZ K., HEIMAN K., J. Sol-Gel Sci. Techn., 26 (2003), 83.
[26] National Committee for Clinical Laboratory Standards (2000),. Performance Standards for Antimicrobial Disc Susceptibility Tests; Approved Standard M-2A7. NCCLS, Villanova, PA.
[27] WANG C.Y., LIU C.Y., CHEN J., SHEN T., J. Colloid Interface Sci., 191 (1997), 464.
[28] HAH H.J., KOO S.M., LEE S.H., J. Sol-Gel Sci. Tech., 26 (2003), 467.

Received 20 April 2004
Revised 4 June 2004

Materials Science-Poland, Vol. 22, No. 2, 2004

Luminescence properties of Eu^{3+}-doped $Al_2(WO_4)_3$

L. MACALIK[1*], J. HANUZA[1, 2], K. HERMANOWICZ[1], P. GODLEWSKA[2], N. V. SIDOROV[3]

[1]Institute of Low Temperatures and Structure Research, Polish Academy of Sciences, Wrocław, Poland

[2]Department of Bioorganic Chemistry, Faculty of Engineering and Economics, University of Economics, Wrocław, Poland

[3]Institute of Chemistry, Kola Science Centre, Russian Academy of Sciences, Apatyty, Murmansk Region, Russia

Emission spectra of $Al_2(WO_4)_3$ doped with Eu^{3+} were recorded at room temperature (orthorhombic phase) and at 10 K (monoclinic phase). The luminescence excitation spectra and luminescence decay profiles were recorded for both structural modifications at RT and LN_2T, and the luminescence lifetimes of Eu^{3+} have been estimated. Two-site behaviour of the optically active ions in both phases has been revealed in the luminescence studies. However, the emission decay profiles give one lifetime of the $^5D_2$ level, equal to 1.8 ms and 848.4 μs at room temperature and liquid nitrogen temperature, respectively. The results obtained have been explained in terms of an unusual location of Eu^{3+} ions inside the crystal tunnels, parallel to the *c*-axis.

Key words: *aluminium tungstate; luminescence; excitation; optical properties*

1. Introduction

This paper reports on the luminescence properties of $Al_2(WO_4)_3$ tungstate doped with Eu^{3+} ions. $Al_2(WO_4)_3$ belongs to the $A_2(BO_4)_3$ group of compounds (A = Cr, Al, Sc, In; B = Mo, W), which have been extensively investigated due to their unusual chemical and physical properties. These compounds exhibit a ferroelastic phase transition, from an orthorhombic *Pnca* (D_{2h}^{14}) to a monoclinic $P2_1/a$ (C_{2h}^{5}) structure [1–3]. The orthorhombic phase exhibits a negative thermal expansion [2–6]. High trivalent ion conduction has been discovered in these crystals [7–10]. A pressure -induced amorphization has been recently described in scandium molybdate and tungstate at moderate pressures [10–12]. Finally, these crystals can serve as crystal hosts for transition metal or lanthanide ion doping. For the above reasons, the tungstates

*Corresponding author, e-mail: lmacalik@int.pan.wroc.pl.

and molybdates of this family have been applied in fuel cell electrolytes [13], gas sensors [13], laser materials [14], optoelectronics [6], and as catalysts support [6].

The effect of pressure on the resistivity and compressibility of $Al_2(WO_4)_3$ has been investigated [15]. It was shown that the resistance of the crystal is strongly frequency -dependent and an anomalous change appears at about 5 kbar. Both the resistance and compressibility prove the occurrence of a reversible phase transition at this pressure.

High-pressure Raman studies of the $Al_2(WO_4)_3$ crystal have been performed by us, showing the onset of two reversible phase transitions at 0.35 and 2.9 GPa [16]. These transitions have been explained to be the result of a reorientation of the tungstate tetrahedra. The phase in the range 0.35–2.9 GPa is consistent with the low-temperature monoclinic phase $P2_1/a$.

In the present paper, we report the luminescence properties of Eu^{3+} ions in the $Al_2(WO_4)_3$ host. In the previous paper, we studied this crystal doped with Cr^{3+} ions [14]. It was stated that the activator substitutes the 8d position occupied by aluminium(III) ions. Since the ionic radii of Al^{3+} and Cr^{3+} ions in this coordination are equal to 0.535 and 0.615 Å, respectively, the mutual substitution of these ions was easily done [14]. In the present study, we have tried to introduce Eu^{3+} ions into the $Al_2(WO_4)_3$ crystal despite the fact that the ionic radius of such an ion is significantly larger (0.947 Å). It is expected that a positive result of this substitution will allow a new laser material containing lanthanide ions to be obtained.

2. Experimental

The synthesis of $Al_2(WO_4)_3$:Eu single crystals was carried out using the flux method described in [14, 16].

Emission experiments were performed using a dye laser with a 467 nm excitation wavelength. The emission was detected with a cooled R 5108 photomultiplier (λ = 400–1200 nm). A low temperature (10 K) was obtained by mounting the sample into a Leybold temperature-controlled closed-cycle cryostat.

Lifetime measurements were performed with an optical parametric oscillator as the excitation source. The 21 410 cm^{-1} line was chosen for the excitation. The emitted light was detected by a photomultiplier connected to a Tektronix TDS 3052 oscilloscope. Measurements were performed at 300 and 77 K.

We tried to measure electronic absorption spectra of the crystals at room temperature using a Cary 5 spectrometer. These spectra could not be recorded due to a small concentration of Eu^{3+} ions. For this reason, the excitation spectra were measured. They were recorded using a SSF 01 Spectrofluorimeter equipped with a 160 W Xe lamp with a sapphire window and an Al-coated parabolic reflector. For low-temperature measurements (7 K), a continuous flow helium cryostat (Oxford model) equipped with a temperature controller was used.

3. Results and discussion

Structural properties. The structure of $Al_2(WO_4)_3$ has been determined by us using low-temperature X-ray equipment [14]. In the 210–300 K temperature range this crystal is orthorhombic with the space group *Pbcn* (D_{2h}^{14}) and four formula units per unit cell. The lattice parameters at 293 K are: a = 12.571, b = 9.046 and c = 9.129 Å. Low-temperature X-ray studies revealed the presence of a first-order phase transition around 210 K. The phase stable below 210 K is monoclinic with the space group $P2_1$ ($P2_1/n$). Its lattice parameters at 160 K are: a = 8.962, b = 9.080, c = 12.587 Å and β = 90.06°. In the orthorhombic phase, the active ions are located in a slightly distorted octahedral arrangement of the oxygen atoms. The site symmetry of Al^{3+} ions is C_1, but its local symmetry can be regarded as close to the tetragonal C_{4v} because one Al–O distance significantly differs from the others. On the other hand, the monoclinic phase showed the presence of four different Cr^{3+} sites in the crystal [14]. The Eu^{3+} ions in the sample could replace the Al^{3+} ions, in a similar way as Cr^{3+} ions. However, another effect cannot be excluded. As the structure of the $Al_2(WO_4)_3$ host contains two tunnels of different sizes (Fig. 1) and the difference between the ionic radii of Eu^{3+} and Al^{3+} ions is very large, it is very likely that the active ions occupy these tunnels instead of the Al^{3+} sites. The tunnels are directed parallel to the c-axis of the orthorhombic phase and the b-axis of the monoclinic phase.

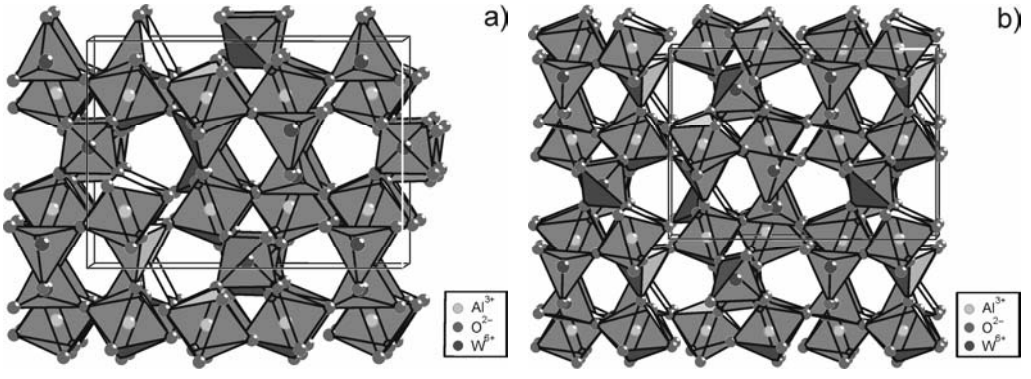

Fig. 1. Crystal structure of the $Al_2(WO_4)_3$ host in two phases: a) high-temperature (orthorhombic) phase and b) low-temperature (monoclinic) phase

Luminescence spectra. The luminescence spectra of the $Al_2(WO_4)_3$:Eu crystal recorded at 300 and 10 K are shown in Fig. 2. Table 1 lists the wavenumbers of the electronic transitions observed in the visible region. The presence of $^5D_0 \rightarrow {}^7F_{0\text{-}4}$ transitions and $^7F_{1,2}$ J-degeneracy prove that the site symmetry of Eu^{3+} ions both in the orthorhombic and monoclinic phases could be described by low-symmetry point groups: C_1, C_2, C_s or C_{2v} [17, 18]. The excitation spectra (Fig. 3) measured at 300 and 7 K confirm this conclusion. Because at room temperature the population of the $^7F_1$

level is about 27%, a transition from this level to $^5D_1$ is observed. The same situation is not observed at low temperature due to a dramatic decrease in the $^7F_1$ level population. From the luminescence and excitation spectra recorded at low temperatures, the Stark level components of electronic multiplets were calculated. Comparing the number of the theoretical and experimental multiplet components, we can say that the site symmetry of Eu^{3+} ions is low. The number of some components is higher than expected from the selection rules for monoclinic symmetry. We can, therefore, say that Eu^{3+} ions occupy two sites in two structural modifications of the crystal and their excitation and emission properties are the same (Table 2).

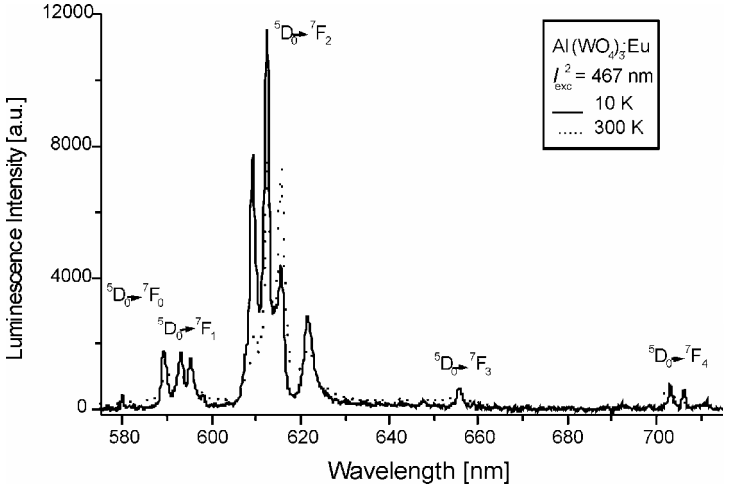

Fig. 2. Emission spectra obtained from the Eu^{3+} co-doped $Al_2(WO_4)_3$ crystal at 300 and 10 K. The excitation wavelength was 467 nm

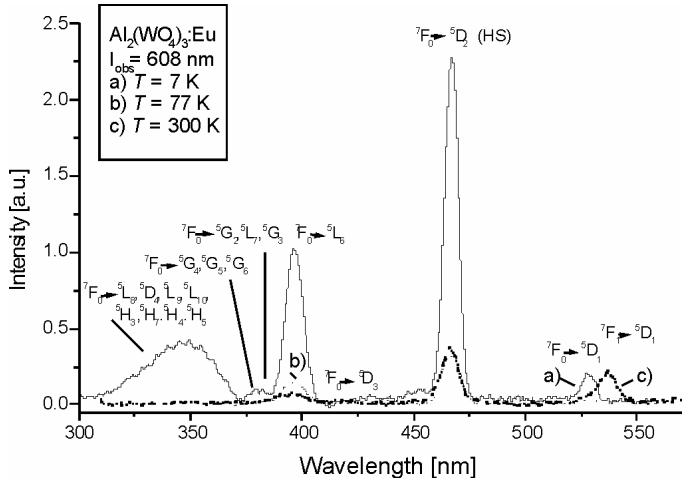

Fig. 3. Excitation spectra obtained for the $Al_2(WO_4)_3$:Eu crystal at 300, 77 and 7 K; λ_{obs} = 608 nm

Table 1. Energy of the Eu(III) emission bands measured for the $Al_2(WO_4)_3$:Eu crystal*

Transition	T = 10 K		T = 300 K	
	[cm^{-1}]	[nm]	[cm^{-1}]	[nm]
$^5D_0 \rightarrow {}^7F_0$	17 253	579.6 sh		
	17 241	580	17 244	579.9
$^5D_0 \rightarrow {}^7F_1$	16 969	589.3		
	16 883	592.3 sh	16 915	591.2 b
	16 861	593.1		
	16 812	594.8 sh	16 798	595.3
	16 798	595.3		
	16 711	598.4		
$^5D_0 \rightarrow {}^7F_2$	16 458	607.6 sh		
	16 415	609.2	16 404	609.6
	16 329	612.4	16 324	612.6
	16 281	614.2 sh		
	16 247	615.5	16 244	615.6
	16 088	621.6	16 090	621.5
$^5D_0 \rightarrow {}^7F_3$	15 439	647.7		
	15 284	654.3 sh	15 344	651.7
	15 253	655.6		
	15 211	657.4 sh	15 265	655.1
$^5D_0 \rightarrow {}^7F_4$	14 438	692.6	14 424	693.3
	14 316	698.5	14 316	698.5
	14 245	702 sh	14 243	702.1
	14 221	703.2	14 225	703
	14 203	704.1 sh	14 192	704.6 sh
	14 158	706.3	14 162	706.1
	14 063	711.1	14 069	710.8

*b – broad band, sh –shoulder.

The intensity of the $^5D_0 \rightarrow {}^7F_0$ band transition is very weak although it is clearly seen that its bandwidth is large (24.3 and 26.7 cm^{-1} at room and low temperature, respectively). This band could be deconvoluted into two components, which also suggests the existence of two sites occupied by Eu^{3+} ions.

Optical transitions typical of Eu^{3+} ions in a crystal correspond mainly to intra f^N transitions of predominantly electric dipole character. On the other hand, electric dipole transitions between states of the same configurations are strictly parity forbidden and the spectra observed result from mixing states of opposite parity during non-centrosymmetric interactions. The f-f transitions are allowed as the magnetic-dipole ones that obey the selection rule $\Delta J = 0, \pm 1$. The $^5D_0 \rightarrow {}^7F_2$ transition is electric dipole

in character, in contrast to the $^5D_0 \rightarrow {}^7F_1$ one, which is purely magnetic dipole allowed. Fluorescence spectra are known to be very sensitive to perturbations of the first coordination sphere. The ratio between the integrated intensities of the transitions: $I(^5D_0 \rightarrow {}^7F_2) : I(^5D_0 \rightarrow {}^7F_1) = I_{0\text{-}2} : I_{0\text{-}1}$ was related to the covalency of the Eu^{3+} ion surroundings via short-range effects [18–26]. Comparing our results, it is seen that the $I_{0\text{-}2} : I_{0\text{-}1}$ ratio is almost the same at both room and low temperature and equals 5.5, meaning that the covalent nature of the local Eu^{3+} ion sites is the same.

Table 2. Stark level components of electronic multiplets of Eu^{3+} ions in $Al_2(WO_4)_3$ crystal

(S, L, J) multiplet	Energy of Stark levels [cm^{-1}]	The number of Stark levels		ΔE [cm^{-1}]
		Theoretical	Experimental	
$^7F_0$	0, 12	1	2	12
$^7F_1$	272, 358, 380, 429, 443, 530	3	6	258
$^7F_2$	783, 826, 912, 960, 994, 1153	5	6	370
$^7F_3$	1802, 1957, 1988, 2030	7	4	228
$^7F_4$	2803, 2925, 2996, 3020, 3038, 3083, 3178	9	7	375
$^5D_1$	18818, 18889, 18954	3	3	136
$^5D_2$	21286, 21413, 21542	5	3	256
$^5D_3$	24378, 24462	7	2	84
$^5L_6$	24740, 25151, 25240, 25549, 25733	13	5	993

Lifetime measurements. Lifetime measurements of the $^1D_2$ level were carried out with a 467 nm excitation. The emission decay profiles measured at 300 and 77 K are

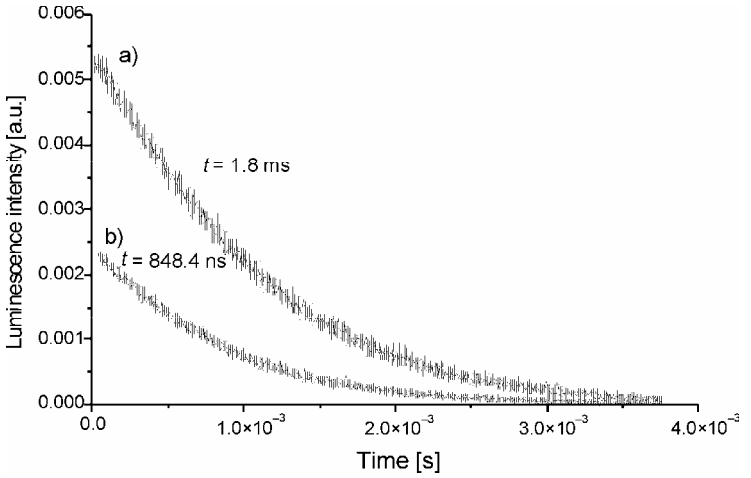

Fig. 4. Room-temperature (a) and liquid nitrogen-temperature (b) time dependence of Eu^{3+} emission obtained for the $Al_2(WO_4)_3$:Eu crystal. The excitation wavelength was 467 nm

shown in Fig. 4. We have found that the data can be well fitted by a single exponential profile both at high and low temperatures.

The lifetime of the $^5D_2$ level in the material studied is 1.8 ms at 300 K and 848.4 μs at 77 K. These results do not agree with X-ray data, which predict a one-site structure of the orthorhombic phase and a two-site behaviour of the monoclinic phase. The presence of only one component in the decay profile at 77 K suggests that the two different Eu^{3+} sites of the monoclinic phase have nearly the same lifetimes of $^5D_2$ luminescence.

4. Conclusions

Eu^{3+} ions do not replace the aluminium(III) sites in the $Al_2(WO_4)_3$ crystal, as observed for Cr^{3+} ions [14]. The concentration of the active ions in this sample is very low. The Eu^{3+} ions are located inside the tunnels that run parallel to the *c*-axis of orthorhombic phase and are also present in the monoclinic phase. Luminescence spectra indicate that Eu^{3+} ions occupy two sites, both in the orthorhombic and monoclinic phase. The coordination shells of the both sites have nearly the same degree of covalency and probably very close bond lengths. This is the reason for their optical similarity, i.e. very similar optical transition energies and excited state lifetimes. The present study therefore shows that the results obtained for the Eu^{3+} doped $Al_2(WO_4)_3$ crystal are different from those obtained for the Cr^{3+} doped sample. The main conclusion of the present study is that the crystal studied is a prospective host for transition metal ions [14], but cannot be applied for f-electron elements.

References

[1] SLEIGHT A.W., BRIXNER L.H., J. Solid State Chem., 7 (1973), 172.
[2] TYAGI A.K., ACHARY S.N., MATHEWS M.D., J. Alloys and Comp., 339 (2002), 207.
[3] EVANS J.S.O., MARY T.A., Int. J. Inorg. Mat., 2 (2000), 143.
[4] EVANS J.S.O, MARY T.A., SLEIGHT A.W., J. Sol. State Chem., 133 (1997), 580.
[5] EVANS J.S.O., MARY T.A., SLEIGHT A.W., Physica B, 241–243 (1998), 311.
[6] EVANS J.S.O., MARY T.A., SLEIGHT A.W., J. Sol. State Chem., 137 (1998), 148.
[7] IMANAKA N., TAMURA S., ADACHI G., KOWADA Y., Sol. State Ionics, 130 (2000), 179.
[8] IMANAKA N., TAMURA S., KOBAYASHI Y., OKAZAKI Y., HIRAIWA M., UEDA T., ADACHI G., J. Alloys and Comp., 303–304 (2000), 303.
[9] OKAZAKI Y., UEDA T., TAMURA S., IMANAKA N., ADACHI G., Sol. State Ionics, 136–137 (2000), 437.
[10] SECCO R.A., LIU H., IMANAKA N., ADACHI G., RUTTER M.D., J. Phys. Chem. Solids, 63 (2002), 425.
[11] SECCO R.A., LIU H., IMANAKA N., ADACHI G., J. Mat. Sci. Lett. 20 (2001), 1339.
[12] PARAGUASSU W., MĄCZKA M., SOUZA FILHO A.G., FREIRE P.T.C., MENDES FILHO J., MELO F.E.A., MACALIK L., GERWARD L., STAUN OLSEN J., WAŚKOWSKA A., HANUZA J., Phys. Rev. B, accepted for publication.
[13] LIU H., SECCO R.A., IMANAKA N., RUTTER M.D., ADACHI G., UCHIDA T., J. Phys. Chem. Solids, 64 (2003), 287.
[14] HANUZA J., MĄCZKA M., HERMANOWICZ K., ANDRUSZKIEWICZ M., PIETRASZKO A., STRĘK W., DEREŃ P., J. Sol. State Chem., 105 (1993), 49.
[15] MUKHERJEE G.D., ACHARY S.N., TYAGI A.K., VAIDYA S.N., J. Phys. Chem. Solids, 64 (2003), 611.

[16] MĄCZKA M., PARAGUASSU W., SOUZA FILHO A.G., FREIRE P.T.C., MENDES FILHO J., MELO F.E.A., HANUZA J., J. Solid State Chemistry, accepted for publication.
[17] NADERI M., ANDERSON M.W., Zeolites, 17 (1996), 437.
[18] CARLOS L.D., VIDEIRA A.L.L., Phys. Rev. B, 49 (1994), 11721 and references therein.
[19] REISFELD R., GREENBERG E., BROWN R.N., DREXHAGE M.G., JÖRGENSEN C.K., Chem. Phys. Lett., 95 (1983), 91.
[20] ZAHIR M., OLAZCUAGA R., PARENT C., LE FLEM G., HAGEN-MULLER P., J. Non-Cryst. Solids, 69 (1985), 221.
[21] REISFELD R., JÖRGENSEN C.K., *Lasers and Excited States of Rare-Earths*, Springer-Verlag, Berlin 1987 (Chapter 3).
[22] REISFELD R., JÖRGENSEN C.K., [in:] *Handbook on the Physics and Chemistry of Rare Earth*, K.A. Gschneider, L. Eyring (Eds.), North-Holland, Amsterdam 1987, Vol. 9, Chapter 58.
[23] OOMEN E.W.J.L., VAN DONGEN A.M.A., J. Non-Cryst. Solids, 111 (1989), 205.
[24] MALTA O.L., BRITO H.F., MENEZES J.F.S., GONCALVES E SILVA F.R., ALVES JR. S., FARIAS JR. F.S., ANDRADE A.V.M., J. Lumin., 75 (1997), 255.
[25] CARLOS L.D., SA FERREIRA R.A., DE ZEA BERMUDEZ V., MOLINA C., BUENO L.A., RIBEIRO S.J.L., Phys. Rev. B, 60 (1999), 1042.
[26] RAINHO J.P., CARLOS L.D., ROCHA J., J. Lumin., 87–89 (2000), 1083.

Received 20 April 2004
Revised 4 June 2004

Materials Science-Poland, Vol. 22, No. 2, 2004

Synthesis and characterization of metastable CeO_2–ZrO_2 solid solution obtained by polymerized complex method

WŁODZIMIERZ MIŚTA[1,*], TREVOR RAYMENT[2], JERZY HANUZA[1], LUCYNA MACALIK[1]

[1]Institute of Low Temperature and Structure Research,
Polish Academy of Sciences, P.O. Box 1410, 50-950 Wrocław 2, Poland

[2]Chemistry Department, Cambridge University, Cambridge CB2 1EW, UK

The paper describes the preparation and characterization of nano-size metastable tetragonal CeO_2 –ZrO_2 mixed oxides prepared by a polymerized complex method. A glycine–ethylene glycol solution containing Ce^{3+} and Zr^{4+} ions was polymerized at 80–110 °C to form a viscous transparent resin without any visible precipitation. After heat-treatment at relatively low temperature (ca 250 °C) on a hot plate in static air, the solid precursor ignited in part due to self-combustion, resulting in the formation of a nanocrystalline, compositionally-homogeneous solid solution. Its structure was confirmed using X-ray diffraction, HRTEM and Raman spectroscopy. The phase separation in CeO_2–ZrO_2 system on a subsequent heat-treatment in air and in a mixture of H_2 and He was also investigated up to 1100 °C.

Key words: *ceria–zirconia; polymerized complex method; Raman spectroscopy; X-ray diffraction*

1. Introduction

Cerium oxide, as a non-stoichiometric rare-earth oxide, has been extensively used in heterogeneous catalysis [1]. Ceria-based mixed oxides are active components of three-way automotive catalysts (TWC) [2–7]. One of the most important roles of CeO_2 in these systems is their ability to store and release oxygen which is related to their redox properties and thermal stability; oxygen storage capacity (OSC) of these materials increases significantly when Zr^{4+} is doped into CeO_2 lattice. A considerable decrease of bulk reduction temperature of mixed CeO_2–ZrO_2 solid solutions is caused by a strong modification of the oxygen sublattice which generates mobile oxygen atoms [8–10].

* Corresponing author, e-mail: mista@int.pan.wroc.pl.

The traditional method for the preparation of multicomponent materials involves preparation of mechanically mixed oxides powders which are subjected to high -temperature calcination for several hours to homogenize the ceria–zirconia composition via solid state reactions. However, this method gives materials with very low surface area and often yields compositional inhomogeneities. To overcome the need for high temperature homogenization in the preparation of $Ce_xZr_{1-x}O_2$ solid solutions, a novel method utilizing room-temperature high-energy mechanical alloying of pure CeO_2 and ZrO_2 has been developed [11, 12]. However, more homogenous compounds are generally prepared via co-precipitation techniques [13–17], hydrothermal synthesis [18–21], spray pyrolysis [22], physical gelation [23, 24], solution combustion [25, 26], sol-gel [27] and the microemulsion methods [28, 29].

The purpose of this study is to apply the polymerized complex method to the synthesis of nanocrystalline ceria–zirconia solid solutions. This technique is a modified version of the Pechini polymeric precursor method [30–33] and is based on the "in situ" polymerization of ethylene glycol in the presence of simple metal salts complexed by glycine. Such a preparation procedure enabled us to obtain homogenous transparent and very stable polymeric sols. It is very cheap and holds a number of advantages over the popular but rather expensive sol-gel synthesis via alkoxide route in which a dry nitrogen atmosphere must be used and the sols have a limited shelf-life. The sols produced via the polymer route may also be good candidates for the preparation of thin, dense ceria–zirconia films for thermal barrier coatings and in intermediate temperature solid oxide fuel cells (SOFC) [34, 35]. In the present study, we tried to check the homogeneity of the prepared solid solutions and to characterize the phase separation during heat treatment in air and in reducing environment by means of powder X-ray diffraction (XRD), HRTEM and Raman spectroscopy.

2. Experimental

Cerium nitrate hexahydrate $Ce(NO_3)_3 \cdot 6H_2O$ (99.99%, Aldrich) and zirconium oxychloride octahydrate $ZrOCl_2 \cdot 8H_2O$ (99.99%, Aldrich) were weighed to give 0.02 mole final oxide in the defined molar ratio, and mixed with 10 ml distilled water, 10 ml of concentrated nitric acid, 0.02 mole of glycine and 40 ml of ethylene glycol. The colourless clear solution thus obtained was heated on a hot plate at about 80–110 °C in order to expel water and other volatile compounds. As the solution became concentrated, it became viscous and changed colour from colourless to yellow or brown, indicating formation of a polymeric gel. The viscous polymeric product thus obtained was first carefully dried at 140 °C on a hot plate under infrared lamp giving an organic-inorganic solid precursor. After prolonged drying at higher temperatures, the dark brown solid ignited in part due to self-combustion during this process, resulting in formation of yellow powder. The samples were then heated in air in an electric furnace up to 1100 °C for 16 h.

Reduction treatments were performed at 1100 °C in 5% H_2/He flowing at 50 $cm^3 \cdot min^{-1}$ for 5 h in a ceramic tubular furnace. The heating rate was 10 deg/min. Research-grade purity gas mixtures (>99.996%) were employed without further purification. After reduction, partly dark blue samples were cooled down to the room temperature under hydrogen.

XRD patterns were obtained with a Philips PW1830 diffractometer ($Cu_{K\alpha}$ with a graphite monochromator situated behind the sample). X-ray powder diffraction patterns were refined and analyzed by the Rietveld method (DBWS 9807 [36] and PowderCell ver.2.3 [37] software) to determine the amount of different phases as well as their lattice parameters and crystallite size. *In-situ* high-temperature X-ray diffraction (HTXRD) work was carried out using an Anton Paar furnace with Pt/Rh heating strip.

Thermal decomposition of the precursors was studied by thermogravimetry (TG/DTA) using MOM-Budapest equipment. During the TG-DTA measurement, the samples were heated in air up to 1000 °C with heating rate of 10 °C/min.

The room temperature Raman spectra were measured with the Bruker RFS 100 FT-Raman Spectrometer using the back scattering arrangement. The resolution was 2 cm^{-1}. Excitation was performed by 1064 nm line of Nd:YAG laser.

HRTEM image was obtained with a Philips CM 20 microscope equipped with the SuperTwin objective lens and operated at 200 kV.

3. Results and discussion

3.1. Synthesis of CeO_2–ZrO_2 organic-inorganic precursor

The inorganic-organic sols obtained with the polymerized complex method give very stable, transparent, viscous solutions without any evidence of the precipitation. In an ethylene glycol medium, formation of ester bonds between carboxylate groups of glycinato-metal complexes and alcohol groups of ethylene glycol could be possible. Ester bonds would cross-link glycinato-metal complexes into low molecular weight oligomers and thereby prevent precipitation. Inorganic-organic hybrid polymers obtained in such a way consist of a dual polymer network, in which cluster or oligomer-type inorganic structures are linked by organic groups or polymer fragments of polyethylene glycol (PEG). This kind of immobilization of a metal complex into a macrofunctionalized organic ligand (PEG) is responsible for high stability of such systems.

3.2. Crystallization behaviour and thermal analysis

After drying on a hot plate at 140 °C the dark-brown solid inorganic-organic precursors were amorphous as could be seen in Fig. 1 where *in-situ* XRD patterns of the $Ce_{0.5}Zr_{0.5}O_2$ precursor during heat-treatment up to 500 °C with a heating rate of 10 °C/min are presented. Crystallization of the amorphous matrix starts at about 250 °C.

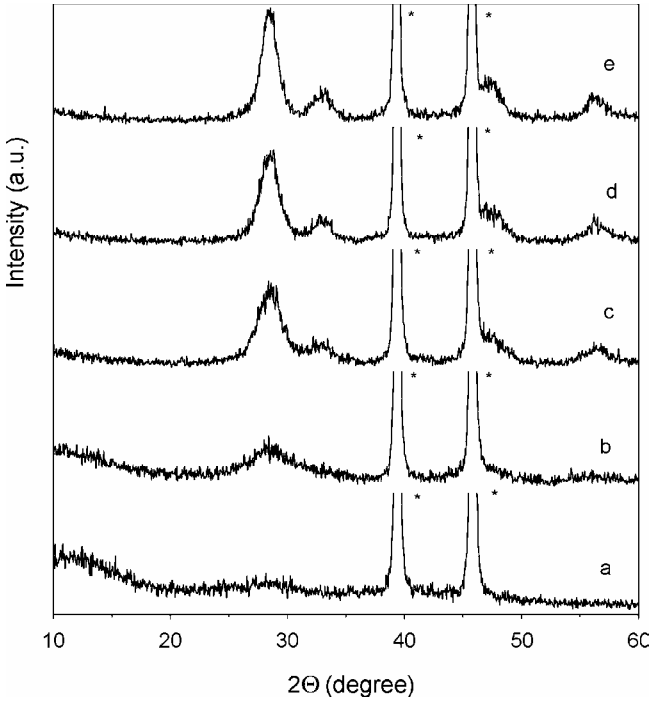

Fig. 1. *In-situ* X-ray diffraction patterns of $Ce_{0.5}Zr_{0.5}O_2$ precursor sample heated at: a) 200 °C, b) 250 °C, c) 300 °C, d) 400 °C, e) 500 °C. Asterisks indicate the Pt/Rh heating strip

Typically, we focused our attention on samples $Ce_{0.3}Zr_{0.7}O_2$ and $Ce_{0.5}Zr_{0.5}O_2$ in order to evaluate thermal evolution of the precursor samples. The differential thermal analyses (DTA) and thermal gravimetric analyses (TG) of gently dried $Ce_{0.3}Zr_{0.7}O_2$ and $Ce_{0.5}Zr_{0.5}O_2$ gels are shown in Figs. 2a, b, respectively. It has been observed that there are three major weight losses of 12.3, 24.7 and 26.0% for $Ce_{0.3}Zr_{0.7}O_2$ and 52.0, 27.0 and 6.0% for $Ce_{0.5}Zr_{0.5}O_2$ precursors. The first weight loss is probably mostly due to dehydration and evaporation of volatile organic components up to 220 °C. The second very rapid weight loss between 220 and 235 °C can be mainly ascribed to exothermic self-combustion reaction of suitable oxidizers (such as metal nitrates) and an organic fuel (such as glycine). The decomposition of glycine–metal nitrate complexes is highly exothermic [38] and the *in-situ* heat generated is utilized for the formation of complex oxides. Similar TG-DTA results were found by Patil et al. [26] during solution combustion (SC) synthesis of complex metal oxides using urea, glycine or hexamethylenetetramine as organic fuels and metal nitrates as oxidizers. The crystallization of amorphous CeO_2–ZrO_2 mixed solid solution starts at about 250 °C (Fig. 1b) which corresponds also to weak exothermic peak which is not well-defined on DTA curve (Fig. 2). The third weight loss extending up to ~500 °C may be due to burnout of most isolated carbon residue and after that there is no further weight loss above 500 °C up to 1000 °C. Products after calcining the gel at 600 °C were crystalline and

resulted in a pale yellow powder. The total weight losses of the polymeric precursors during heating up to 1000 °C were ca. 63% (Fig. 2a) and ca. 85% (Fig. 2b).

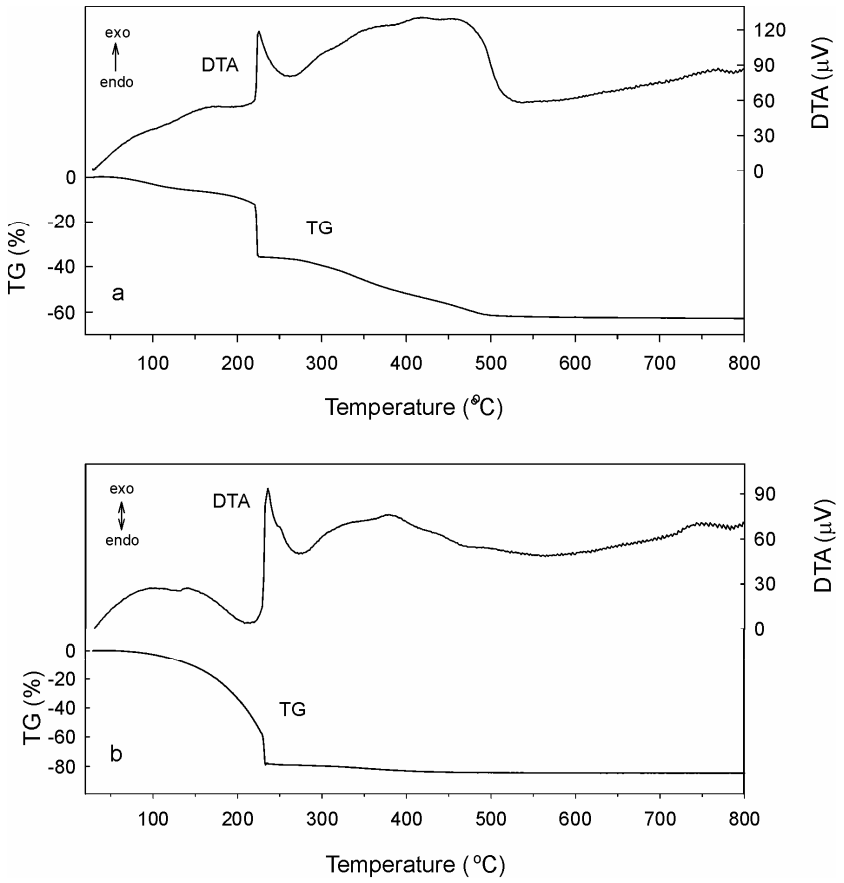

Fig. 2. Differential thermal analysis and thermogravimetric curve of polymeric precursors for samples of: a) $Ce_{0.3}Zr_{0.7}O_2$, b) $Ce_{0.5}Zr_{0.5}O_2$

The DTA curves for the same samples show broad endothermic peak at about 100–220 °C related probably to the dehydration and evaporation of high-melting polymeric compounds like poly(ethylene glycol) (PEG) and subsequently a narrow exothermic peak at 227 °C for $Ce_{0.3}Zr_{0.7}O_2$ or 232 °C for $Ce_{0.5}Zr_{0.5}O_2$ corresponding to the sudden weight loss observed on TG curve which can be attributed to the self-combustion process connected with exothermic redox reaction of suitable oxidizer (metal nitrate) and an organic fuel [26]. The other very broad exotherm at about 270–530 °C could be ascribed to the complete burnout of the residual organic char.

Thermolysis of organic-inorganic gel precursors is a very complex process resulting in complete breakdown of the gel structure before oxide formation. The cation homogeneity is controlled mainly by the thermal stabilities of the metal–glycinate

bridges in different glycinato-metal complexes which could decompose at different temperatures, resulting in phase separation during gel thermolysis [39]. In our case, the organic decomposition takes place simultaneously at a narrow temperature range during self-combustion process. During this process, a large amount of energy has been released resulting in an increase of local temperature. Therefore the Ce- and Zr-glycinate complexes crosslinked to the PEG oligomers undergo a rapid decomposition in the same temperature range. This highly exothermic process enables simultaneous nucleation and crystallization of a highly compositional homogeneous nanocrystalline mixed oxides as observed during the *in-situ* XRD experiment.

3.3. XRD, HRTEM and Raman characterization of the CeO_2–ZrO_2 solid solution

Figure 3 shows XRD patterns of the as-received nanocrystalline $Ce_xZr_{(1-x)}O_2$ samples heat-treated in air at 600 °C for 16 h. The lattice constants and crystallite sizes of each phase are presented in Table 1. The data were analysed using full pattern profile refinement.

For undoped nanocrystalline ZrO_2 sample (Fig. 3) there are two phases, monoclinic and small amount (~8 wt. %) of tetragonal phase. It is well known that undoped t-ZrO_2 could be stabilized by fine crystallites; the increase of their sizes with annealing treatment above 400 °C induces a martensitic t → m phase transition. A simultaneous presence of the tetragonal and monoclinic ZrO_2 was clearly detected with increasing crystallite sizes. Our results are in good agreement with those reported by Djurado et al. [40] who estimated the critical size to be around 23 nm. In our situation after heat-treatment at 600 °C for 16 h, the transformation is almost complete, the content of m-ZrO_2 phase being about 92 wt. % and crystallite size amounting to 27 nm.

Slightly asymmetric XRD profiles for nanocrystalline $Ce_xZr_{(1-x)}O_2$ (x = 0.1–0.2) samples suggest the formation of t-phase (Fig. 3). At 30–40 mol % of CeO_2 the samples mainly consist of t′-phase. The axial ratio c/a decreases with an increase of the content of CeO_2 and became unity at about 50 mol % of CeO_2. The composition $Ce_{0.5}Zr_{0.5}O_2$ represents a further point of interest since it is located at the limit of the t″ → t′ transition which allows one to prepare either tetragonal or cubic form by simply changing the preparation conditions [29, 41, 42]. A pseudocubic t″ phase mainly exists in the range of 50–80 mol % of CeO_2 content (Fig. 3, Table 1). The lattice parameters for cubic (t″, c) nanocrystalline $Ce_xZr_{(1-x)}O_2$ (x = 0.5–1.0) samples demonstrate rather good linear relationship between the cell parameters and the ZrO_2 content. However, the comparison between various literature data, in particular when different synthesis methods are employed, leads to a significant disagreement between the data [11, 41]. Since XRD patterns of nanocrystalline $Ce_xZr_{(1-x)}O_2$ solid solution are remarkably broad and sensitive mainly to the cation sublattice, it is very difficult to find the accurate phase composition.

The crystal structures and phase transformations in the CeO_2–ZrO_2 binary system have been investigated by many researchers [9, 43–48]. However, we are not aware of

any detailed and systematic study of the of nanostructured $Ce_xZr_{(1-x)}O_2$ materials prepared by the low-temperature method over the entire composition range. In the intermediate region, the exact nature of the phases is still unclear, because of stable and metastable phases of tetragonal symmetry present [41, 49]. Only arc-melted CeO_2 –ZrO_2 powders have been carefully studied by Yashima et al. [43–45, 50].

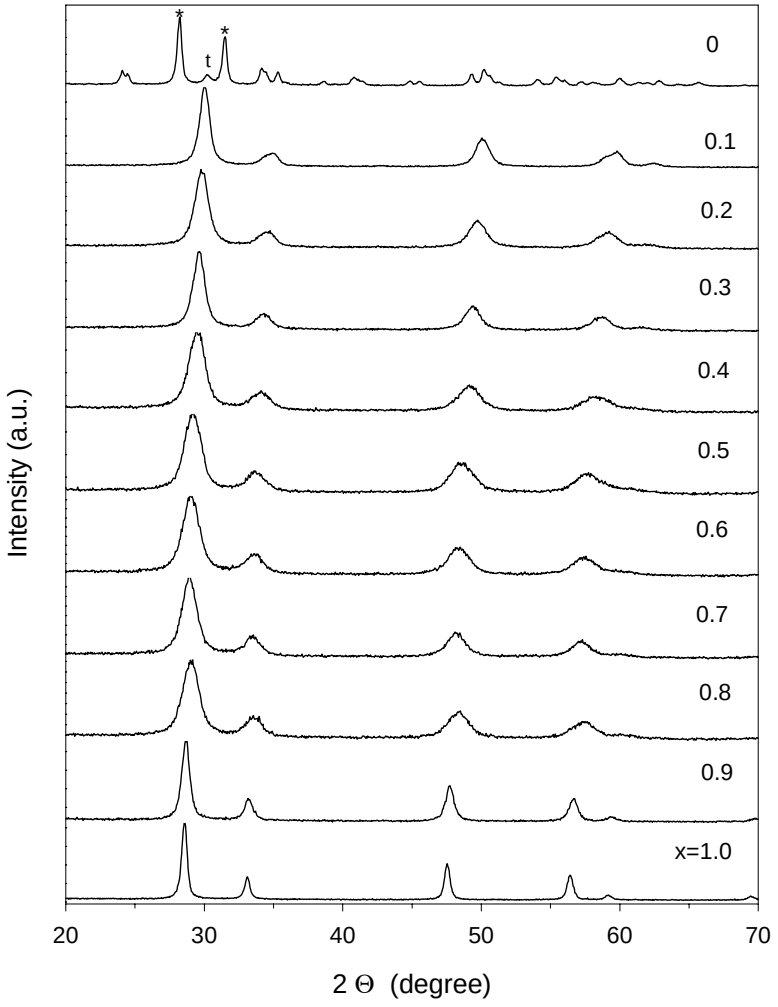

Fig. 3. X-ray diffraction patterns of $Ce_xZr_{(1-x)}O_2$ samples heated in air at 600 °C for 16 h. The symbols * and t indicate most intense lines of the monoclinic and tetragonal phases, respectively

One of the characteristic features of the zirconia–ceria solid solutions prepared by solid state reaction at high temperatures is the existence of monoclinic, cubic (fluorite type) and three tetragonal forms (t, t′, t″), all belonging to the $P4_2/nmc$ space group. At high cerium oxide concentrations, the cubic phase is formed, whereas for the zirconia-rich solid solution the monoclinic phase appears. A stable tetragonal form is

called the t-form, which is restricted to the solubility limit predicted by the equilibrium phase diagram. There is also a metastable t′-form with a wider solubility, but unstable with respect to the mixture of the t-form and the cubic phase. Finally, another metastable t″-form has an axial ratio *c*/*a* of unity, but with the oxygen atoms displaced along the c-axis from their ideal sites of the cubic phase (8*c* sites of the *Fm*3*m* space group). The t′/t″ and t″/c boundaries have been investigated by many authors [9, 10, 41, 43, 51] but the exact positions of metastable tetragonal regions strongly depend on the crystallite size and the synthetic method employed in preparation.

XRD patterns of the nanocrystalline $Ce_xZr_{(1-x)}O_2$ (x = 0.2–0.8) solid solutions calcined at 600 °C (Fig. 3) present very broad reflections. The average crystallite sizes of $Ce_xZr_{(1-x)}O_2$ (x = 0.2–0.8) samples give values of approx. 8–10 nm (Table 1). The addition of ZrO_2 in the form of solid solution resulted in effective improving the thermal stability of CeO_2 [41, 47, 48]. A pure ceria tends to sinter rapidly during heat-treatment at 600 °C yielding crystallite size about 23 nm (Table 1).

Table 1. XRD Characterization of $Ce_xZr_{1-x}O_2$ samples calcined at 600 °C for 16 h

CeO_2 [mol %]	Lattice type	Lattice parameters [Å]	D^c [nm]
0	monoclinic	a_m = 5.150 b_m = 5.207 c_m = 5.318 β = 99.22	27
	tetragonal	a = 5.086[a] c = 5.177	20
10	tetragonal	a = 5.122[a] c = 5.218	12.8
20	tetragonal	a = 5.158[a] c = 5.254	9.2
30	tetragonal	a = 5.197[a] c = 5.265	10
40	tetragonal	a = 5.230[a] c = 5.288	9.6
50	tetragonal[b]	A = 5.3016	9.6
60	tetragonal[b]	a =5.325	8.3
70	tetragonal[b]	a =5.345	8.4
80	tetragonal[b]	a = 5.360	8.5
90	cubic	a = 5.389	16
100	cubic	a =5.411	23

[a]The lattice parameters of pseudofluorite cell.

[b]Axial ratio c/a =1; from XRD pattern this phase is commonly indexed in the *Fm*3*m* space group.

[c]Crystallite size calculated from XRD.

Nanophase powders are a new class of materials which, in contrast to conventional solids, have an appreciable fraction of their atoms residing in defected environments,

especially on grain boundaries, where they occupy positions relaxed from their normal lattice sites [52]. Therefore the properties of nanophase materials are strongly related to their unique microstructures. This additional line broadening due to sample effects results from two main effects: the particle-size which results from the finite extent and particular morphology of the coherently diffracting domains within the grains, and the microstrain broadening or possibly defected structure. The precise determination of microstructural parameters requires taking into account strain and size effects in order to achieve the best interpretation of the observed peak-profile broadening.

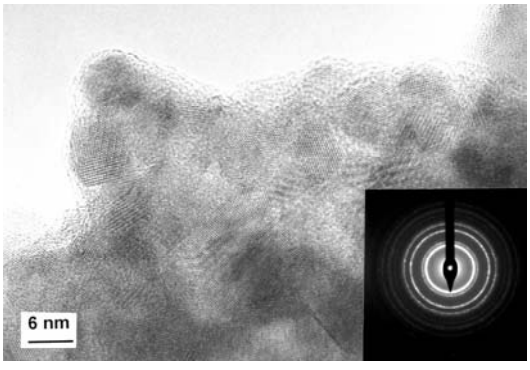

Fig. 4. HRTEM micrograph of the $Ce_{0.4}Zr_{0.6}O_2$ sample heated in air at 600 °C for 16 h and corresponding electron diffraction pattern (inset)

In order to observe a real microstructure of $Ce_xZr_{(1-x)}O_2$ samples heat-treated in air at 600 °C for 16 h we used TEM studies. HRTEM observations obtained for the 40 mol % CeO_2 sample (a representative image is given in Fig. 4) show the presence of nanocrystalline particles with lattice fringes corresponding to the (111) lattice plane in fluorite structure. These particles appear with narrowly distributed sizes, around 8–9 nm, thus corresponding roughly to the crystallite sizes detected in XRD. Specific preferential crystal orientations were not observed. The dried sample was composed of highly aggregated ultrafine particles.

A selected area electron diffraction pattern was also taken from this material (inset in Fig. 4). It shows the Debye–Sherrer rings (somewhat grainy, indicating incomplete sampling of all possible orientations) that can be consistently indexed according to a cubic fluorite structure with the lattice parameter of 5.25 Å. This value is in a relatively good agreement with XRD results. However, the positions of the rings agreed with those expected for the fluorite structure, although their line widths are too large to allow the presence of some tetragonal character to be excluded.

Vibrational spectroscopy is an effective tool for identification of the phase composition in the binary Ce–Zr–O system [10, 47, 48, 53–57]. Raman scattering measurements are more powerful than the XRD method for detection of a small amount of the stable tetragonal phase mixed with the cubic phase. Therefore Raman spectra can be used to characterize the CeO_2–ZrO_2 solid solution samples.

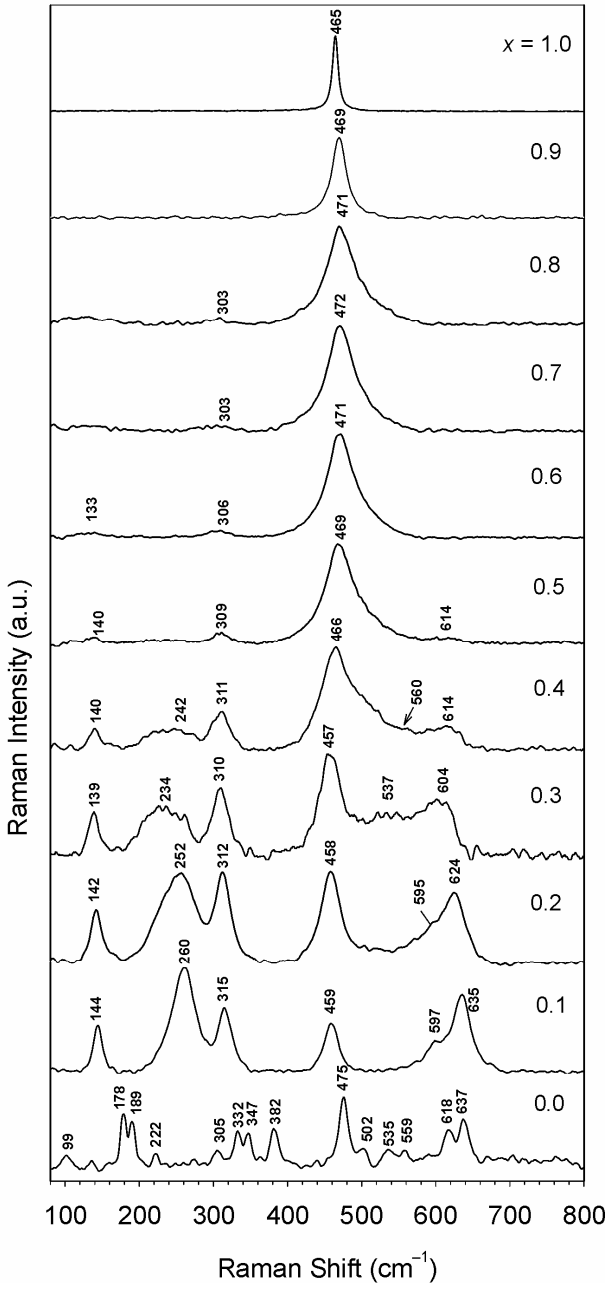

Fig. 5. Raman spectra of $Ce_xZr_{(1-x)}O_2$ samples after heat-treatment in air at 600 °C for 16 h

From the theoretical point of view the following vibrational characteristics are predicted for the respective phases of zirconia [58, 59]. For the cubic phase of the

fluorite structure (space group $Fm3m \equiv O_h^5$, $Z = 1$) the irreducible representation of the optic phonons is F_{2g} (R) + F_{1u} (IR).

For tetragonal t-ZrO_2 (space group $P4_2/nmc \equiv D_{4h}^{15}$, $Z = 2$) the distribution of the normal modes is: A_{1g} (R) + $2B_{1g}$ (R) + $3E_g$ (R) + A_{2u} (IR) + $2E_u$ (IR). In monoclinic phase (space group $P2_1/c \equiv C_{2h}^5$, $Z = 4$) all atoms lie on general positions and therefore the expected IR and Raman active modes are as follows: $9A_g$ (R) + $9B_g$ (R) + $8A_u$ (IR) + $7B_u$ (IR).

In XRD patterns, the peak broadening due to a small size of the crystallites makes detection of the tetragonal phase difficult, whereas the t phase exhibits six relatively strong, narrow bands in the Raman spectra as compared with one strong band for the cubic phase. However, for t″- or t′-phase only four or five modes could be visible at intermediate ceria contents (40–60 % mol). Besides strong bands at 465 cm^{-1} with a weak broad shoulder at about 550 cm^{-1} some very weak peaks at about 145 and 310 cm^{-1} are also observed [10, 42]. This high-frequency tail at 550 cm^{-1} has been attributed to oxygen vacancies [57]. Keeping in mind these theoretical predictions, the Raman spectra of the samples have been discussed.

Figure 5 shows the Raman spectra of $Ce_xZr_{(1-x)}O_2$ solid solution after calcination in air at 600 °C for 16 h. As expected, in pure CeO_2 only a strong F_{2g} mode is observed at 465 cm^{-1}. For $Ce_xZr_{(1-x)}O_2$ (x = 0.5–0.9) samples, the spectrum is dominated by a single strong band which shifts to higher frequencies (470 cm^{-1}). It has a very broad and asymmetric profile. Additionally, some peaks of low intensities at about 139 and 310 cm^{-1} are visible, indicating that t″-phase is also present. For $Ce_xZr_{(1-x)}O_2$ ($x < 0.4$) samples six bands of the tetragonal t-phase have been detected. For pure ZrO_2 the Raman spectrum shows a typical monoclinic phase without evidence of minor t-ZrO_2 phase.

Zhang et al. [60] reported recently that additional effects in Raman spectra should be expected for pure CeO_2 nanoparticles when the particle size is smaller than 20 nm. The peak at 464 cm^{-1} shifts to lower energies and shows large asymmetric broadening with decreasing particle size. The lattice expansion with decreasing particle size largely explains this systematic change of the Raman peak which can be attributed to the increasing concentration of point defects. The crystallite size effect (6–15 nm) on Raman spectra of undoped nanocrystalline tetragonal zirconia was presented by Djurado et al. [40]. Vibrational properties of nanomaterials are strongly dependent on the nano-grain size. In general, one can expect a broadening and frequency shifting of Raman bands as the nanograin size decreases.

3.4. Structural changes due to heat-treatment at 1100 °C in air and in reducing conditions

XRD patterns of $Ce_xZr_{(1-x)}O_2$ samples heated in air up to 1100 °C for 16 h are shown in Fig. 6. The $Ce_xZr_{1-x}O_2$ (x = 0.2–0.8) samples heated above 1000 °C show

considerable phase separation. According to the phase diagram in this system, there exists a wide two-phase (t + c) region. During annealing in air at 1100 °C for 16 h, the $Ce_xZr_{1-x}O_2$ (x = 0.2–0.8) solid solution separated into tetragonal phase with lower CeO_2 concentration (t-$Ce_{0.16}Zr_{0.84}O_2$; a = 5.1445 Å, c = 5.2394 Å) and the cubic phase with higher CeO_2 concentration (c-$Ce_{0.75}Zr_{0.25}O_2$; a = 5.347Å).

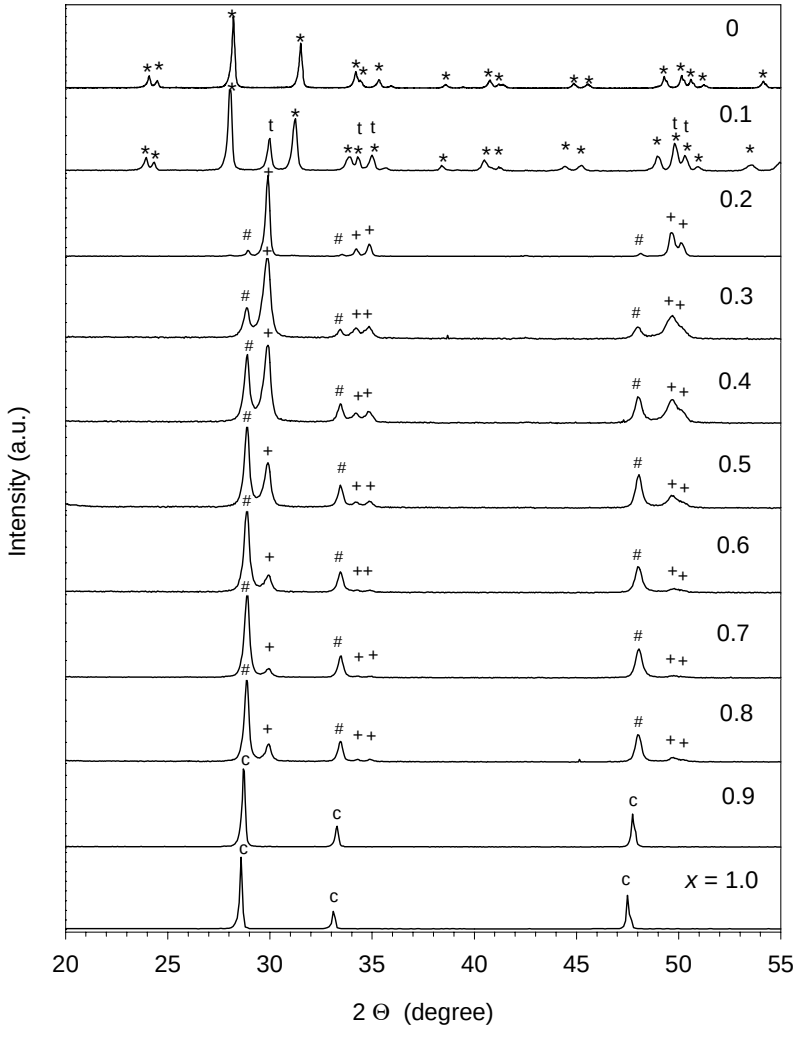

Fig. 6. X-ray diffraction patterns of $Ce_xZr_{(1-x)}O_2$ samples heated in air at 1100 °C for 16 h. The symbols (*) (t) (c) (#) and (+) indicate most intense lines of the monoclinic, tetragonal, cubic $Ce_xZr_{(1-x)}O_2$ phases and c-($Ce_{0.75}$ $Zr_{0.25}O_2$) , t-($Ce_{0.16}Zr_{0.84}O_2$) phases, respectively

The Raman spectra for $Ce_{0.3}Zr_{0.7}O_2$ and $Ce_{0.5}Zr_{0.5}O_2$ solid solution samples calcined at different temperatures (600 and 1100 °C) and in different atmospheres (air and 5% H_2/He) are presented in Figs. 7 and 8, respectively. The Raman spectra of

initial tetragonal t-$Ce_{0.3}Zr_{0.7}O_2$ and t″-$Ce_{0.5}Zr_{0.5}O_2$ homogeneous solid solution samples calcined at 600 °C for 16 h are presented in Fig. 7a and 8a, respectively. After calcination at 1100 °C in air both initial samples are composed of two phases (t-$Ce_{0.16}Zr_{0.84}O_2$ and c-$Ce_{0.75}Zr_{0.25}O_2$) with different relative concentrations. Their Raman spectra (Figs. 7b and 8b) consist of multiplets characteristic of the t- and c-phases. The existence of c-$Ce_{0.75}Zr_{0.25}O_2$

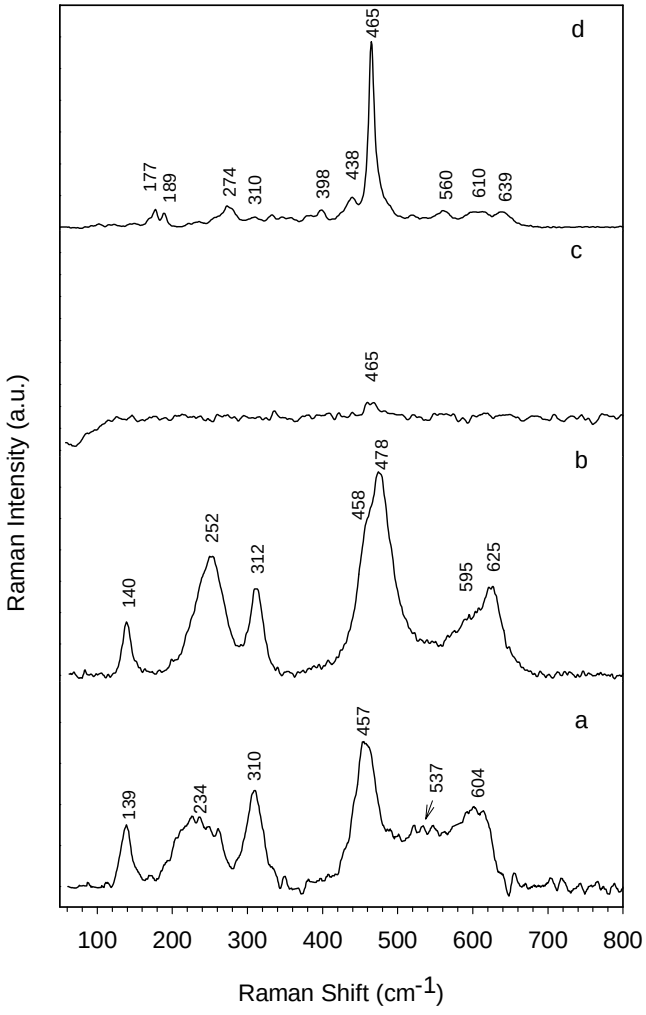

Fig. 7. Raman spectra of $Ce_{0.3}Zr_{0.7}O_2$ samples: a) heated in air at 600 °C for 16 h; b) heated in air at 1100 °C for 16 h; c) heated in 5% H_2/He gas mixture at 1100 °C for 10 h, d) heated in 5% H_2/He gas mixture at 1100 °C and subsequent calcination in air at 600 °C

phase is confirmed by the very strong line at 478 cm^{-1} and for t-$Ce_{0.16}Zr_{0.84}O_2$ phase Raman lines appears at about 625, 595, 458, 312, 252, 140 cm^{-1}. In pure CeO_2, the F_{2g} mode is observed at 465 cm^{-1} and for c-ZrO_2 the F_{2g} mode is centred at 490 cm^{-1} [47].

With decreasing CeO_2 content (down to about 60% mol) this single F_{2g} mode for cubic phase becomes broader and shifts to higher frequencies due to a decrease of the cubic lattice parameter [10]. The only difference between these Raman spectra (Figs. 7b and 8b) is a much higher intensity of the F_{2g} mode at 478 cm^{-1} for sample with the initial composition of $Ce_{0.5}Zr_{0.5}O_2$ (Fig. 8b), which is related to a higher content of the cubic (c-$Ce_{0.75}Zr_{0.25}O_2$) phase in the sample.

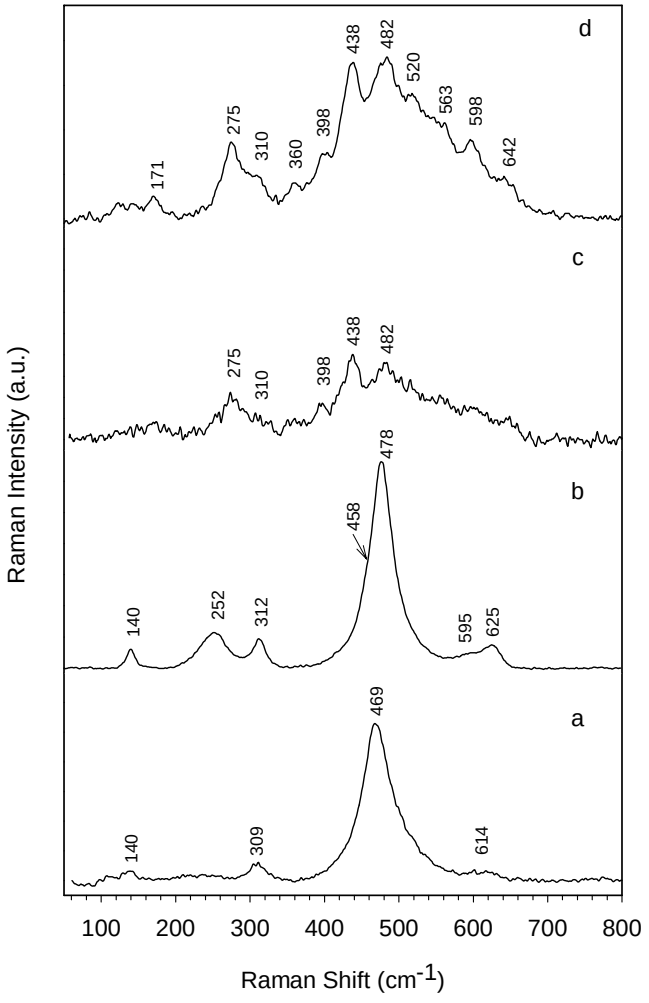

Fig. 8. Raman spectra of $Ce_{0.5}Zr_{0.5}O_2$ samples: a) heated in air at 600 °C for 16 h; b) heated in air at 1100 °C for 16 h; c) heated in 5% H_2/He gas mixture at 1100 °C for 10 h and d) heated in 5% H_2/He gas mixture at 1100 °C and subsequently calcinated in air at 600 °C

Raman scattering measurements also provided a supplementary evidence for the phase separation in samples reduced with hydrogen at 1100 °C. Figures 7c and 8c show Raman spectra for H_2 reduced initial $Ce_{0.3}Zr_{0.7}O_2$ and $Ce_{0.5}Zr_{0.5}O_2$ samples, re-

spectively. The Raman spectrum of reduced $Ce_{0.3}Zr_{0.7}O_2$ sample consists of only one very weak line observed at 465 cm^{-1}. Also, the spectrum of the reduced $Ce_{0.5}Zr_{0.5}O_2$ sample (Fig. 8c) is significantly more complex, consisting of very broad and weak lines of the disordered new phase (275, 310, 398, 438, 482 cm^{-1}). It is well known [61] that Raman spectra of disordered phases show less-resolved, broad lines resulting from the order defects (anion vacancies, antiphase boundaries, substituted cations). However, it could be possible to recognize defective cubic κ-Ce–Zr–O solid solutions which are formed after oxidation of the $Ce_2Zr_2O_{7+\delta}$ pyrochlore phase at ambient temperature. The Raman spectrum of non-defective cubic κ-phase, obtained by subsequent reoxidation at 600 °C in air of H_2 reduced $Ce_{0.5}Zr_{0.5}O_2$ sample at 1100 °C, is shown in Fig. 8d. These Raman bands are in a good accordance with the literature data [62, 63]. The Raman spectrum of non-defective $Ce_{0.3}Zr_{0.7}O_2$ sample prepared by hydrogen reduction and subsequent reoxidation at 600 °C is shown in Fig. 7d. After reoxidation the following phases are identified: cubic (465 cm^{-1}); κ-phase (274, 398, 438, 560, 610, 639 cm^{-1}) and monoclinic phase (177, 189 cm^{-1}).

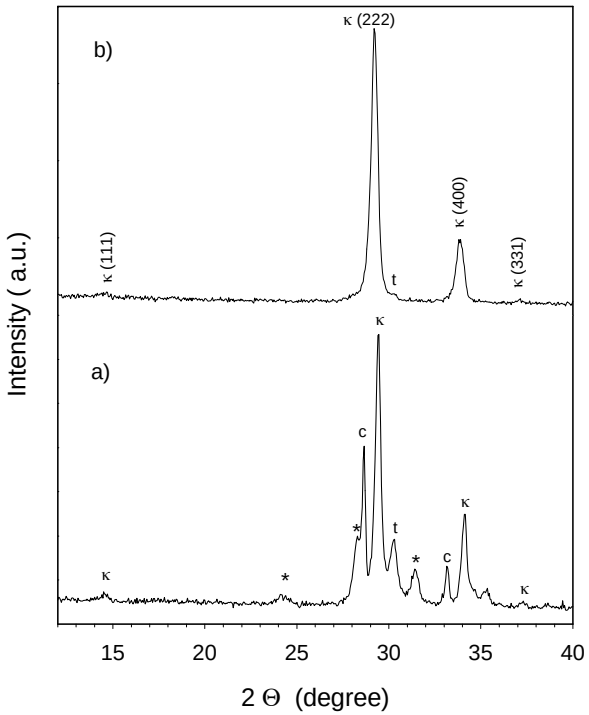

Fig. 9. X-ray diffraction patterns of $Ce_xZr_{(1-x)}O_2$ samples reduced in 5% H_2/He gas mixture at 1100 °C for 10 h: a) x = 0.3, b) x = 0.5. The symbols (*) (c) (t) and (κ) indicate most intense lines of the monoclinic, cubic, tetragonal and cubic κ-phase, respectively

The phase compositions of hydrogen reduced samples at 1100 °C were also investigated by XRD. The corresponding diffraction patterns are compared in Fig. 9. The

$Ce_xZr_{1-x}O_2$ ($x \approx 0.1$–0.3) samples consist of four phases. The exemplary XRD pattern for the reduced $Ce_{0.3}Zr_{0.7}O_2$ sample (Fig. 9a) exhibits very complex behaviour with extensive peak overlapping. After profile fitting of the XRD pattern, the major $Ce_xZr_{(1-x)}O_{2-\delta}$ phase could be indexed in the cubic pyrochlore cell with lattice parameter a = 10.520 Å. A low-intensity (odd, odd, odd) reflections confirm the cubic pyrochlore-type phase. The minor phases are low Ce-doped zirconia: t-ZrO_2 (a = 5.091 Å, c = 5.18 Å), m-ZrO_2 (a = 5.155 Å, b = 5.197 Å, c = 5.320 Å, β = 98.87°) and almost pure c-CeO_2 (a = 5.40 Å). However, these phases must have a very disordered oxygen sublattice as is evidenced from their Raman spectra (Fig. 7c).

The XRD patterns for the reduced $Ce_{0.5}Zr_{0.5}O_2$ sample after heat-treatment in hydrogen at 1100 °C are shown in Fig. 9b. It is interesting to note that no phase separation occurs during reductive heat treatment for this composition. The XRD pattern for this solid solution was indexed on the basis of a cubic pyrochlore-related structure with the lattice constant a = 10.584 Å. Only traces of tetragonal phase (2Θ =30.2°) could be noticed.

The phase separation in the Ce–Zr–O system induced by heat treatment in a reducing gas should be interpreted with regard to the ternary ZrO_2–CeO_2–$CeO_{1.5}$ phase diagram [64, 65].

The formation of a cubic κ-phase after a cycling of high-temperature reduction and subsequent oxidation is very effective to the enhancement of the oxygen storage capacity (OSC) and to decrease the reduction temperature in comparison with starting t′-tetragonal solid solution [63].

4. Conclusion

The polymerized complex method produces excellent precursors yielding nanocrystalline homogeneous ceria–zirconia solid solutions at low temperatures and for shorter annealing times, reducing segregation of the components. XRD, HRTEM, TG-DTA and Raman measurements have been successfully carried out on the polymeric derived CeO_2–ZrO_2 mixed oxides samples. The success in lowering the crystallization temperature of mixed oxides to about 250 °C may indicate an improved level of mixing of the cations in the prepared samples. The phase composition and the reduction properties of $Ce_xZr_{(1-x)}O_2$ solid solution depend on the choice of preparation method and specific processing conditions. To our best knowledge, no lower decomposition temperature was reached by the polymerized complex methods.

However, during a prolonged heat treatment in air or in a reducing gas at 1100 °C, phase segregation to more thermodynamically stable phases was observed. The $Ce_{0.5}Zr_{0.5}O_2$ solid solution shows lower thermal stability in air and slight phase segregation in hydrogen at 1100 °C in comparison to $Ce_{0.3}Zr_{0.7}O_2$ sample. Raman spectroscopy provided sufficient evidence for the phase separation even at the initial stage where XRD was not successful in showing the tetragonal components in the cubic

matrix. It is very important to investigate the thermal stability of the solid solutions prepared by the polymer route, particularly for use as advanced materials for the three-way catalyst (TWC-s) applications.

Acknowledgements

Financial support for this research programme from The Royal Society Postdoctoral Fellowship is greatly appreciated. The authors thank Dr. L. Kępiński and L. Krajczyk for performing HRTEM image and Z. Mazurkiewicz for skilful technical assistance.

References

[1] TROVARELLI A., Catal. Rev.-Science & Engineering, 38 (1996), 439.
[2] OZAWA M., J. Alloys Comp., 257–277 (1998), 886.
[3] FORNASIERO P., BALDUCCI G., KAŠPAR J., MERIANI S., DI MONTE R., GRAZIANI M., Catal. Today, 29 (1996), 47.
[4] DI MONTE R., KASPAR J., Topics Catal., 28 (2004), 47.
[5] SUGIURA M., Catal. Surveys Asia, 7 (2003), 77.
[6] BERNAL S., BLANCO G., CALVINO J.J., GATICA J.M., PEREZ-OMIL J.A., PINTADO J.M., Topics Catal., 28 (2004), 31.
[7] KASPAR J., FORNASIERO P., J. Solid State Chem., 171 (2003), 19.
[8] VLAIC G., DI MONTE R., FORNASIERO P., FONDA E., KASPAR J., GRAZIANI M., Studies Surface Sci. Catalysis, 116 (1998), 185.
[9] YASHIMA M., SASAKI S., YAMAGUCHI Y., KAKIHANA M., YOSHIMURA M., MORI T., Appl. Phys. Lett., **7**2 (1998), 182.
[10] VLAIC G., DI MONTE R., FORNASIERO P., FONDA E., KASPAR J., GRAZIANI M., J. Catal., 182 (1999), 378.
[11] LEITENBURG C., TROVARELLI A., ZAMAR F., MASCHIO S., DOLCETTI G., LLORCA J., J. Chem. Soc. Chem. Commun. (1995), 2181.
[12] SUDA A., KANDORI T., TERAO N., UKYO Y., SOBUKAWA H., SUGIURA M., J. Mater. Sci. Lett., 17 (1998), 89.
[13] LIN J.-D., DUH J.-G., J. Am. Ceram. Soc., 80 (1997), 92.
[14] HIRANO S., KAWABATA A., YOSHINAKA M., HIROTA K., YAMAGUCHI O., J. Am. Ceram. Soc., 78 (1995), 1414.
[15] SUN Y., SERMON P.A., J. Mater. Chem., 6 (1996), 1025.
[16] KAWABATA A., HIRANO S., YOSHINAKA M., HIROTA K., YAMAGUCHI O., J. Mater. Sci., 31 (1996), 4945.
[17] ROSSIGNOL S., MADIER Y., DUPREZ D., Catal. Today, 50 (1999), 261.
[18] HIRANO M., KATO E., J. Am. Ceram. Soc., 104 (1996), 958.
[19] CABANAS A., DARR J.A., LESTER E., POLIAKOFF M., Chem. Comm. (2000), 901.
[20] CABANAS A., DARR J.A., LESTER E., POLIAKOFF M., J. Mater. Chem., 11 (2001), 561.
[21] KAPOOR M.P., RAJ A., MATSUMURA Y., Micropor. Mesopor. Mater., 44–45 (2001), 565.
[22] YOSHIOKA T., DOSAKA K., SATO T., OKUWAKI A., TANNO S., MIURA T., J. Mater. Sci. Lett., 11 (1992), 51.
[23] KAKIHANA M., KATO S., YASHIMA M., YOSHIMURA M., J. Alloys Comp., 280 (1998), 125.
[24] SETTU T., GOBINATHAN R., Bull. Chem. Soc. Jpn., 67 (1994), 1999.
[25] ARUNA S.T., PATIL K.C., Nanostr. Mater., 10 (1998), 955.
[26] PRAKASH A.S., KHADAR A.M.A., PATIL K.C., HEGDE M.S., J. Mater. Synth. Process., 10 (2002), 135.
[27] LUO M.-F., LU G.-L., ZHENG X.-M., J. Mater. Sci. Lett., 17 (1998), 1553.
[28] MASUI T., FUJIWARA K., PENG Y., SAKATA T., MACHIDA K., MORI H., ADACHI G., J. Alloys Comp., 269 (1998), 116.
[29] MARTINEZ-ARIAS A., FERNANDEZ-GARCIA M., BALLESEROS V., SALAMANCA L.N., CONESA J.C., OTERO C., SORIA J., Langmuir, 15 (1999), 4796.

[30] PECHINI M.P., US Pat. 3, 330, 697 (1967).
[31] YASHIMA M., OHTAKE K., KAKIHANA M., YOSHIMURA M., J. Am. Ceram. Soc., 77 (1994), 2773.
[32] QUINELATO A.L., LONGO E., LEITE E.R., VARELA J.A., Appl. Organom. Chem., 13 (1999), 501.
[33] YAMAMOTO S., KAKIHANA M., KATO S., J. Alloys Comp., 297 (2000), 81.
[34] CHEN C.C., NASRALLAH M.M., ANDERSON H.U., J. Electrochem. Soc., 140 (1993), 3555.
[35] CHEN C.C., NASRALLAH M.M., ANDERSON H.U., Solid State Ionics, 70-71 (1994), 101.
[36] YOUNG R.A., SAKTHIVEL A., MOSS T.S., PAIVA-SANTOS C.O., J. Appl. Cryst., 28 (1995), 366.
[37] KRAUS W., NOLZE G., *PowderCell* software, Federal Institute for Materials Research and Testing, 12489 Berlin, Germany.
[38] MIMANI T., PATIL K.C., Mater. Phys. Mech., 4 (2001), 134.
[39] NARENDAR Y., MESSING G.L., Catal. Today, 35 (1997), 247.
[40] DJURADO E., BOUVIER P., LUCAZEAU G., J.Solid State Chem., 149 (2000), 399.
[41] KASPAR J., FORNASIERO P., GRAZIANI M., Catal. Today, 50 (1999), 285.
[42] FORNASIERO P., BALDUCCI G., DI MONTE R., KASPAR J., SERGO V., GUBITOSA G., FERRERO A., GRAZIANI M., J. Catal., 164 (1996), 173.
[43] YASHIMA M., ARASHI H., KAKIHANA M., YOSHIMURA M., J. Am. Ceram. Soc., 77 (1994), 1067.
[44] YASHIMA M., MORIMOTO K., ISHIZAWA N., YOSHIMURA M., J. Am. Ceram. Soc., 76 (1993), 2865.
[45] YASHIMA M., MORIMOTO K., ISHIZAWA N., YOSHIMURA M., J. Am. Ceram. Soc., 76 (1993), 1745.
[46] MERIANI S., SPINOLO G., Powder Diffract., 2 (1987), 255.
[47] KASPAR J., FORNASIERO P., BALDUCCI G., DI MONTE R., HICKEY N., SERGO V., Inorg. Chim. Acta, 349 (2003), 217.
[48] ESCRIBANO V.S., LOPEZ E.F., PANIZZA M., RESINI C., AMORES J.M.G., BUSCA G., Solid State Science, 5 (2003), 1369.
[49] TROVARELLI A., BOARO M., ROCCHINI E., LEITENBURG C., DOLCETTI G., J. Alloys Comp., 323–324 (2001), 584.
[50] YASHIMA M., YOSHIMURA M., Mater. Jpn, 34 (1995), 448.
[51] YASHIMA M., YOSHIMURA M., Jpn. J. Appl. Phys., 31 (1992), L1614.
[52] *Nanomaterials: synthesis, properties and applications*, A.S. Edelstein, R.C. Cammarata (Eds.), Institute of Physics Publishing, Bristol, 1995, p. 201.
[53] COLON G., PIJOLAT M., VALIVIESO F., VIDAL H., KASPAR J., FINOCCHIO E., DATURI M., BINET C., LAVALLEY J.C., BAKER R.T, BERNAL S., J. Chem. Soc. Faraday Trans., 94 (1998), 3717.
[54] DI MONTE R., FORNASIERO P., GRAZIANI M., KASPAR J., J. Alloys Compd., 275–277 (1998), 877.
[55] HIRATA T., ZHU H., FURUBAYASHI T., NAKATANI I., J. Am. Ceram. Soc., 76 (1993), 1361.
[56] HIRATA T., ZHU H., Solid State Commun., 80 (1991), 991.
[57] FORNASIERO P., KASPAR J., SERGO V., GRAZIANI M., J. Catal., 182 (1999), 56.
[58] HIRATA T., ASARI E., KITAJIMA M., J. Solid State Chem., 110 (1994), 201.
[59] YASHIMA M., OHTAKE K., KAKIHANA M., ARASHI H., YOSHIMURA M., J. Phys. Chem. Solids, 57 (1996), 17.
[60] ZHANG F., CHAN S.-W., SPANIER J.E., APAK E., JIN Q., ROBINSON R.D., HERMAN I.P., Appl. Phys. Letters, 80 (2002), 127.
[61] MICHEL D., JORBA M.P.Y, COLLONGUES R., J. Raman Spectr., 5 (1976), 163.
[62] OTSUKA-YAO-MATSUO S., OMATA T., IZU N., KISHIMOTO H., J. Solid State Chem., 138 (1998), 47.
[63] MASUI T., OZAKI T., MACHIDA K., ADACHI G., J. Alloys Comp., 303–304 (2000), 49.
[64] IZU N., OMATA T., OTSUKA-YAO- S., J. Alloys Comp., 270 (1998), 107.
[65] OTSUKA-YAO-MATSUO S., MORIKAWA H., IZU N., OKUDA K., J. Japan Inst. Metals, 59 (1995), 1237.

Received 16 April 2004
Revised 22 June, 2004